UNIVERSITY
OF TRENTO – Italy

Giovanni Noselli

Structural-model experiments revealing bifurcation, instability and localization

March, 2011

University of Trento
University of Brescia
University of Padova
University of Trieste
University of Udine
University IUAV of Venezia

Giovanni Noselli

STRUCTURAL-MODEL EXPERIMENTS REVEALING BIFURCATION, INSTABILITY AND LOCALIZATION

Advisor: Prof. Davide Bigoni

2011

UNIVERSITY OF TRENTO
Engineering of Civil and Mechanical Structural Systems
XXIII cycle

Ph.D. Program Head: Prof. Davide Bigoni

Final Examination: March 25, 2011

Board of Examiners:
Prof. Antonio DeSimone, SISSA, Trieste
Prof. Ettore Pennestrì, University of Roma Tor Vergata
Prof. Robert M. McMeeking, University of California, Santa Barbara
Prof. Roberto Oboe, University of Padova

A mio padre,
alla mia famiglia,
ai miei buoni amici.

SUMMARY

Small scale experiments are invented to analyze several aspects of instability and bifurcation occurring in structures and within materials.

Photoelasticity is employed to analyze the localization of stress in ordered granular materials and near stiff and thin inclusions embedded in an elastic matrix.

Prototypes have been designed and realized of elastic structures evidencing buckling under tensile dead loading and flutter and divergence instabilities as related to dry friction.

All the experiments have been performed at the Laboratory for Physical Modeling of Structures and Photoelasticity of the Department of Mechanical and Structural Engineering of the University of Trento.

Trento, March 25, 2011

Giovanni Noselli

ACKNOWLEDGEMENTS

The constant supervision and optimism of my advisor, Prof. Davide Bigoni, have been fundamentals during these years. I would like to express my gratitude to him for his remarks, suggestions and encouragements throughout this research work.

I am grateful to all members of the Solid and Structural Mechanics Group of the University of Trento, in particular I am highly thankful to Dr. Francesco Dal Corso and to Mr. Diego Misseroni for their cooperation.

Finally, I am especially grateful to all members of the Mechanical Service of the Faculty of Science, in particular to Mr. Pierino Gennara and Mr. Franco Berti.

PUBLISHED PAPERS

The main results presented in this thesis have been summarized in the following papers:

1. Bigoni, D. and Noselli, G. (2010) Localized stress percolation through dry masonry walls. Part I – Experiments. *European Journal of Mechanics A/Solids*, **29**, 291-298;

2. Bigoni, D. and Noselli, G. (2010) Localized stress percolation through dry masonry walls. Part II – Modelling. *European Journal of Mechanics A/Solids*, **29**, 299-307;

3. Noselli, G., Dal Corso, F. and Bigoni, D. (2010) The stress intensity near a stiffener disclosed by photoelasticity. *International Journal of Fracture*, **166**, 91-103;

4. Zaccaria, D., Bigoni, D., Noselli, G. and Misseroni, D. (2011) Structures buckling under tensile dead load. *Proceedings of the Royal Society A*, *in press*;

5. Bigoni, D. and Noselli, G. (2011) The experimental evidence of flutter and divergence instabilities induced by dry friction. *Submitted*.

CONTENTS

INTRODUCTION

Modern materials and structures are studied to work under extreme conditions, so that the knowledge of bifurcations and instabilities that may occur in a structural component during mechanical loading is the basis of a rational design. In the pursuit of a combined theoretical/experimental approach to mechanics, we address the design and realization of small scale experiments to highlight crucial aspects of instability and to determine special manifestations of this.

We begin analyzing ordered granular materials, in particular dry masonry walls, presenting in Chapter 1 experimental results obtained through transmission photoelasticity on scale models. These experiments disclose a stress distribution complicated by unilateral joints between elements, where 'randomness constrained within a geometrical scheme' of contact points occurs. As a result, a highly localized stress percolation is observed, evidencing 'unloading islands' in a 'stress stream', see Fig. 1.

These findings are theoretically explained in Chapter 2 both proposing a micromechanical model, based on a form of random cascade transmission of forces between bricks, and applying a phenomenological description, based on the extreme orthotropy of the equivalent homogeneous material.

The validity of photoelastic technique to determine highly localized and severe stress fields is confirmed by the results reported in Chapter 3, related to the analysis of the stress field near a thin and stiff linear inclusion, a so-colled 'stiffener', embedded in an elastic matrix. In particular, the linear elastic solution for the stiffener, which involves a square-root singularity, has been experimentally validated, (see for instance the comparison

between the experimental results and the theoretical full-field solution for MODE I loading reported in Fig. 2).

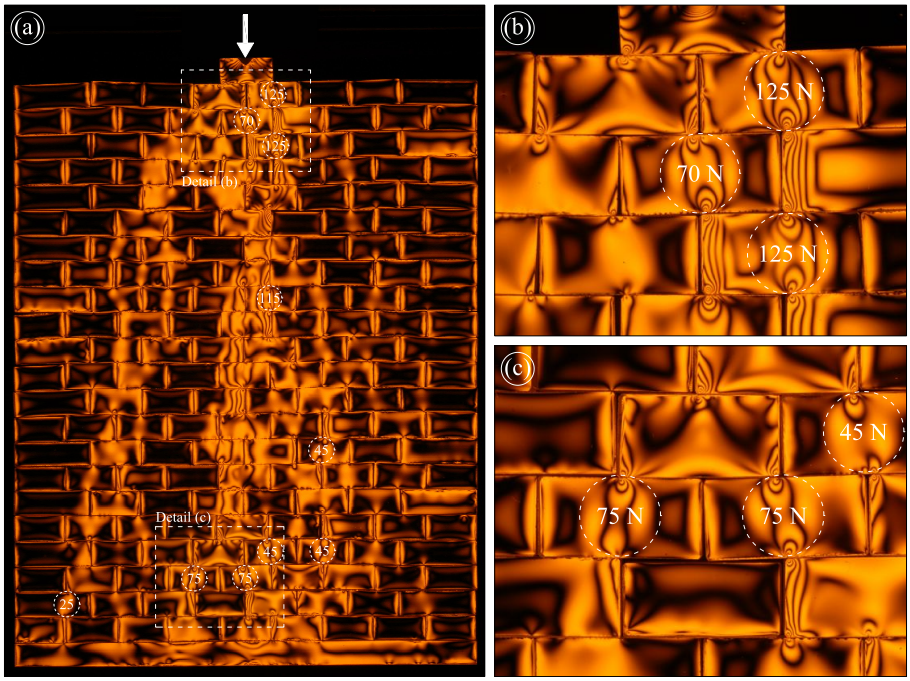

Fig. 1: Photoelastic fringes in a model of dry masonry (see Fig. 2.2 for details) under an applied vertical load, denoted with a white arrow. Note the highly localized, tree-like stress percolation, showing 'unloading islands' separated by 'stress streams'.

A novel and apparently unexpected behaviour is analyzed in Chapter 4, where elastic structures buckling under tensile dead loads are discovered and analyzed in detail, both theoretically and experimentally. In particular, prototypes have been designed and realized of elementary structures with a single degree of freedom and more complex mechanical systems, where buckling in tension is related to the presence of a structural junction, called 'slider', allowing only relative transversal displacement between the connected elements.

In systems composed by two elastic rods connected through a slider bifurcations occur both in tension and compression and are governed by

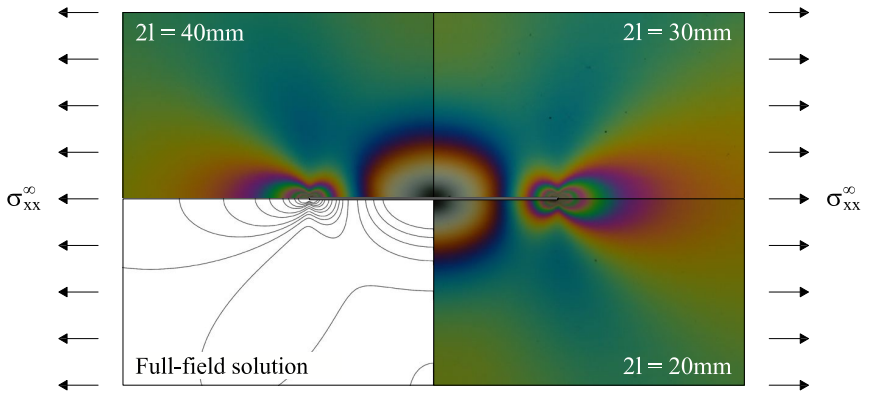

Fig. 2: Photoelastic fringes revealing the stress field near a thin line inclusion embedded in an elastic matrix loaded at remote horizontal tensile stress, compared to the linear elastic plane strain solution. The image is the composition of three experimental results, obtained for different stiffener lengths, see Fig. 3.1 for details.

the equation of the elastica, employed here for tensile loading, so that the buckled rods take the form of the capillary curve in a liquid, which is in fact governed by the equation of the elastica under tension, see Fig. 3.

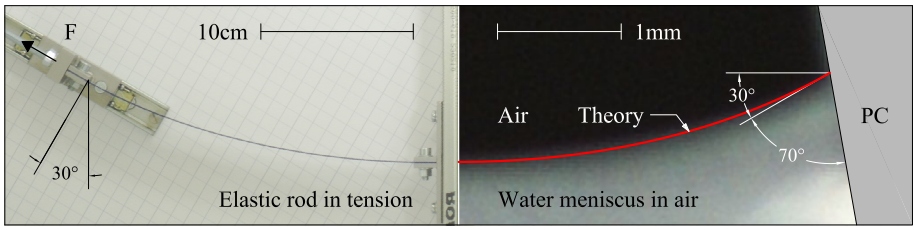

Fig. 3: Analogy between an elastic rod buckled under tensile force and a water meniscus in a capillary channel (superimposed to the solution of the elastica, marked in red); the deflection of the rod and the surface of the liquid have the same shape, see Section 4.4.

Chapter 5 is devoted to the experimental analysis of flutter and divergence instabilities in a structure as connected to the presence of dry friction, inducing a follower force, which was previously thought to be of extremely difficult practical realization, but is now obtained in a quite

simple way.

The presented results provide the first indisputable evidence that flutter and divergence instabilities can be induced by Coulomb friction. Two

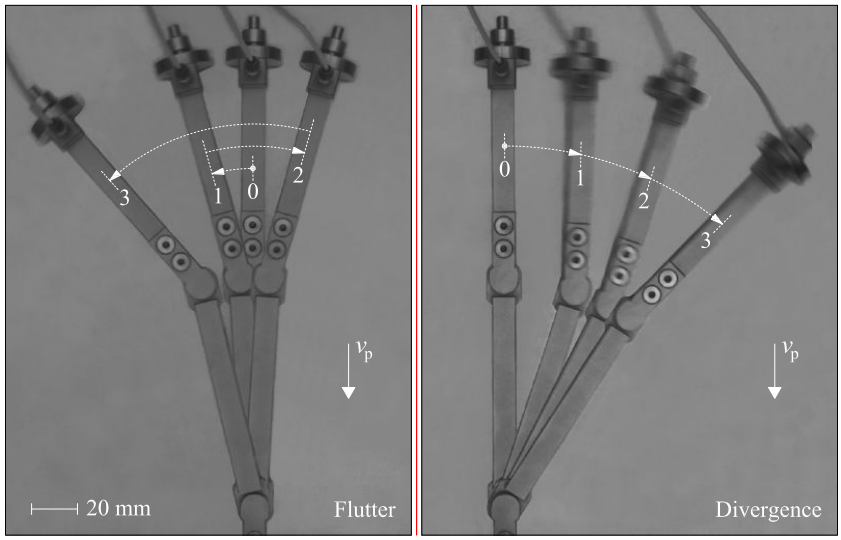

Fig. 4: A superposition of photos taken at different instants of time of a two-degree-of-freedom structure (Ziegler's column) exhibiting flutter (left) and divergence (right) instability. The whole movement took 1.08 s (0.36 s) for flutter (for divergence). Note the oscillatory nature of the flutter instability (left), in contrast to the growing motion typical of divergence (right).

experiments evidencing flutter and divergence instability are shown in Fig. 4.

All the experiments have been performed at the Laboratory for Physical Modeling of Structures and Photoelasticity of the Department of Mechanical and Structural Engineering of the University of Trento.

CHAPTER

ONE

LOCALIZED STRESS PERCOLATION THROUGH DRY MASONRY WALLS - EXPERIMENTS

Transmission photoelasticity on scale models is shown to disclose the stress distribution within dry masonry walls. This distribution is found to be complicated by unilateral joints between elements, where 'randomness constrained within a geometrical scheme' of contact points occurs, so that stress percolation results highly localized, evidencing 'unloading islands' in a 'stress stream'. These findings are theoretically explained in Chapter 2 of this thesis from both micromechanical and continuous modelling perspectives.

1.1 Introduction

How does the stress flow round a rose window in a masonry façade of a church? How does the stress rearrange when a new hole is punched in a masonry? What is the complexity of a stress state in the vicinity of a relieving arch of several voussoirs embedded in a masonry? Although masonry is an ancient and extremely successful[1] composite material, these questions still remain for many aspects open. This is due to the fact that, even for simple geometries and far from failure loadings, masonry structures exhibit a mechanical response affected by extreme stiffness contrast between constituents, randomness of contact points between bricks where

[1]Nacre, mother-of-pearl, is a natural material with unchallenged mechanical properties (Gao *et al.*, 2003) and very similar to masonry (Bertoldi *et al.*, 2008).

unilaterality and Coulomb friction dominate. These effects are known to be important in granular materials, which represent typical disordered media. In contrast, masonry is a regular distribution of elements possessing uniform geometry[2], so that the contact point distribution is 'orderly random', in the sense that it is randomly distributed within a constraining regular scheme.

The interplay between extreme stiffness contrast and randomness on the one hand and regularity of the fabric on the other, yields stress distributions within masonry walls that may present localized stress paths, evidencing stress concentrations and stress relieves (for instance, the so-called 'arching effect'). Surprisingly, transmission photoelasticity - successfully employed for granular materials[3] - has never been applied to the analysis of the stress state in a masonry wall, so that the only experimental setting resembling a stone block construction (rather than a granular assemblage or a masonry) has been investigated by Da Silva and Rajchenbach (2000).

We consider for the first time in the present work the so-called 'stretcher bond fabric' (in the masonry nomenclature), reproduced without mortar[4] and with different spacing between the vertical joints, where transmission of a vertical compressive force (applied on a small area) is analyzed. Results reveal that the contact points are practically always located at the brick corners, but with a random distribution so that a highly localized, tree-like stress percolation results, showing 'unloading islands' separated by 'stress streams'. The 'streams' are shown to broaden when load is increased, as a result of the fact that contact 'points' between bricks evolve into contact 'areas'[5]. Moreover, different stress percolations occur in 'nom-

[2]The texture is fundamental to determine the 'global' mechanical behaviour of a masonry structure. To highlight this concept with a simple example, we remark that the construction without centering of the Brunelleschi's dome in the Florence Cathedral and the achievement of a minimal safety factor against collapse in this structure would have both been simply impossible without the recourse to a highly sophisticated -and effective- brick disposition (Mainstone, 1970).

[3]The idea of employing photoelasticity to investigate the stress distribution within granular materials goes back to Drescher and de Josseiling de Jong (1972). A reference interesting to our purposes is Zhu *et al.* (1996), where results are referred to elliptical particles, which are more similar to a brick masonry than the circular or pentagonal disks used for instance by Geng *et al.* (2001, 2003).

[4]An attempt to simulate mortar is presented in Appendix A

[5]The fact that the contact between bricks is localized at random points is perfectly

inally identical' masonries, due to the different contact distributions.

Two alternatives are proposed in Chapter 2 of this thesis to fully explain experiments, namely: (i.) the micromechanical model, where the masonry is treated as an elastic structure with unilateral 'orderly random' contacts to generate a form of random cascade of vertical forces, where 'random coalescence' may occur in addition to the usual rule of random branching; (ii.) the continuum model, where the masonry behaves as a strongly orthotropic material close to the elliptic border and reveals stress localization following concepts proposed by Bigoni and Capuani (2002, 2005).

Although simple structural models are addressed in this article, the proposed experimental technique and mechanical constitutive description can be applied to brick or stone masonry, as well as to megalithic constructions, and easily extended to analyze: (i.) different homogeneous or composite masonry textures[6]; (ii.) structural masonry elements (for instance, an arch opening in a masonry); (iii.) effectiveness of restoration design (for instance, a structural rehabilitation through reinforcement with FRP).

1.2 Experimental

Three different photoelastic materials produced in sheets have been employed, namely, an extruded PC (Lexan®), a PSM–9 (purchased from Vishay®), and a PMMA (Plexiglas®) to manufacture 187 miniaturized $20\,\text{mm} \times 10\,\text{mm} \times 6\,\text{mm}$ bricks (some of these have different dimensions, namely $30\,\text{mm} \times 10\,\text{mm} \times 6\,\text{mm}$, to complete the rectangular geometry employed in the experiments). The miniaturized bricks have been ordered

known in the building practice, where mortar is introduced with the main purpose of distributing loading. Although less evident, this function of mortar is important also for megalithic block constructions, where mortar facilitates masonry setting, but also prevents cracking of stone blocks (see the example reported by Clarke and Engelbach (1930) referred to the casing-blocks of the Great Pyramid at Giza). We have tried to simulate mortar layers in our experiments by adding 0.5 mm thick paper slices between bricks. The resulting stress percolation patterns still remain highly localized (see Appendix A).

[6]With reference to the ancient Roman architecture, examples of homogeneous textures, different from those analyzed in the present article, are the so-called 'opus reticulatum', or 'opus spicatum', while 'opus mixtum' denotes an example of composite texture.

into two types of stretcher–bond fabric masonries, one with nominally null and another with thick (8 mm) vertical joints.

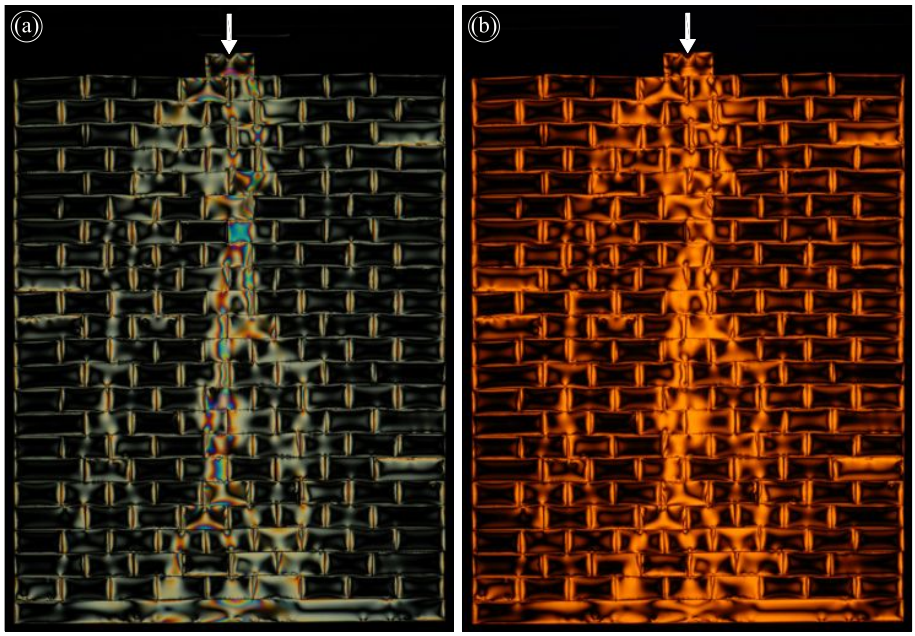

Fig. 1.1: Photoelastic fringes of a model of dry masonry with thin vertical joints detected with a linear transmission polariscope (axes at 45° with respect to the vertical) at (a) white light and (b) sodium vapor lamp ($\lambda = 589.3\,\mathrm{nm}$); low vertical applied load (125 N), denoted with a white arrow.

The PMMA and PC bricks have been cut with a AKE Cutting & Better® circular saw blade HM-KS $200 \times 2.2 \times 30$ Z80, while the PSM-9 with a Dremel® moto-scroller saw blade 16440. To enhance optical properties, all bricks have been hand polished employing sand-paper P120.

The masonries have been positioned between two glasses to prevent possible out-of-plane displacements, but a 1 mm gap has been left between the model and the glasses, to avoid diffused contact (in fact the masonry samples have in some cases 'touched' the glasses at a few points only, so that masonry/glass friction has not been involved).

Temperature near the samples, monitored with a thermocouple connected to a Xplorer GLX Pasco®, has been found to lie around 22°C,

without sensible oscillations during experiments. Loading has been prescribed by providing a vertical fixed 2 mm/min velocity of displacement (corresponding to a 'global' conventional 1% per minute velocity of deformation) to a steel tool similar to the edge of a screwdriver.

The vertical displacement has been imposed using a ELE Tritest 50 machine (ELE International Ltd) on which a linear and a circular (with quarterwave retarders for 560 nm) polariscope (equipped with a white and Sodium vapor lightbox purchased from Tiedemann & Betz) has been installed, which has been designed by us and manufactured at the University of Trento[7].

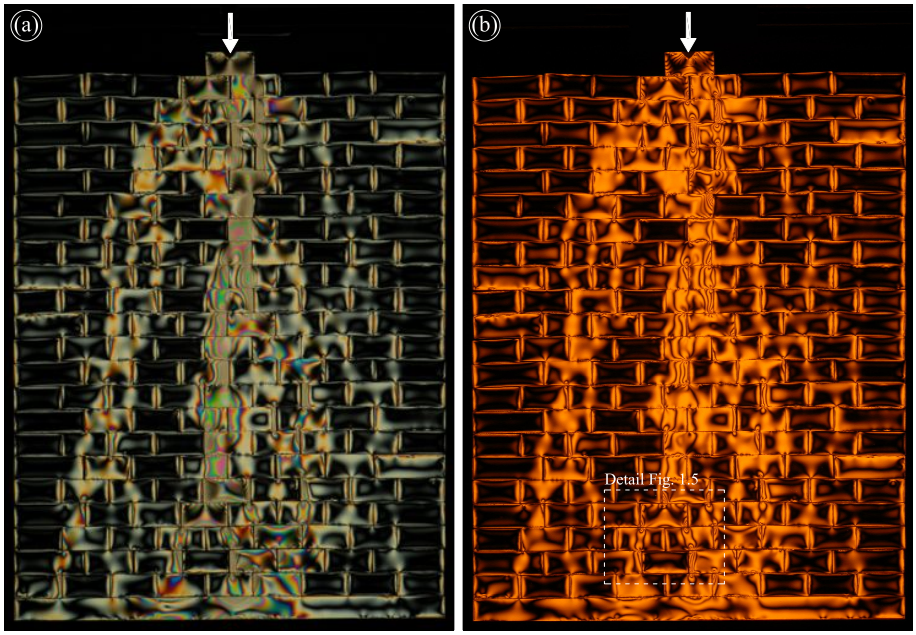

Fig. 1.2: Photoelastic fringes of a model of dry masonry with thin vertical joints detected with a linear transmission polariscope (axes at 45° with respect to the vertical) at (a) white light and (b) sodium vapor lamp ($\lambda = 589.3$ nm); high vertical applied load (250 N), denoted with a white arrow.

[7] A description of photoelasticty and related experimental techniques can be found for example in Coker and Filon (1957) and Frocht (1965).

Photos have been taken with a Nikon® D200 digital camera, equipped with a AF-S micro Nikkor (105 mm 1:2.8G ED) lens and with a AF-S micro Nikkor (70-180 mm 1:4.5-5.6 D) lens for details.

Vertical displacements and vertical forces have been recorded during all tests employing a PY2-F-25 vertical displacement transducer (purchased from Gefran SpA), a TH-KN1D loading cell (also purchased from Gefran SpA), and a Datascan 7320 data acquisition system (Measurement System Ltd).

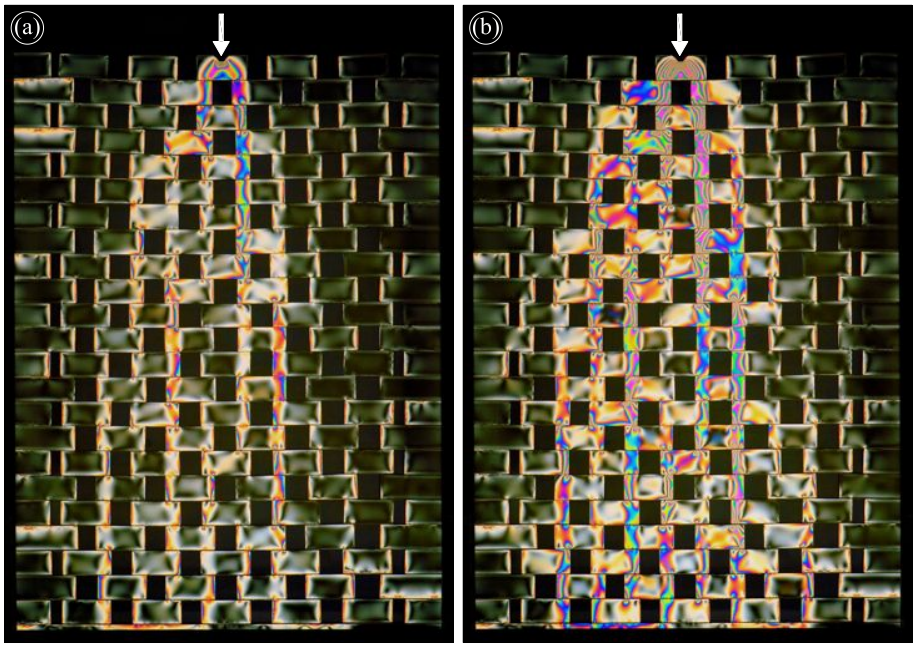

Fig. 1.3: Photoelastic fringes of a model of dry masonry with thick vertical joints detected with a circular transmission polariscope at white light (the white arrow denotes the applied load). (a) low vertical load (200 N) and (b) high vertical load (400 N).

Typical results obtained with a linear transmission polariscope on PSM-9 material are shown in Figs. 1.1 and 1.2, obtained with polarizer axes inclined at 45° with respect to the vertical, using white and Sodium vapor lamps. The figures refer to low (125 N for Fig. 1.1) and high (250 N for Fig. 1.2) loading.

Figs. 1.1 and 1.2 pertain to a masonry with null space forming the vertical joints (see Appendix A for further experimental results[8]).

Thick joints are investigated in Fig. 1.3 obtained with a circular polariscope at low (200 N for Fig. 1.3a) and high (400 N for Fig. 1.3b) load, employing white light. The joints are 8 mm thick.

Details (referred to a masonry different from those reported in Figs. 1.1 and 1.2) are reported in Fig. 1.4, together with the load displacement curve recorded at the top of the sample. These have been taken at red monochromatic light, employing the linear polariscope with a monochromator filter (wavelength 680 nm) and the analyzer inclined at 45°. The details reported in Fig. 1.4 allow investigation of contact areas and forces.

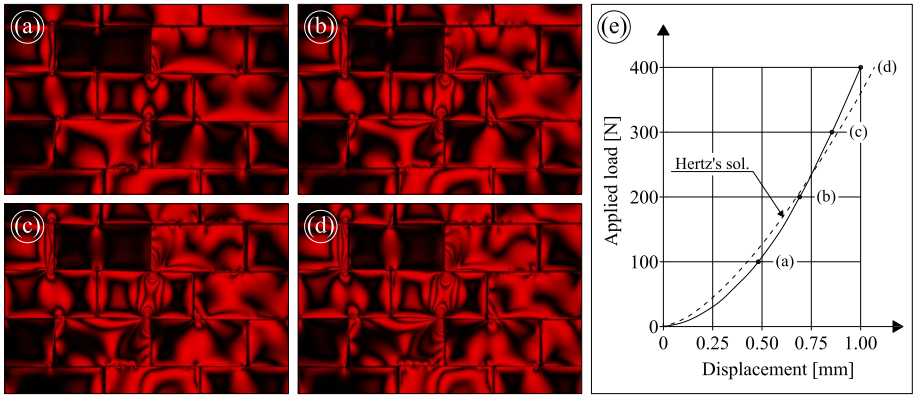

Fig. 1.4: Photoelastic fringes of a model of dry masonry detected with a linear transmission polariscope at red light. (a) photo taken at 100 N of vertical load; (b) photo taken at 200 N of vertical load; (c) photo taken at 300 N of vertical load; (d) photo taken at 400 N of vertical load. Note the typical Hertzian contact fringes in the brick roughly at the centre of the photos. (e) load displacement curve, resulting nonlinear due to the broadening of contact areas between bricks, in full agreement with results referred to contact mechanics.

Note that the nonlinearity of the load displacement curve agrees with the fact that contact areas increase during loading, consistently with results from contact mechanics (Johnson, 1985). In particular, Hertz's the-

[8] A movie of an experiment and other information can be downloaded from: http://ssmg.ing.unitn.it.

ory prescribes that the total load compressing two elastic spheres is proportional to the mutual approach of the centres elevated to the power 3/2, the law which has been plotted in Fig. 1.4e with a proportionality coefficient taken to fit our data.

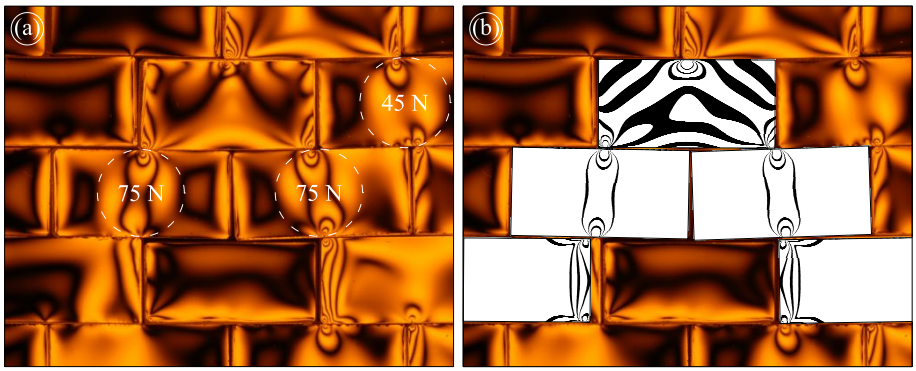

Fig. 1.5: Detail (a) of Fig. 1.2b compared to (b) a linear elastic f.e. simulation of isochromatics (black contours within white bricks denote calculated in-plane principal stress difference).

An analysis of contacts between bricks with a quantification of the load transmitted between them is provided Chapter 2 (see Fig. 2.2).

A detailed investigation of a particular of Fig. 1.2b is reported in Fig. 1.5a, contrasted with a linear elastic finite element simulation of isochromatics under the plane stress assumption (reported in Fig. 1.5b and obtained using ABAQUS Standard, Ver. 6.7-1, Hibbitt, Karlsson & Sorensen Inc., employing 4-nodes bilinear elements CPS4).

The simulation (black contours reported on 'white' bricks) provides the difference between in-plane principal stresses, corresponding to the isochromatics. In the simulation, bricks have been separately analyzed, subjected to reciprocal contact forces taken in a way that equilibrium is satisfied. It can be noted that the experiment is nicely reproduced, so that the conclusion that the stress transmission within a masonry is dominated by contact between bricks remains fully confirmed. Note also that when the force is applied at the middle of the brick the stress state is very similar to that obtained from the elastic solution of a circular disk loaded by two

opposite forces, a consideration that will be used to quantify the force percolation in the masonry (see Fig. 2.2).

The analysis of the photos reported in Figs. 1.1-1.4 and the simulation reported in Fig. 1.5 reveals the following features:

i.) localized contacts at random positions (but constrained to lie near the vertices, therefore within the 'rigid' masonry geometry) between bricks;

ii.) existence of low friction at these contacts;

iii.) the stress distribution:

  a.) is localized and elongated in the vertical direction;

  b.) is organized as in a percolation tree;

  c.) evidences unloading zones;

iv.) due to the fact that randomness is constrained, the stress percolations do not qualitatively differ much from each other. However, our results demonstrate that 'nominally identical' masonry structures can be subjected to different stress states under the same loads.[9]

The fact that the stress percolation is highly localized explains the known difficulty in detecting the stress state of masonry structures using the so-called 'flat-jack' test.

Our results indicate that a sort of 'indeterminacy principle' could affect this test, since -first- the location of the stress 'streams' is not known and -second- the cut in the masonry (which is preliminary required to the introduction of the flat-jack) alters the contact points and therefore the stress distribution.[10]

1.3 Interpretation of experimental results

There are two ways to successfully explain the obtained experimental results: one is the micromechanical approach, in which the masonry is

[9]Different stress percolation patterns are recorded in the same masonry, when the brick distribution is changed, see Appendix A.

[10]For a definition of the flat-jack test, see ASTM Standard: 'In-situ compressive stress within solid unit masonry estimated using flat-jack measurements' C 1196-91, 1991.

modelled as a discrete structure, where bricks are randomly in contact at their vertices; another is the continuum mechanics approach, in which the material is modelled as a continuous homogeneous material, characterized by an extreme orthotropy, so that the material response is close to an instability threshold. Both approaches are deferred to Chapter 2.

1.4 Conclusions

Scale models represent a new tool for investigating the localized and non-unique internal stress distribution induced by external loads within a dry masonry, allowing the reproduction of the exact texture of a masonry, crucial in the understanding of the global structural behaviour.

The experimental technique evidences the behaviour of a material on the verge of material instability, where the perturbative approach proposed by Bigoni and Capuani (2002, 2005) reveals its effectiveness, as it is shown in Chapter 2 of this thesis.

A Additional experimental results

A.1 Dry masonry models

Experimental results, additional to those presented in Figs. 1.1-1.4, are shown in Figs. 1.6-1.9, referred to the PSM-9 material (Figs. 1.6 and 1.7), to the Lexan material (Fig. 1.8), and to the PMMA material (Fig. 1.9). The photos have been taken with a linear transmission polariscope at

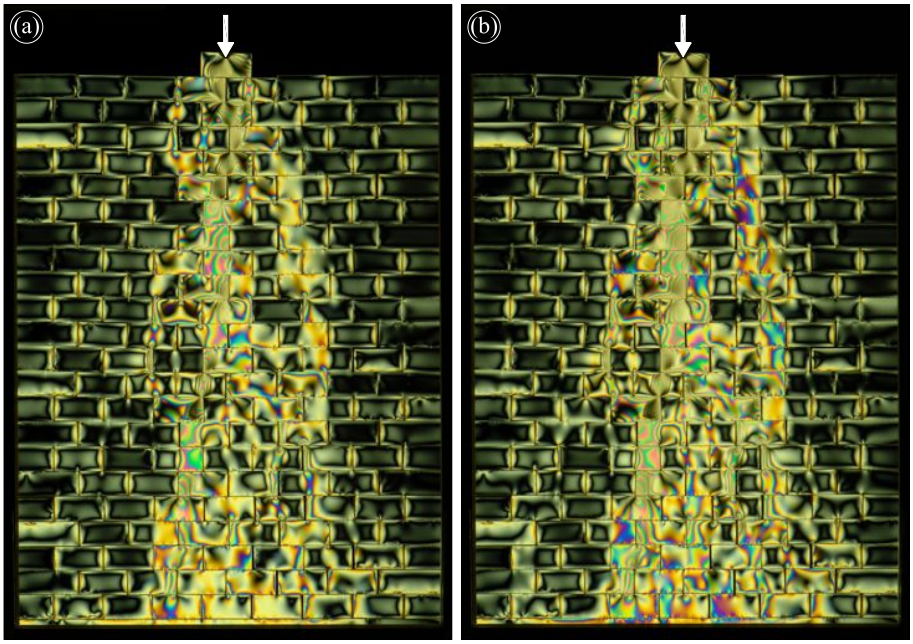

Fig. 1.6: Photoelastic fringes of a model of dry masonry detected with a linear transmission polariscope at white light with analyzer inclined at 45°. Material used is PSM-9 (the white arrow denote the applied vertical load). (a) low vertical load (400 N); (b) high vertical load (800 N).

white light with analyzer inclined at 45°. The vertical loads have been taken equal to 400 N and 800 N for the parts (a) and (b), respectively, of Figs. 1.6 and 1.8, relative to the PSM-9 and the Lexan material. The photos in Fig. 1.9, relative to the PMMA material, have been taken at a vertical load of 1000 N for part (a) and 2500 N for part (b).

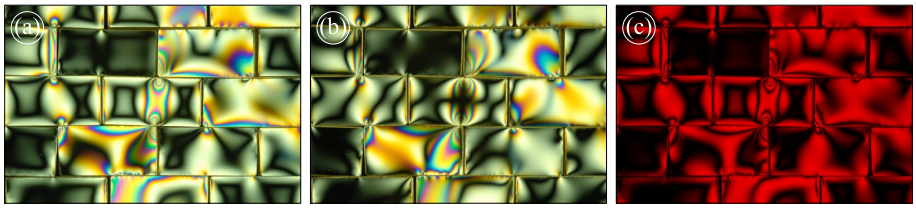

Fig. 1.7: Photoelastic fringes of a model of dry masonry detected with a linear transmission polariscope at 200 N of vertical load. (a) white light with analyzer inclined at 45°; (b) white light with analyzer inclined at 9° with respect to the vertical axis; (c) red light with analyzer inclined at 45°. The isoclines are visible from which low friction and near-vertex contact points can be detected.

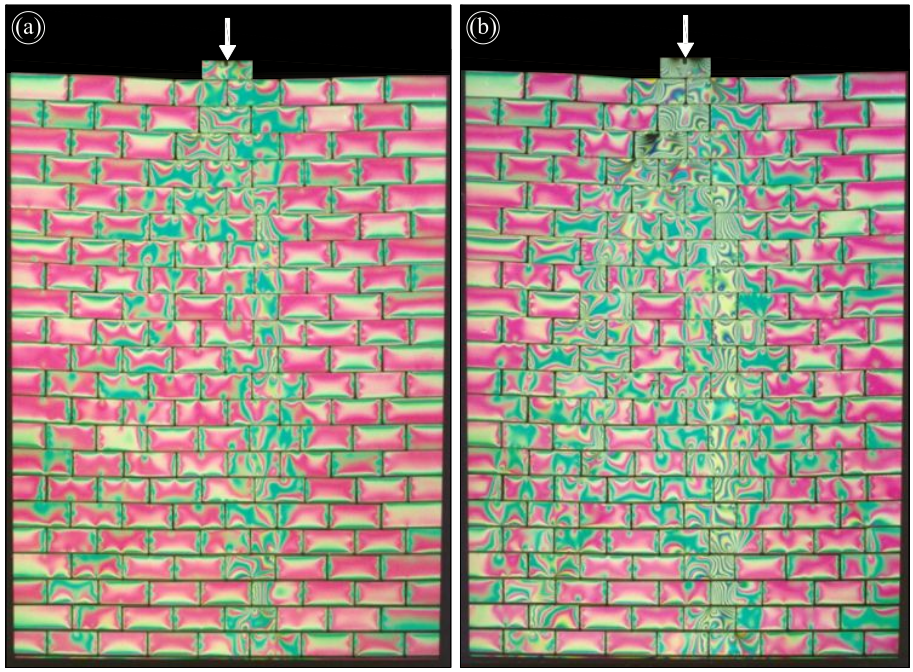

Fig. 1.8: Photoelastic fringes of a model of dry masonry detected with a linear transmission polariscope at white light with analyzer inclined at 45°. Material used is Lexan® (the white arrow denote the applied vertical load). (a) low vertical load (400 N); (b) high vertical load (800 N).

Details of results reported in Fig. 1.6 evidencing near-vertex contact points and low friction and additional to those reported in Fig. 1.3 are reported in Fig. 1.7.

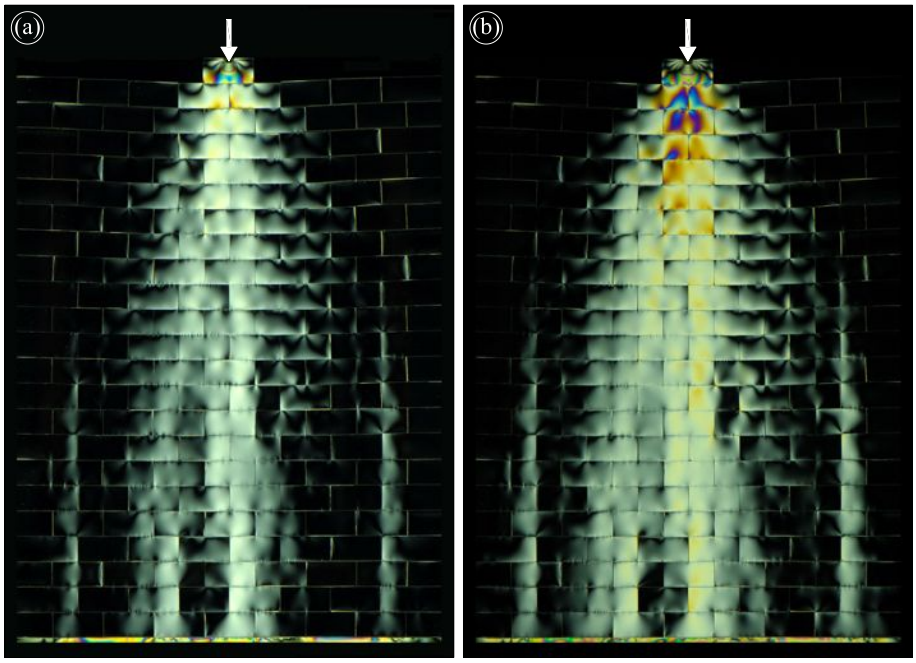

Fig. 1.9: Photoelastic fringes of a model of dry masonry detected with a linear transmission polariscope at white light with analyzer inclined at 45°. Material used is PMMA (the white arrow denote the applied vertical load). (a) low vertical load (1000 N); (b) high vertical load (2500 N).

The details reported in Fig. 1.7 allow investigation of contact areas and forces, see for example the second brick from left in the third course from the top. Here the typical Hertz (see Johnson, 1985) fringe pattern is clearly visible.

A.2 An attempt to simulate the effects of mortar

In an attempt to simulate the effects of mortar, 0.5 mm thick paper layers have been introduced between brick courses, while the vertical joints

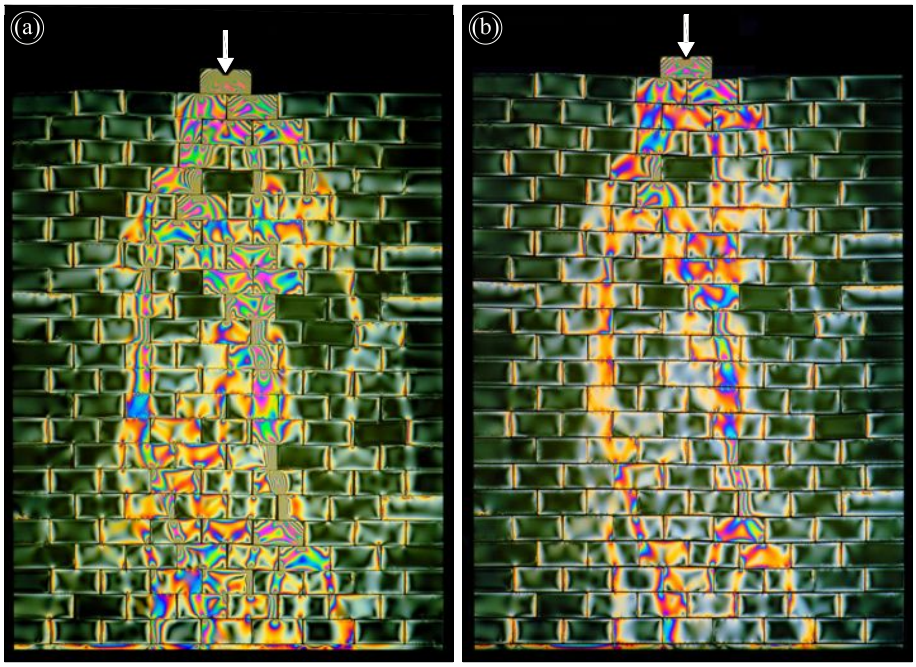

Fig. 1.10: Photoelastic fringes of a model of dry masonry detected with a circular transmission polariscope at white light and at 400 N of vertical load. Material used is PSM-9. (a) dry masonry; (b) mortar courses are simulated with paper layers. Part (b) shows that the intensity of transmitted forces is lower than in part (a), but localization of 'stress streams' appears even greater where mortar is simulated.

between bricks have been kept dry.

Results obtained with a circular polariscope are reported in Fig. 1.10, where a comparison is made with the same masonry (with exactly the same brick distribution) at the same vertical load.

It is clear from Fig. 1.10 that the 'mortar' courses mitigate the stress intensity, but the stress localization results even more pronounced in the case where mortar is simulated using paper layers (Fig. 1.10b), than for dry masonry (Fig. 1.10a).

CHAPTER
TWO

LOCALIZED STRESS PERCOLATION THROUGH DRY MASONRY WALLS - MODELLING

The highly localized stress distribution found within dry masonry walls through transmission photoelasticity in Chapter 1 of this thesis is explained both proposing a micromechanical model (based on a form of random cascade transmission of forces between bricks, which includes random coalescence additionally to random branching) and applying a phenomenological description (based on the extreme orthotropy of the equivalent homogeneous material).

2.1 Introduction

Transmission photoelasticity has been shown in Chapter 1 of this thesis to reveal the highly inhomogeneous stress distribution within dry masonry walls, where 'unloading islands' emerge in a narrow 'stress stream'. The key to the interpretation of these experimental results is randomness (but constrained within the regular scheme imposed by the masonry) of contacts between bricks and 'overall' material orthotropy with high contrast in elastic moduli. Accordingly, two alternatives are proposed to fully explain experiments presented in Chapter 1, namely, (i.) the micromechanical model - where the masonry is treated as an elastic structure with unilateral 'orderly random' contacts, to generate a form of random cascade of vertical forces, where 'random coalescence' may occur in addition to the usual rule of random branching - and (ii.) the continuum model -

where the masonry behaves as a strongly orthotropic material close to the elliptic border and reveals stress localization following concepts proposed by Everstine and Pipkin (1971) and Bigoni and Capuani (2002, 2005).

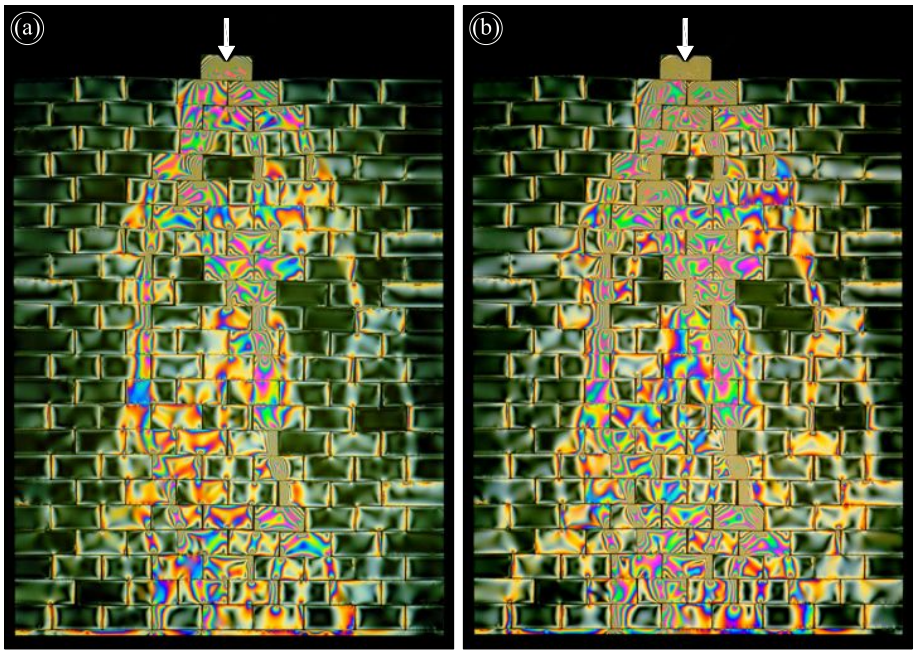

Fig. 2.1: Photoelastic fringes of a model of dry masonry with thin vertical joints detected with a circular transmission polariscope at white light. (a) Low vertical load (400 N); (b) high vertical load (800 N). Note the unloaded brick three courses below the applied vertical load (denoted with a white arrow).

Although they both successfully explain our experimental results, the micromechanical approach and the continuum model have limitations, in the sense that the former is a simple approach tailored on our experimental setting (so that it cannot be immediately generalized to cover complex stress situations), while the latter approach is general, though does not reproduce the diversity of the stress states within masonries (the two approaches could be combined, but this falls beyond the scope of this thesis).

2.2 A résumé of experimental results

We refer to the experiments reported in Figs. 2.1 and 2.2, together with those reported in Chapter 1 of this thesis to highlight: (i.) the highly localized nature of (almost vertical) stress percolation within the masonry and (ii.) the fact that forces are almost vertically transmitted at random contacts between bricks.

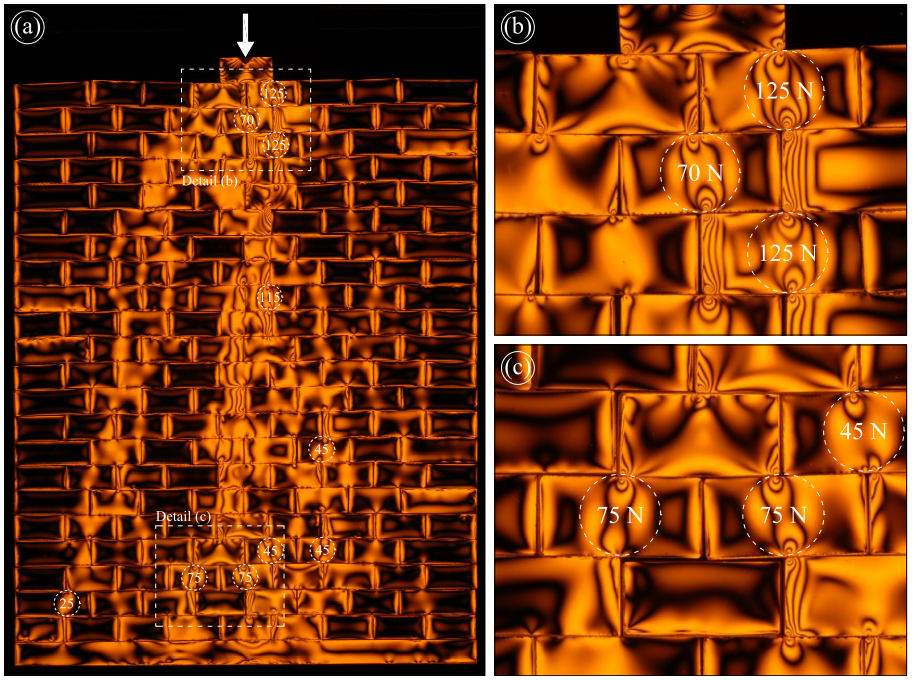

Fig. 2.2: Photoelastic fringes of a model of dry masonry with thin vertical joints detected with a linear transmission polariscope equipped with sodium vapor lamp (axes at 45° with respect to the vertical) at an applied load of 250 N, denoted with a white arrow. Forces have been quantified through comparison with the solution of an elastic disk subject to two opposite forces. (a) 1.2b of Chapter 1 of this thesis. Details are reported in parts (b) and (c).

A quantification of these forces has been proposed in Fig. 2.2 (which is the same photo reported in Fig. 1.2b of Chapter 1 of this thesis), through comparison with the elastic solution of a disk subject to two equal and

opposite forces (the material used is PSM-9, for which the fringe constant is known to be 10.5 kPa/fringe/m). The stress state in the disk is very similar to that obtained with f.e. simulations when the force is applied at the center of the brick, so that the use of the analytical solution for the disk permits a fast and enough accurate treatment of the images.

The quantification of force percolation shown in Fig. 2.2 reveals that there is little diffusion of the load through the masonry, so that the 125 N plus 70 N force near the load application becomes 75 N plus 75 N plus 45 N in the three neighbor bricks near the bottom of the sample.

To fully appreciate the strong, qualitative difference between results reported in Figs. 2.1 and 2.2 and those pertaining to a model of identical dimension, but homogeneous, we report in Fig. 2.3 results pertaining a 72 mm × 88 mm × 6 mm rectangular plate of PSM-9 material, loaded in the same way as for the masonry models, namely, with a vertical force applied on a 8 mm × 4 mm × 6 mm punch (also made of PSM-9).

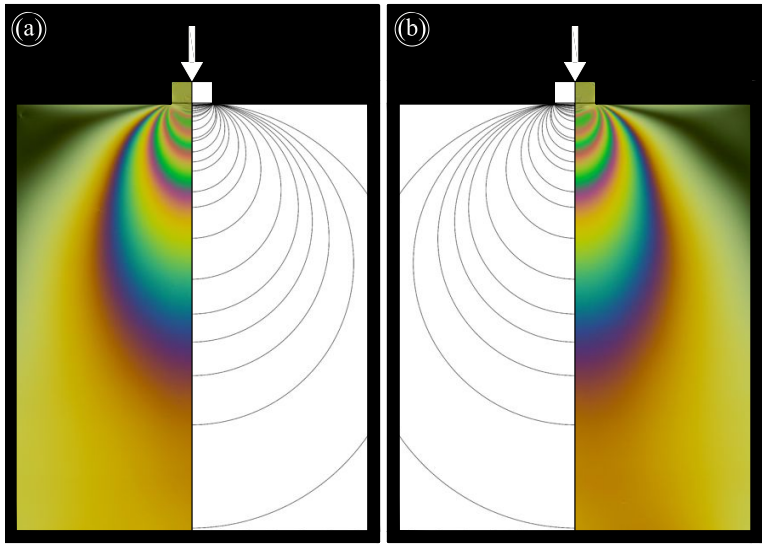

Fig. 2.3: A uniform rectangular plate loaded on a small portion of its edge through a 500 N vertical force. Isochromatic fringes detected with a circular transmission polariscope at white light and compared to the analytical solution for an elastic homogeneous isotropic half space, loaded on a portion of its boundary, Eq. (2.2).

The photo reported in Fig. 2.3, taken with the circular polariscope at 500 N vertical load, has been split into two parts and interpolated with the analytical solution for a uniform loading on a finite area of a semi-infinite elastic plate (which is derived below, Eq. (2.2), see also Johnson, 1985). This solution can be derived from the problem of a concentrated force F orthogonal to the otherwise free surface of an elastic half space, the so-called 'Flamant solution', where only the radial stress is different from zero and is given by

$$\sigma_r(r,\theta) = -\frac{2F}{\pi} \cdot \frac{\cos\theta}{r}, \tag{2.1}$$

where r is the radial distance between the vertical force and the point under consideration in the elastic half space, singled out by the angular coordinate θ, taken null when the point lies on the vertical line of the loading force. The stress state induced in the half space when a uniform load p is applied on a segment of length $2b$ is obtained in Cartesian coordinates through integration of Eq. (2.1) as

$$\begin{aligned}
\sigma_{11}(x_1,x_2) &= -\frac{2p}{\pi}\int_{-b}^{b} \frac{(x_1-\xi)^2 x_2}{[(x_1-\xi)^2+x_2^2]^2}\,d\xi,\\
\sigma_{22}(x_1,x_2) &= -\frac{2p}{\pi}\int_{-b}^{b} \frac{x_2^3}{[(x_1-\xi)^2+x_2^2]^2}\,d\xi,\\
\sigma_{12}(x_1,x_2) &= -\frac{2p}{\pi}\int_{-b}^{b} \frac{(x_1-\xi)x_2^2}{[(x_1-\xi)^2+x_2^2]^2}\,d\xi,
\end{aligned} \tag{2.2}$$

where x_1 and x_2 are respectively the horizontal and the vertical axes of a coordinate system centered at the middle of the uniformly loaded segment $[-b,\ b]$. Note that, although the stress field (2.2) is referred to a semi-infinite elastic medium, the comparison with the experiment reported in Fig. 2.3 and referred to a finite rectangular plate is very satisfactory. This is related to the fact that the loading punch is small when compared to the dimensions of the plate.

A comparison between Fig. 2.3 and the figures pertaining to the masonry models (Figs. 2.1 and 2.2) reveals that the stress state within the masonry models deeply differs from the elastic, isotropic and homogeneous solution. This situation has been noted in somewhat similar experiments

by Da Silva and Rajchenbach (2000). Their conclusion is that the experiments do not fit both elasticity and plasticity models, rather, they show diffusive patterns. Although we do not disprove their conclusions (rather we agree on several points), we suggest here an interpretation not involving any diffusion. In particular, we point out that experimental results on masonry models can be successfully interpreted in two alternative ways, namely, *either as the response of a highly inhomogeneous material composed by a regular - though discontinuous - structure, or as the response of a homogeneous elastic, but strongly orthotropic, material*. The former approach is based on micromechanical considerations, while a macroscopic modelling in terms of an equivalent homogeneous material is pursued following the latter approach. We explain both approaches below.

2.3 Interpretation of experimental results

There are two ways to explain the obtained experimental results: one is the micromechanical approach, in which the masonry is modelled as a discrete structure, where bricks are randomly in contact at their vertices; another is the continuum mechanics approach, in which the material is modelled as a continuous homogeneous material, characterized by an extreme orthotropy. Both approaches can be successfully developed as follows.

2.3.1 Micromechanics: masonry as a discrete structure with random contacts between bricks

The bricks have been found to be randomly in contact at their vertices, so that a simple micromechanical model of our masonries can be obtained as follows (explained with reference to the case of null vertical joints, while thick vertical joints are treated in Appendix A):

i.) our physical models are loaded vertically and experiments show that friction does not play an important role. Friction is therefore neglected in the mathematical model, so that it is assumed that forces percolate only vertically through the masonry;

ii.) since experiments show that forces are localized near the brick vertices, we assume that every brick is loaded at its upper edge by three

compressive vertical forces, applied at the centre and at the vertices of the edge (F_1, F_2 and F_3 in Fig. 2.4b). Moreover, the contact points at the lower edge of a brick are always two, to be randomly chosen between three possibilities (labeled 1, 2 and 3 in Fig. 2.4b);

iii.) equilibrium of the brick and unilaterality of the contacts at the lower edge of it determine the vertical reaction forces (R_1, R_2 and R_3 in Fig. 2.4b), which become the vertical forces for the upper edges of the bricks at the lower course.

More in detail, the load transmission mechanism 1 involves two reaction forces applied at the lower corners of the brick, determined as

$$\begin{aligned} R_1 &= F_1 + \frac{F_2}{2}, \\ R_2 &= 0, \\ R_3 &= F_3 + \frac{F_2}{2}. \end{aligned} \tag{2.3}$$

The load transmission mechanism 2 (3) involves a reaction force applied at the central point of the lower edge of the brick, plus a reaction force applied at the left (right) corner or a reaction force applied at the right (left) corner, depending on the satisfaction of the unilateral constraint that no tensile forces are transmitted throughout the masonry. The reaction forces are thus determined as

$$\begin{aligned} R_1 &= \langle F_1 - F_3 \rangle, \\ R_2 &= F_1 + F_2 + F_3 - \langle F_1 - F_3 \rangle - \langle F_3 - F_1 \rangle, \\ R_3 &= \langle F_3 - F_1 \rangle, \end{aligned} \tag{2.4}$$

where $\langle\rangle$ denotes the Macaulay brackets defined for all real α as $\langle \alpha \rangle = (|\alpha| + \alpha)/2$.

The algorithm to determine a force percolation within a masonry works as follows. For a given masonry geometry, first, the load mechanisms between the bricks are randomly generated (employing a discrete probability density function) selecting between the three possibilities listed in Fig. 2.4b and, second, the forces and the contact points are obtained by employing Eqs. (2.3) or (2.4). The proposed algorithm works in such a way that

all equilibrium conditions (including rotational equilibrium) and unilateral constraints are automatically satisfied. It is clear that *the structure*

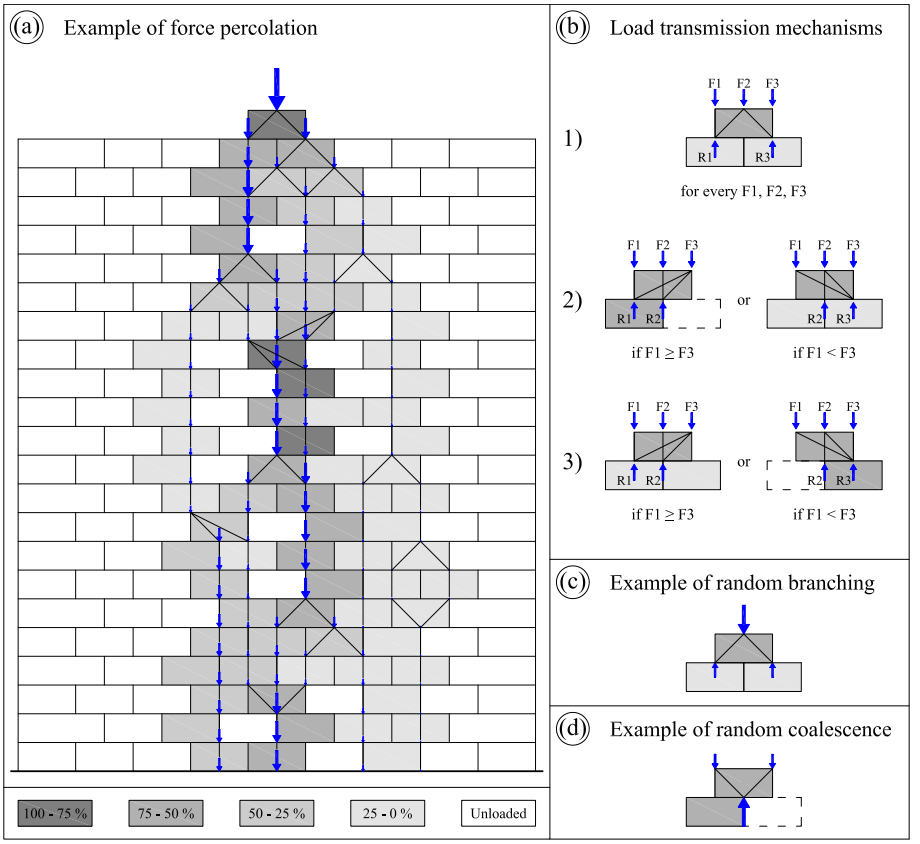

Fig. 2.4: Model of a masonry as a discrete system with a form of random cascade vertical force transmission, where 'random coalescence' is possible, in addition to random branching. An example of force diffusion tree similar to results reported in Fig. 2.1 is given in (a), where the darker is the color, the higher is the force transmitted (white bricks are unloaded, see the scale reported in the lower part of the figure, where the transmitted percent of vertical load has been reported). Force transmission mechanisms are given respectively in part (b), while examples of random force branching and coalescence are presented in parts (c) and (d), respectively.

is statically determinate and there is a great (although finite) number of

force distributions (but all constrained to lie within a certain 'limit' geometry and to possess a certain 'regularity') to equilibrate a given vertical load.[1]

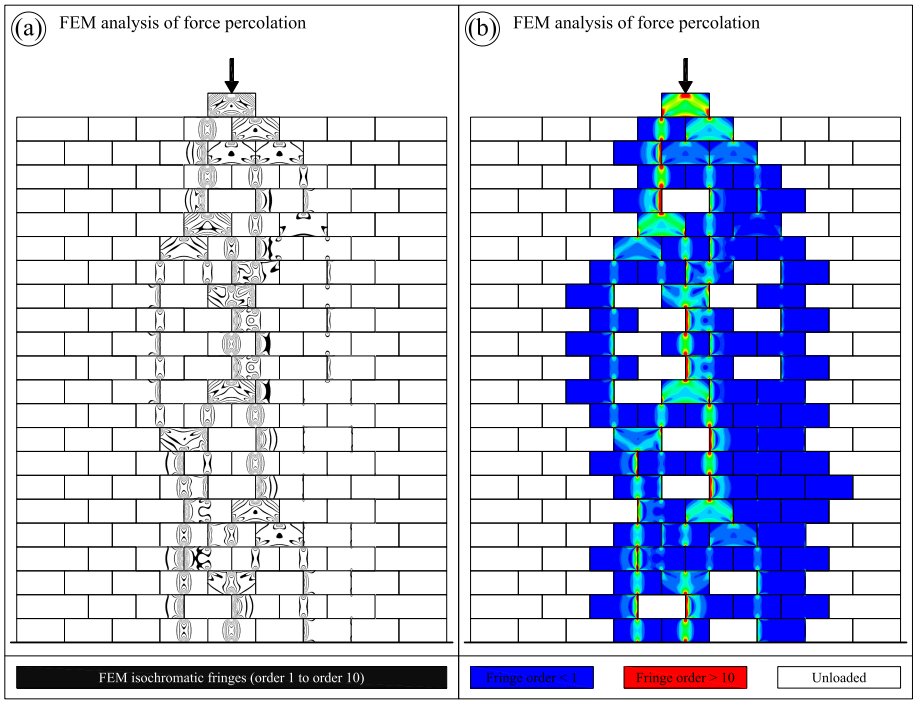

Fig. 2.5: Isochromatics for the masonry loaded through the force percolation tree reported in Fig. 2.4a is analyzed with linear elastic f.e. Monochromatic, part (a), and colored, part (b), contours denote calculated in-plane principal stress difference, corresponding to the photoelastic fringes.

Moreover, the obtained force distribution is a type of *random cascade*, in which some additional rules have to be enforced, so that *random branching* (Fig. 2.4c) is also accompanied by *random coalescence*, occurring when

[1]Since force distributions are always possible and these will ensure equilibrium for applied vertical load distribution of arbitrary intensity, a collapse load will not be predicted for applied vertical loads, a conclusion consistent with limit analysis, where compressive strength is usually taken to be infinite (Heyman, 1966).

two or three vertical forces applied at the upper edge of a brick coalesce into one or two (Fig. 2.4d).

An example of the above procedure for determining a force distribution in a masonry is shown in Fig. 2.4a, where darker bricks are loaded more than lighter. This stress distribution has been generated to mimic the experiment shown in Fig. 2.1. After the load percolation through the masonry has been generated with the above-explained algorithm, the stress state within the bricks and the relative simulation of photoelastic fringe patterns (corresponding to in-plane principal stress contours) has been evaluated as in Fig. 1.5 of Chapter 1 (with ABAQUS-Standard, Ver. 6.7-1, Hibbitt, Karlsson & Sorensen Inc., employing 4-nodes bilinear elements CPS4) and reported in Fig. 2.5.

Due to the assumed randomness of the contacts, from a practical point of view only 'some' of the possible stress distributions can be investigated with the proposed model; however, the obtained diversity of the possible stress distributions reproduces our experimental results.

The proposed model shares some similarity with the so-called 'q–model' proposed by Liu *et al.* (1995) (see also Coppersmith *et al.*, 1996), in which the percolation of vertical forces through a granular system is analyzed assuming that the vertical forces are randomly distributed at n contact points, so that for $n = 2$, a unit force is split into a force q and another force $1 - q$. Although rotational equilibrium is violated and horizontal forces are neglected (Socolar, 1998), the q–method allows successful predictions of so–called 'force chains' in random distributions of photoelastic disks. However, the q–model does not provide information on the stress distribution within the elements, while our method, in which both equilibrium and unilaterality of contact are preserved, allows determination of stresses even inside the bricks.

2.3.2 Masonry as a continuous material with extreme orthotropy

In a macroscopic modelling, the highly inhomogeneous structure of the masonry models is 'viewed at a distance' from which inhomogeneity can be disregarded, so that the response of a uniform equivalent continuum is considered. In these conditions, the diversity of the possible stress percolations in nominally identical structures is necessarily lost, since these become in a sense identical when 'viewed at a sufficient distance' and they

appear as manifestations of the same localized stress distribution.

Since prior to vertical loading bricks are set in contact only under the (evidently small) effect of gravity, the vertical joints are unable to sustain any (normal or shearing) traction, while the horizontal joints cannot support shearing stress, but they can carry orthogonal compressive forces. In these conditions and due to the specific geometry of the masonry, the material becomes equivalent to an orthotropic homogeneous material, with a high contrast between stiffness moduli.[2]

The solution for a concentrated force F orthogonal to the otherwise free surface of an elastic orthotropic half space (with orthotropy x_1–x_2 axes aligned parallel and orthogonal to the free surface) has been found by Lekhnitskii (1981). With reference to an elastic material loaded in plane stress (as is the case of our masonry models), the constitutive equations can be written in inverse

$$\begin{aligned} \varepsilon_{11} &= \frac{1}{E_1}(\sigma_{11} - \nu_{12}\sigma_{22}), \\ \varepsilon_{22} &= \frac{1}{E_2}(\sigma_{22} - \nu_{21}\sigma_{11}), \\ \varepsilon_{12} &= \frac{1}{2\mu_{12}}\sigma_{12}, \end{aligned} \tag{2.5}$$

and direct form

$$\begin{aligned} \sigma_{11} &= \frac{E_1}{1-\nu_{12}\nu_{21}}(\varepsilon_{11} + \nu_{21}\varepsilon_{22}), \\ \sigma_{11} &= \frac{E_2}{1-\nu_{12}\nu_{21}}(\varepsilon_{22} + \nu_{12}\varepsilon_{11}), \\ \sigma_{12} &= 2\mu_{12}\varepsilon_{12}, \end{aligned} \tag{2.6}$$

where E_1 and E_2 are the two Young moduli in the directions 1 and 2 respectively, μ_{12} is the shear modulus, while ν_{12} and ν_{21} play a role similar to the Poisson coefficient of isotropic elasticity.

[2]More precisely, this material should be considered elastoplastic, rather than elastic, in conditions where both an elastic or an elastoplastic strain increment may occur. However, the plastic branch of such an elastoplastic material can be analyzed employing an 'elastic comparison material', following concepts introduced by Bigoni and Capuani (2002, 2005). Therefore, the analysis is reduced again to the analysis of the behaviour of an elastic orthotropic material.

The solution for the concentrated force, where only the radial stress is different from zero and defining θ as the angle taken from the vertical line of the load F, is expressed by

$$\sigma_r(r,\theta) = -\frac{F}{\pi}\cdot\frac{\cos\theta}{r}\cdot\sqrt{\frac{E_2}{E_1}}\frac{u_1+u_2}{\Lambda(\theta)}, \tag{2.7}$$

which generalizes the Flamant solution, Eq. (2.1). Here u_1 and u_2 are two roots (to be chosen with the rule that the resultant of σ_r over a semi circle has to be F) of the equation

$$\frac{E_2}{E_1}u^4 + \left(2\nu_{12}\frac{E_2}{E_1} - \frac{E_2}{\mu_{12}}\right)u^2 + 1 = 0, \tag{2.8}$$

and

$$\begin{aligned}\Lambda(\theta) &= \frac{E_2}{E_1}\sin^4\theta - \left(2\nu_{12}\frac{E_2}{E_1} - \frac{E_2}{\mu_{12}}\right)\sin^2\theta\cos^2\theta + \cos^4\theta \\ &= \det[\mathbf{A}(\theta)]\frac{1-\nu_{12}\nu_{21}}{\mu_{12}E_1},\end{aligned} \tag{2.9}$$

is a quantity proportional to the determinant of the so-called 'acoustic tensor' $\mathbf{A}(\theta)$ (Rice, 1977). Therefore, the differential equations governing equilibrium remain (strongly) elliptic until this determinant is strictly greater than zero. Our masonry structure is characterized by a low value of shear modulus μ_{12} and of elastic modulus E_1, the latter particularly in the case of thick joints between bricks. Moreover, the two Poisson's ratios are certainly small and, as a first approximation, they can be taken to be zero, $\nu_{12} = \nu_{21} = 0$, so that the function (2.9) becomes:

$$\Lambda(\theta) = \frac{1}{\mu_{12}E_1}\left(\mu_{12}E_2\sin^4\theta + E_1E_2\sin^2\theta\cos^2\theta + \mu_{12}E_1\cos^4\theta\right). \tag{2.10}$$

The analysis of the singularity of the acoustic tensor when an elastic modulus tends to zero provides the key to the understanding of localization of deformation (Rice, 1977). The following two cases are of interest to describe our experimental results.

i.) Coefficient μ_{12} tends to zero, while E_1 remains finite. Two shear bands form: one vertical and one horizontal, corresponding to a band normal inclined at $\theta = 0$ and $\theta = \pi/2$ in Eq. (2.10) and a shear deformation mode within the band;

ii.) both E_1 and μ_{12} tend to zero. One vertical compaction/separation band becomes possible, corresponding to a band normal inclined at $\theta = 0$ in Eq. (2.10) and a uniaxial strain deformation mode within the band.

Since in both of the above cases one vertical shear band is always possible, the application of a vertical load will result in a stress map elongated and focussed in the vertical direction. This becomes evident from the analysis reported below.

Solution (2.7) depends on two independent elastic constants only and, when a uniform load p is applied on a segment of length $2b$, its integration provides a generalization of solution (2.2) in the form

$$\begin{aligned}
\sigma_{11}(x_1,x_2) &= -\frac{p}{\pi}\sqrt{\frac{E_2}{E_1}}\int_{-b}^{b}\frac{(x_1-\xi)^2 x_2}{\Lambda(x_1,x_2,\xi)[(x_1-\xi)^2+x_2^2]^2}\,d\xi,\\
\sigma_{11}(x_1,x_2) &= -\frac{p}{\pi}\sqrt{\frac{E_2}{E_1}}\int_{-b}^{b}\frac{x_2^3}{\Lambda(x_1,x_2,\xi)[(x_1-\xi)^2+x_2^2]^2}\,d\xi,\\
\sigma_{11}(x_1,x_2) &= -\frac{p}{\pi}\sqrt{\frac{E_2}{E_1}}\int_{-b}^{b}\frac{(x_1-\xi)x_2^2}{\Lambda(x_1,x_2,\xi)[(x_1-\xi)^2+x_2^2]^2}\,d\xi,
\end{aligned} \tag{2.11}$$

where

$$\begin{aligned}
\Lambda(x_1,x_2,\xi) = \frac{1}{[(x_1-\xi)^2+x_2^2]^2}\Bigg[&\frac{E_2}{E_1}(x_1-\xi)^4+\\
&-\left(2\nu_{12}\frac{E_2}{E_1}-\frac{E_2}{\mu_{12}}\right)(x_1-\xi)^2x_2^2+x_2^4\Bigg].
\end{aligned} \tag{2.12}$$

Equations (2.1) and (2.7) are exact. However, in the case (i) of extreme contrast in orthotropy, there is an asymptotic solution available, which approximates Eq. (2.7). This has been found by Everstine and Pipkin (1971)[3] (see also Christensen, 1979) and is expressed by

$$\sigma_{11}(x_1,x_2)=0,\quad \sigma_{2i}(x_1,x_2)=\frac{F}{\epsilon\pi}\frac{x_i}{\left(\frac{x_1}{\epsilon}\right)^2+x_2^2}, \tag{2.13}$$

[3]Everstine and Pipkin (1971) also noticed a 'stress channeling effect' for fiber reinforced materials, essentially similar to the stress percolation found in our models.

where $i \in [1, 2]$ and ϵ^2 is in our case (in which $\nu_{12} = \nu_{21} = 0$) the ratio between the shear modulus μ_{12} and the vertical elastic modulus E_2. When

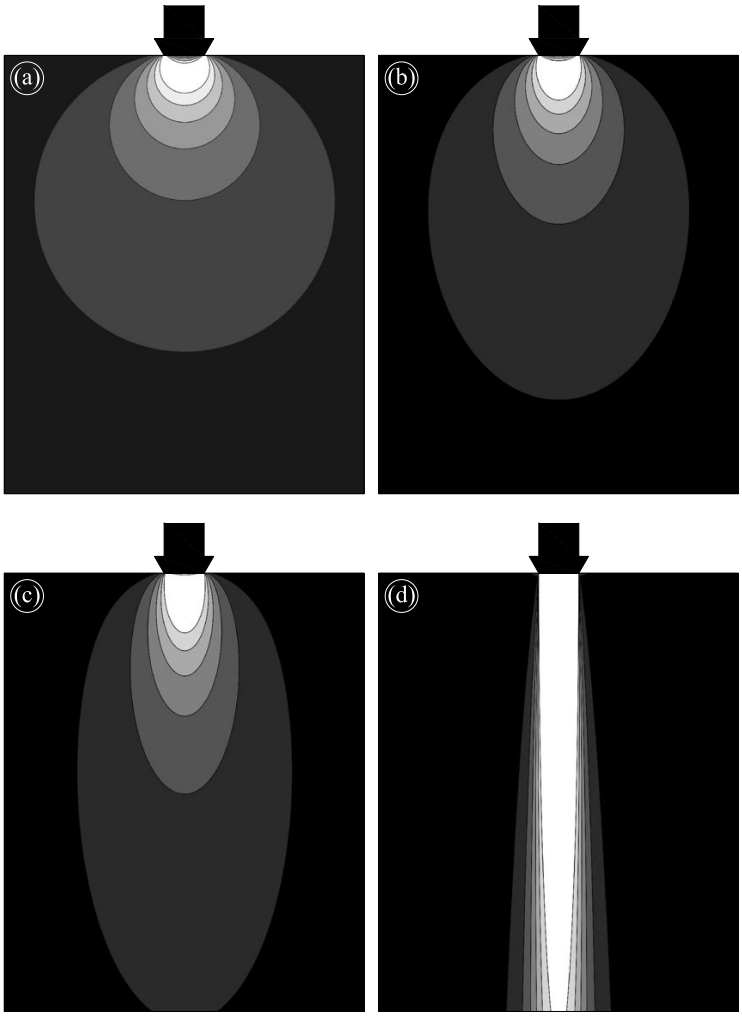

Fig. 2.6: Level sets of in-plane principal stress difference for a vertical uniform force distribution (denoted with a thick black arrow) on an area of finite length on an elastic half space, Eqs. (2.11). (a) The isotropic solution; (b) and (c) 'intermediate' values of orthotropy; (d) the highly orthotropic solution, obtained with both E_1 and m_{12} tending to zero (while $E_1/\mu_{12} = 2$) evidencing nearly vertical stress percolation.

a uniformly distributed load p acts on a half space, Eq. (2.13) can be integrated to obtain the following approximation to Eq. (2.11)

$$\sigma_{11}(x_1, x_2) = 0, \quad \sigma_{2i}(x_1, x_2) = -\frac{p}{\epsilon\pi} \int_{-b}^{b} \frac{x_i - \xi\delta_{1i}}{x_2^2 + \left(\frac{x_1 - \xi}{\epsilon}\right)^2} \, d\xi, \qquad (2.14)$$

where $i \in [1, 2]$ and δ_{1i} is the Kronecker delta.

The use of Eq. (2.11) or (2.14) is equivalent to our purposes, since results are qualitatively identical in both the limit cases (i) and (ii) of extreme orthotropy. Hence, maps of in-plane principal stress difference have been plotted in Fig. 2.6, obtained with Eq. (2.11) and elastic constants ranging from the isotropic case (Fig. 2.6a) to the extreme orthotropy where both E_1 and μ_{12} tend to zero (Fig. 2.6d), keeping $E_1/\mu_{12} = 2$. In particular, Fig. 2.6b-d correspond to E_1/E_2 taken equal to 2/3, 1/3, and 1/300, respectively.

An inspection of Fig. 2.6 clearly reveals that the stress distribution strongly localizes and focusses parallel to the direction of the load when the orthotropy becomes high, which explains the nearly vertical stress percolation in the masonry models. This finding is in complete agreement with results obtained in elastic solids prestressed near the elliptic boundary by Bigoni and Capuani (2002, 2005); Bigoni and Dal Corso (2008); Bigoni *et al.* (2008); Dal Corso *et al.* (2008); Piccolroaz *et al.* (2006). Therefore, our physical models provide examples of a material characterized by constitutive equations with an extreme orthotropy and therefore near the elliptic boundary, or - in other words - near material instability. Perturbed with concentrated forces, the response of such a material can be interpreted within the theory proposed by Bigoni and Capuani (2002, 2005).[4] Accordingly, the mechanical response is highly localized, so that the stress percolates in a 'narrow channel' almost coaxial with the concentrated force.

Note that Fig. 2.6d closely resembles the wave-like stress diffusion pursued by Goldenberg and Goldhirsh (2005), see also Luding (2005) to explain the behaviour of granular materials.[5] In the case (i) of extreme

[4]The perturbative approach has been recently employed to explain fundamental features of shear band propagation by Bigoni and Dal Corso (2008).

[5]Piccolroaz *et al.* (2006) have pointed out that the perturbative approach by Bigoni

orthotropy, where only μ_{12} tends to zero, Eq. (2.14) yields, for $\epsilon = 1/25$, a plot of the principal in-plane stress difference qualitatively identical to Fig. 2.6d and therefore the experimental results are fully explained in both cases (i) and (ii) of extreme orthotropy.

The solution relative to an extreme orthotropy contrast (Fig. 2.6d) fully explains the near vertical stress percolation found in our experiments. The localized stress distribution obtained for high orthotropy contrast degenerates at the boundary of ellipticity into a set of vertical lines, transmitting the load without diffusion, as pointed out by Di Pasquale (1992), with reference to the so-called 'no-tension material model' introduced by Heyman (1966). It should be noted that, consistently with the continuum mechanics assumption and differently from the micromechanics approach, the diversity of stress states within the same masonry structure cannot be now reproduced, since masonry is interpreted as a homogeneous material, while the different localized stress streams are manifestations of the same localized response, differing only for the presence of structural imperfections. A way for reproducing stress-state diversity within a masonry might be pursued by introducing some form of randomly distributed defects in the continuum material, similarly to the randomly distributed dislocations in the simulations of crystal plasticity (van der Giessen and Needleman, 1995), but this leads us beyond the scope of the present investigation.

2.4 Conclusions

Models of dry masonry walls have been shown to represent: (i.) from micromechanical point of view, an example of a microstructure dominated by random (but constrained within a regular fabric) contacts between bricks; (ii.) from continuum modelling point of view, an example of a material on the verge of an instability. These two points of views have been successfully translated into modelling using micromechanical considerations and the perturbative approach proposed by Bigoni and Capuani (2002, 2005). These models explain experimental results presented in Chapter 1 of the present thesis and open a new perspective in the modelling of masonry structures.

and Capuani (2002, 2005) can be generalized to model the behaviour of granular materials.

A Micromechanical model for thick joints

In a microstructural modelling, we can take into account that the distribution of the contact points between bricks is random, but localized near the edges of the bricks. Roughly speaking, the idea here is to treat

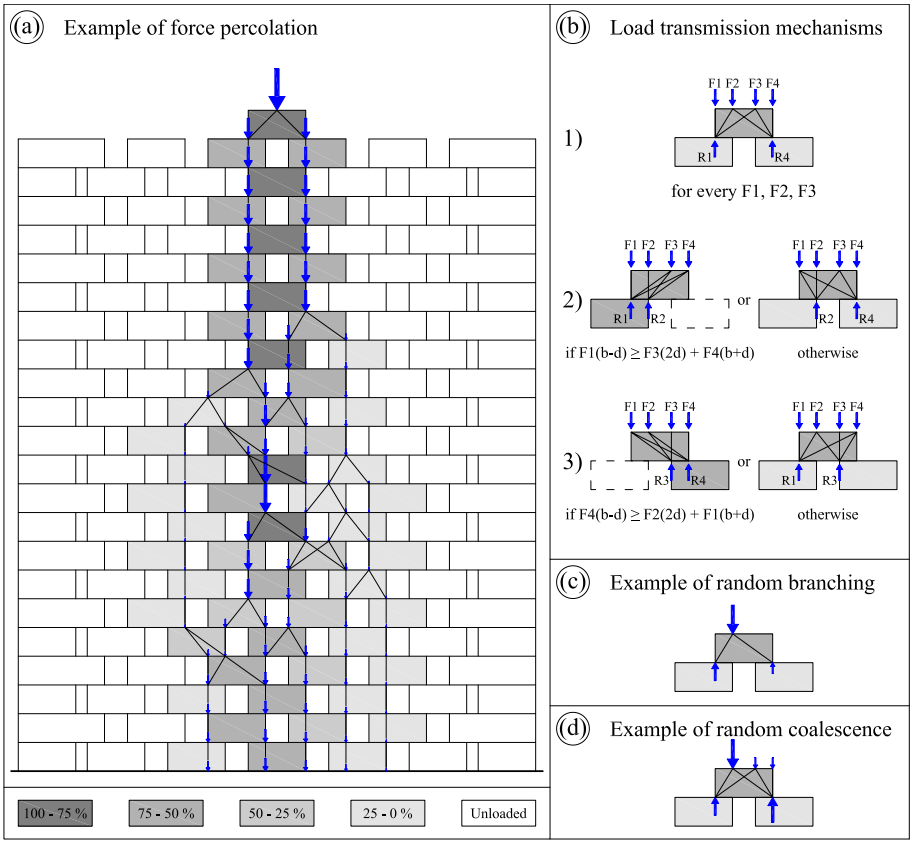

Fig. 2.7: Model of a masonry with thick vertical joints as a discrete system with a form of random cascade vertical force transmission, where 'random coalescence' is possible, in addition to random branching. A dark color denotes a high force transmission, so that white bricks are unloaded (see the scale reported in the lower part of the figure, where the transmitted percent of vertical load is reported). (a) A force percolation tree obtained with the model; (b) force splitting-rules for a masonry with thick joints; (c), (d) examples of random branching and random coalescence.

every brick as a doubly supported beam by randomly distributed reaction forces (R_1–R_4, to be selected between the three possibilities shown in Fig. 2.7b), subject to the vertical loads (F_1–F_4, Fig. 2.7b) transmitted by the two bricks in the upper course.

Note that we have excluded the possibility, never observed in our experiments, that a brick be supported simultaneously at the two corners of the lower bricks. The result of the procedure is a form of random cascade admitting random coalescence, in addition to random branching (Fig. 2.7c–d). Note that the width of the bricks is b and the thickness of the joints is d in Fig. 2.7, so that the reaction forces are determined as

$$\begin{aligned} R_1 &= F_1 + F_2\left(\frac{b+d}{2b}\right) + F_3\left(\frac{b-d}{2b}\right), \\ R_2 &= R_3 = 0, \\ R_4 &= F_4 + F_2\left(\frac{b-d}{2b}\right) + F_3\left(\frac{b+d}{2b}\right), \end{aligned} \tag{2.15}$$

for mechanism 1; as

$$\begin{aligned} R_1 &= \frac{\langle b(F_1 - F_4) - d(F_1 + 2F_3 + F_4)\rangle}{b-d}, \\ R_2 &= F_1 + F_2 + F_3 + F_4 + R_1 - R_4, \quad R_3 = 0 \\ R_4 &= \frac{\langle b(F_4 - F_1) + d(F_1 + 2F_3 + F_4)\rangle}{b+d}, \end{aligned} \tag{2.16}$$

for mechanism 2, and as

$$\begin{aligned} R_1 &= \frac{\langle b(F_1 - F_4) + d(F_1 + 2F_2 + F_4)\rangle}{b+d}, \\ R_2 &= 0, \quad F_1 + F_2 + F_3 + F_4 - R_1 - R_4, \\ R_4 &= \frac{\langle b(F_4 - F_1) - d(F_1 + 2F_3 + F_4)\rangle}{b-d}, \end{aligned} \tag{2.17}$$

for mechanism 3.

We can note from Figs. 2.4 and 2.7 that the proposed micromechanical model correctly reproduces both the tree-like form of the stress percolation and the diversity of 'stress streams' occurring even in nominally identical masonries.

CHAPTER

THREE

THE STRESS INTENSITY NEAR A STIFFENER DISCLOSED BY PHOTOELASTICITY

Can the thickness of a thin inclusion (in a matrix material) be made so small (though retaining sufficient stiffness and matrix adhesion) to generate 'in practice' a stress state in agreement with the analytical (square-root singular) solution for a rigid line inclusion (so-called 'stiffener') embedded in a linear elastic plate? Can this inhomogeneous stress state be generated for tensile loading parallel to the stiffener? We provide a direct and positive answer to these questions, by showing how to produce elastic materials containing thin inclusions and by providing photoelastic investigation of these structures. The experiments fully validate the stress state calculated for an elastic plate containing a rigid (finite-length) line inclusion, until a distance from the inclusion tip on the order of its thickness, corresponding to a stress concentration up to seven.

3.1 Introduction

The experimental stress analysis near a *fracture* in an elastic material is one of the most explored topics in solid mechanics. Without attempting a review, we limit ourself to quote the thorough *photoelastic* investigation of this problem (see the review by Østervig, 1987, the recent applications to dynamics by Lim and Ravi-Chandar, 2007; 2009, and Sammis *et al.*, 2009).

Surprisingly, the experimental investigation of the stress state near a *thin stiff inclusion* in an elastic matrix, akin to the problem of fracture, has received no attention, although the analytical solution is known since fifty years (Muskhelishvili, 1953) and, more importantly, the mechanical behaviour of thin inclusions is fundamental in the design of composite materials. In these materials, the inclusions increase the global stiffness but introduce strong stress concentrators, leading to premature failure (experiments performed in our lab and not reported here show that the presence of a thin inclusion may decrease the failure load of a factor ranging from ten to twenty).[1]

Compared to a crack, the thin rigid inclusion model poses new problems (as first noticed by Dal Corso *et al.*, 2008), so that, while the chief difficulty of experimental fracture mechanics is the realization of a sufficiently sharp crack tip in a sufficiently stiff matrix, a thin inclusion should be realized sufficiently: (i.) thin, (ii.) stiff, (iii.) adherent to the matrix material, in which (iv.) residual stresses should be negligible; moreover, (v.) the presence of the inclusion (rigid when compared to the matrix stiffness) introduces a dependance on the matrix Poisson's ratio, so that plane stress and plane strain correspond to different in-plane stress distributions.[2]

A first, qualitative, approach to the problem has been attempted by Dal Corso *et al.* (2008), so that the purpose of the present paper is: (i.) to describe a technique to obtain photoelastic materials 'sufficiently' free of residual-stress and embedding 'sufficiently' thin, stiff, adherent metallic

[1] Although failure is not addressed in the present article, we have eventually sacrificed all the samples employed for our photoelastic experiments to detect the mean failure stress, to be compared with the failure stress of the material without inclusion. We have found that the ratio between the latter and the former stress fluctuates around ten and may grow to twenty, showing that the thin inclusion is definitely detrimental to strength.

[2] Other problems (not investigated in the present article) raised by the stiffener model are related to the near-reinforcement failure behaviour. One of these (mentioned by Dal Corso *et al.*, 2008) is that the hoop-stress criterion of fracture mechanics does not rule the near-stiffener failure. Another problem is that the criticality of the stress intensity factor cannot directly be related to any energy associated to a 'fracture *advance*', although the stress intensity factor still remains a measure of the severity of the fields and therefore a higher stress intensity factor is related to an earlier near-stiffener fracture *nucleation*. A final problem is related to the fact that a stiffener may *buckle*, when subject to compressive parallel load.

inclusions, (ii.) to present results of photoelastic experiments on this material, (iii.) to provide systematic and quantitative comparison with both asymptotic and full-field elastic solutions.

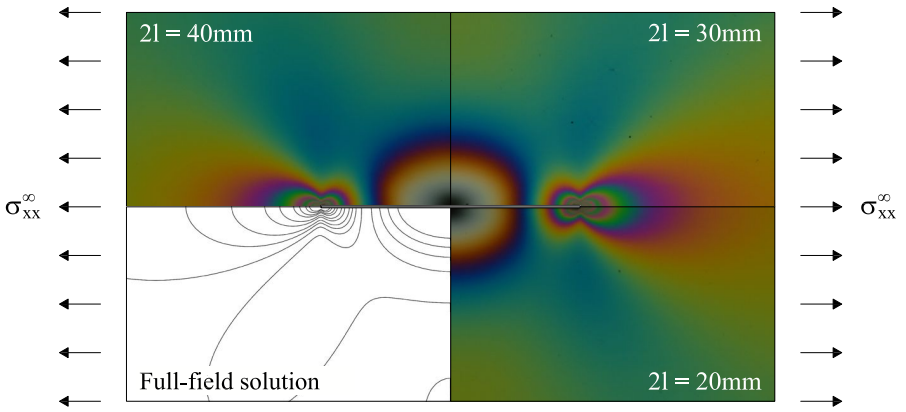

Fig. 3.1: Photoelastic fringes revealing the stress field near a thin line inclusion (0.1 mm thick steel platelet) embedded in an elastic matrix (a two-component 'soft' epoxy resin) loaded at remote stress σ^{∞}_{xx}=0.116 MPa, compared to the elastic solution (in plane strain, with Poisson's ratio equal to 0.45). The image is the composition of three different photos taken for different stiffener lengths ($2l = \{20, 30, 40\}$ mm), scaled down according to self-similarity in order to provide the same stress fields.

The achievement of result (i.) is less trivial than it might appear, since the matrix material should be prepared 'soft enough' to eliminate residual stresses in the vicinity of the rigid inclusion. The fact that the matrix material is soft, implies that a nonlinear dependance of the refraction tensor on the stress state plays a role in interpreting the experiments. Therefore, we have employed a simplified version of a nonlinear theory of photoelasticity in which we have assumed a linear stress/strain response together with a nonlinear dependence of the refraction tensor on the stress, which has been proposed on the basis of our experimental data. As a result, the experiments show an excellent agreement with theoretical prediction, fully substantiating the rigid-line inclusion (so-called 'stiffener') model, Fig. 3.1. Moreover, the stress field in the vicinity of the stiffener tip (Fig. 3.2) is shown to follow with great precision the linear elastic asymptotic solution until a distance comparable with the stiffener thickness (0.1 mm), where

the maximum measured stress concentration (the ratio between stress at a point and the remote applied stress) results to be equal to seven.

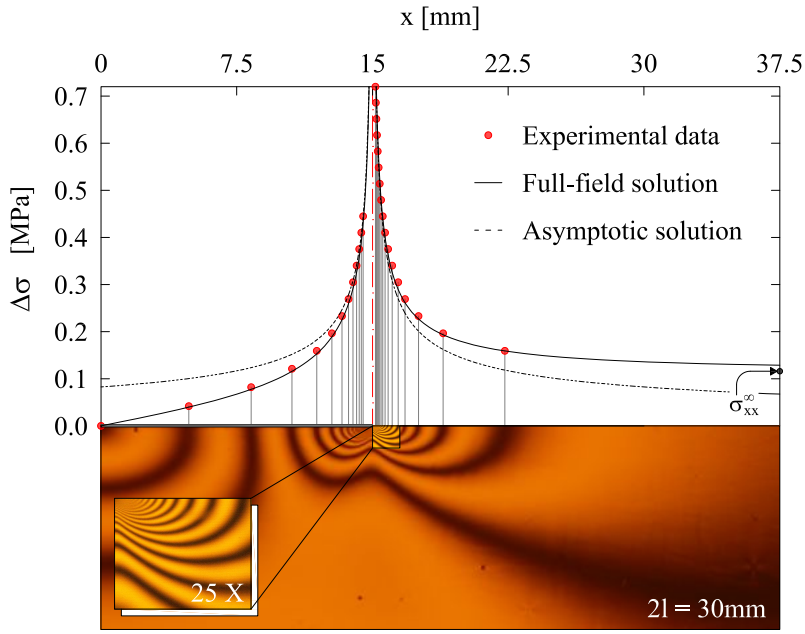

Fig. 3.2: In-plane principal stress difference $\Delta\sigma$ along the stiffener line: comparison between photoelastic experiment with monochromatic light and the full-field and asymptotic elastic solutions, for remote stress σ^{∞}_{xx}=0.116 MPa. A detail of the region near to the (right) stiffener tip has been captured using an optical microscope (photo reported in the inset), so that a great number (twenty) of fringes have been detected, until a distance from the tip of the same order of magnitude of the stiffener thickness (0.1 mm). A stress concentration of seven is visible.

3.2 Non-linear photoelasticity

We begin assuming a nonlinear hyperelastic behaviour, isotropic in the unloaded state, so that the constitutive equation can be written in terms of a strain energy density $W(\varepsilon_1, \varepsilon_2, \varepsilon_3)$, function of the principal logarithmic (or 'true') strains ε_i $(i = 1, 2, 3)$, from which the Kirchhoff stress $\mathbf{K}$, defined in terms of Cauchy stress $\boldsymbol{\sigma}$ and J, determinant of the

deformation gradient $\mathbf{F}$, as

$$\mathbf{K} = J\boldsymbol{\sigma}, \quad J = \exp(\varepsilon_1 + \varepsilon_2 + \varepsilon_3), \tag{3.1}$$

is given by (Ogden, 1984)

$$\mathbf{K} = \frac{\partial W}{\partial \varepsilon_1}\mathbf{v}_1 \otimes \mathbf{v}_1 + \frac{\partial W}{\partial \varepsilon_2}\mathbf{v}_2 \otimes \mathbf{v}_2 + \frac{\partial W}{\partial \varepsilon_3}\mathbf{v}_3 \otimes \mathbf{v}_3, \tag{3.2}$$

where $\mathbf{v}_i$ $(i = 1, 2, 3)$ are the unit vectors defining the principal Eulerian axes. In terms of nominal stress $\boldsymbol{\sigma}^{(n)}$, defined as

$$\boldsymbol{\sigma}^{(n)} = \mathbf{F}^{-1}\mathbf{K}, \tag{3.3}$$

Eq. (3.2) becomes

$$\boldsymbol{\sigma}^{(n)} = \frac{1}{\lambda_1}\frac{\partial W}{\partial \varepsilon_1}\mathbf{u}_1 \otimes \mathbf{v}_1 + \frac{1}{\lambda_2}\frac{\partial W}{\partial \varepsilon_2}\mathbf{u}_2 \otimes \mathbf{v}_2 + \frac{1}{\lambda_3}\frac{\partial W}{\partial \varepsilon_3}\mathbf{u}_3 \otimes \mathbf{v}_3, \tag{3.4}$$

where λ_i $(i = 1, 2, 3)$ are the stretches and $\mathbf{u}_i$ $(i = 1, 2, 3)$ are the unit vectors defining the principal Lagrangean axes. Note that the logarithmic strains and the stretches are related by $\varepsilon_i = \log \lambda_i$ $(i = 1, 2, 3)$.

For an elastic material, isotropic in the unloaded state, the refraction symmetric second-order tensor $\mathbf{n}$ can be expressed as isotropic function of the Cauchy stress $\boldsymbol{\sigma}$,

$$\mathbf{n} = \widehat{\mathbf{n}}(\boldsymbol{\sigma}), \tag{3.5}$$

so that the principle of material frame indifference requires

$$\widehat{\mathbf{n}}(\boldsymbol{\sigma}) = \mathbf{Q}^T\widehat{\mathbf{n}}(\mathbf{Q}\boldsymbol{\sigma}\mathbf{Q}^T)\mathbf{Q}, \tag{3.6}$$

for every rotation tensor $\mathbf{Q}$. As a consequence, the function $\widehat{\mathbf{n}}$ has to be isotropic, so that the representation theorems (Wang, 1970) imply that it can be expressed as

$$\mathbf{n} = \alpha\mathbf{I} + \beta\boldsymbol{\sigma} + \gamma\boldsymbol{\sigma}^2, \tag{3.7}$$

where α, β and γ are arbitrary functions of the invariants of $\boldsymbol{\sigma}$.

Our experiments (detailed later) suggest that the nonlinear law (3.7) can be simplified by assuming $\gamma = 0$. Moreover, it is instrumental (to

immediately recover the nomenclature used in the linear theory) to redefine α and β in the following way

$$\alpha = n_0 + c_2 \mathrm{tr}\boldsymbol{\sigma}, \quad \beta = c_1 - c_2, \tag{3.8}$$

where n_0 is the refraction index for the unstressed material, c_1 and c_2 are constant in the linear theory, but in general arbitrary functions of the invariants of $\boldsymbol{\sigma}$. The refraction tensor (3.7) becomes

$$\mathbf{n} = (n_0 + c_2 \mathrm{tr}\boldsymbol{\sigma})\,\mathbf{I} + (c_1 - c_2)\,\boldsymbol{\sigma}. \tag{3.9}$$

Restricting attention to plane (stress or strain) condition, the angular phase shift Δ between the two refracted components of the incident light (with wavelength λ and orthogonal to the plane defining the plane condition) is given by

$$\Delta = \frac{2\pi\, t}{\lambda}\,(n_I - n_{II})\,, \tag{3.10}$$

where t is the current out-of-plane thickness of the material element under consideration, $(n_I - n_{II})$ is the difference of the in-plane principal components of the refraction tensor, that using Eq. (3.9) becomes

$$n_I - n_{II} = (c_1 - c_2)\,\Delta\sigma, \tag{3.11}$$

where $\Delta\sigma = \sigma_I - \sigma_{II}$ is the in-plane principal stress difference. Therefore, the isochromatic fringe order $N = \Delta/2\pi$ is given by

$$N = \frac{t}{\lambda}\,(c_1 - c_2)\,\Delta\sigma. \tag{3.12}$$

In the linear theory, the material fringe constant f_σ

$$f_\sigma = \frac{\lambda}{c_1 - c_2}, \tag{3.13}$$

is introduced, that in our case becomes a function of the stress invariants, so that the fringe order (3.12) is given by

$$N = \frac{t}{f_\sigma}\Delta\sigma, \tag{3.14}$$

corresponding to the well-known law of linear photoelasticity when f_σ and t are assumed to be constants, but in the nonlinear theory under consideration they are related to the *current* values of t, f_σ and $\Delta\sigma$.

Equation (3.14) can be rewritten in terms of nominal quantities (i.e. referred to the undeformed configuration) as

$$N = \frac{t_0}{f_\sigma^{(n)}} \Delta\sigma^{(n)}, \tag{3.15}$$

where t_0 is the undeformed thickness, $\Delta\sigma^{(n)}$ is the nominal in-plane principal stress difference and $f_\sigma^{(n)}$ is the nominal material fringe parameter. Note that $f_\sigma^{(n)}$ and f_σ are related through the following equation

$$f_\sigma^{(n)} = \frac{\lambda_1 \lambda_2 \Delta\sigma^{(n)}}{\sigma_I^{(n)} \lambda_1 - \sigma_{II}^{(n)} \lambda_2} f_\sigma. \tag{3.16}$$

The parameters $f_\sigma^{(n)}$ and f_σ, functions of the stress, have to be obtained experimentally. To this purpose, we have performed uniaxial stress experiments (in the way described in Section 3.4.2), employing homogeneous dog-bone shaped samples cut from each of the samples prepared with the inclusion (and described in Section 3.4.2).[3]

In a uniaxial stress test, where $\sigma_2 = \sigma_3 = \sigma_2^{(n)} = \sigma_3^{(n)} = 0$ and $\lambda_2 = \lambda_3 = t/t_0$, Eq. (3.16) becomes

$$f_\sigma^{(n)} = \frac{t}{t_0} f_\sigma, \tag{3.17}$$

a simple relation which is of great help in measuring $f_\sigma^{(n)}$ and f_σ as functions only of the applied stress σ_1.

The uniaxial stress experiments have revealed a viscous behaviour of the two-component epoxy resin employed for photoelasticity, so that the experiments have been performed at controlled load applied in discrete steps, with a waiting time of 5 minutes before reading displacements and performing the subsequent loading step. The true and nominal stress

[3]The geometry of dog-bone shaped samples has been taken according to the specific ASTM standards ASTM D 638-98 'Standard Test Method for Tensile Properties of Plastics' (Test specimen TYPE IV).

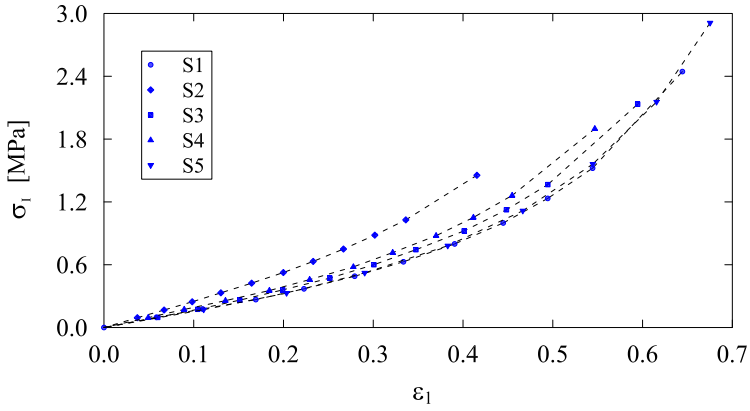

Fig. 3.3: Mechanical properties: applied true (Cauchy) stress σ_I versus true (logarithmic) deformation ε_l. Experimental data obtained with a uniaxial test at controlled load.

behaviours, respectively versus conventional and logarithmic deformation, are shown in Figs. 3.3 and 3.4, the latter showing the locking in tension typical of rubber-like materials. Note that one curve (sample S1) is slightly

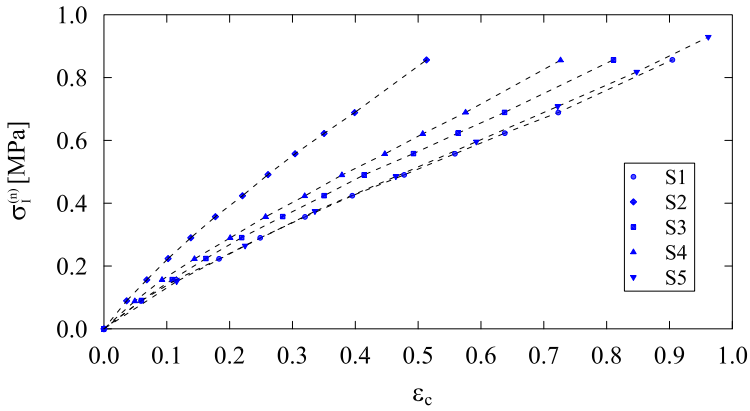

Fig. 3.4: Mechanical properties: applied nominal stress $\sigma_I^{(n)}$ versus conventional deformation ε_c. Experimental data obtained with a uniaxial test at controlled load.

stiffer than the others, due to a spurious oscillation in the temperature during polimerization of the sample.

Turning now the attention to the optical properties, we have measured the isochromatic fringe order N (using the so-called 'Tardy compensation procedure', see Dally and Riley, 1965), together with the nominal stress $\sigma_1^{(n)}$ and the longitudinal and transversal stretches λ_1 and $\lambda_2 = \lambda_3$. From these data, Eq. (3.15) allows to calculate $f_\sigma^{(n)}$ as a function of the in-plane nominal stress difference, and then f_σ is given by Eq. (3.16) as a function of the true stress. Results are plotted in Figs. 3.5 and 3.6.

The experimental results for the true quantities reported in Fig. 3.5 are described by the law

$$f_\sigma = 0.214 + 0.024\,|\Delta\sigma|^{3/2} \ \ [\mathrm{N/mm}], \tag{3.18}$$

while the results in terms of nominal quantities, reported in Fig. 3.6 and more important for our subsequent calculations, are fitted by the law

$$f_\sigma^{(n)} = a + b\,\{\exp(-c\,|\Delta\sigma^{(n)}|) - 1\}, \tag{3.19}$$

where a, b and c are constants, so that the nominal material fringe parameter $f_\sigma^{(n)}$ becomes a function of the *in-plane maximum shear stress* $|\Delta\sigma^{(n)}|/2$. Our experiments indicate the following values for the coefficients in Eq. (3.19)

$$a = 0.214 \ \ [\mathrm{N/mm}], \quad b = 0.038 \ \ [\mathrm{N/mm}], \quad c = 3.245 \ \ [\mathrm{mm^2/N}], \tag{3.20}$$

which provides the nonlinear function of stress plotted in Fig. 3.6 to fit the experimental data. We finally remark that the linearization of the constitutive equations (3.2) [or (3.4)] and of the optical law (3.14) [or (3.15)] leads to the usual setting of linear photoelasticity. However, the stress/strain mechanical problem and the optical problem are decoupled, so that there are no conceptual difficulties in linearizing the former and keeping nonlinear the latter. In fact, in the following we will show that the optimal interpretation of experiments leads us to the use of the linear theory of elasticity for the determination of the stress fields, so that $\Delta\sigma = \Delta\sigma^{(n)}$, employed together with the nonlinear Eq. (3.19) for the optical behaviour of the material.

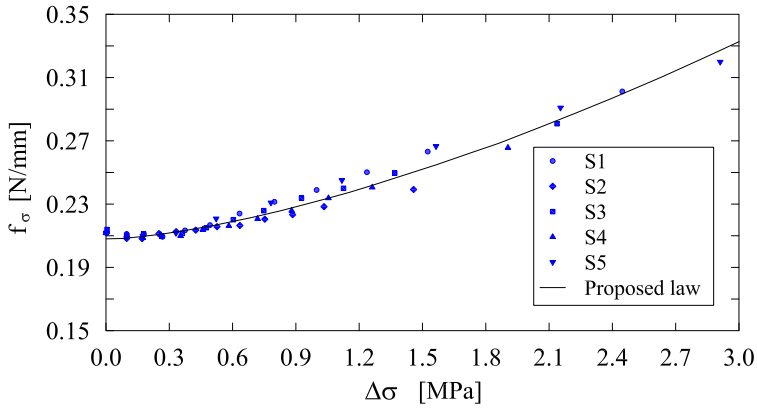

Fig. 3.5: Optical properties: true material fringe parameter f_σ versus true principal stress difference $\Delta\sigma$. Experimental data and proposed law, Eq. (3.18).

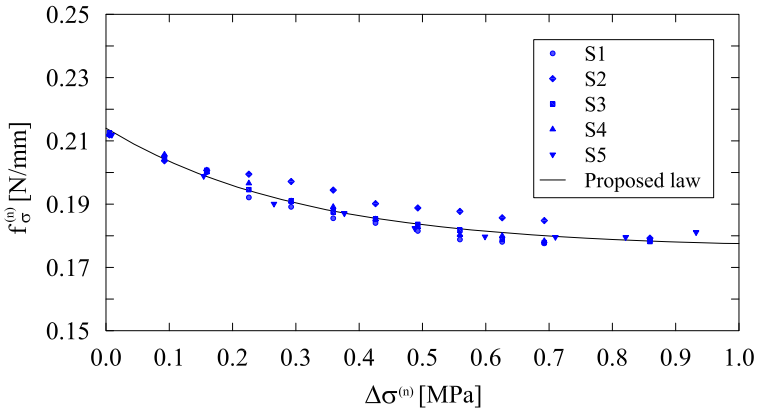

Fig. 3.6: Optical properties: nominal material fringe parameter $f_\sigma^{(n)}$ versus nominal principal stress difference $\Delta\sigma^{(n)}$. Experimental data and proposed law, Eq. (3.19) with the coefficients (3.20).

3.3 Linear elastic solution for a stiffener

It is instrumental now to recall the solution for a rigid line inclusion embedded in a linear elastic matrix. To this purpose, we assume general-

ized plane conditions, so that the displacement field is defined as

$$u_x = u_x(x, y), \qquad u_y = u_y(x, y), \tag{3.21}$$

from which the in-plane deformations $\varepsilon_{\alpha\beta}$ (α, β=x, y) can be obtained as

$$\varepsilon_{xx} = \frac{\partial u_x}{\partial x}, \qquad \varepsilon_{yy} = \frac{\partial u_y}{\partial y}, \qquad \varepsilon_{xy} = \frac{1}{2}\left(\frac{\partial u_x}{\partial y} + \frac{\partial u_y}{\partial x}\right). \tag{3.22}$$

For a linear elastic isotropic material, the relation between deformations (3.22) and stresses $\sigma_{\alpha\beta}$ (α, β=x, y) is given by the in-plane constitutive equations,

$$\begin{aligned} \varepsilon_{xx} &= \frac{(\kappa+1)\sigma_{xx} + (\kappa-3)\sigma_{yy}}{8\mu}, \\ \varepsilon_{yy} &= \frac{(\kappa+1)\sigma_{yy} + (\kappa-3)\sigma_{xx}}{8\mu}, \\ \varepsilon_{xy} &= \frac{\sigma_{xy}}{2\mu}, \end{aligned} \tag{3.23}$$

where μ represents the shear modulus and

$$\kappa = \begin{cases} 3 - 4\nu, & \text{for plane strain,} \\ \dfrac{3-\nu}{1+\nu}, & \text{for plane stress,} \end{cases} \tag{3.24}$$

where $\nu \in (-1, 1/2)$ is the Poisson's ratio. Note that $\kappa = 1$ in the limit case of incompressible material under plane strain.

A rigid line inclusion of length $2\,l$, aligned parallel to and centered at the origin of the x–axis, is considered perfectly bonded to an elastic matrix defined by the constitutive equations (3.23). The presence of such inclusion introduces boundary conditions on the line where the inclusion lies (different from those corresponding to a crack), that can be distinguished in:

- kinematical boundary conditions (expressing the fact that, for points belonging to the inclusion line, the displacements field consists in a generic rigid-body motion)

$$u_x(\xi, 0) = u_x(0, 0), \quad u_y(\xi, 0) = u_y(0, 0) + \omega_S\,\xi, \quad \forall\,|\xi| < l, \tag{3.25}$$

where $u_x(0,0)$, $u_y(0,0)$ represent the unknown generic displacements of the mid-point of the inclusion and ω_S a rigid-body rotation;

- statical boundary conditions (expressing the fact that the resultant forces on the rigid line inclusion have to be null in order to satisfy equilibrium)

$$\begin{aligned} \int_{-l}^{l} [\![\sigma_{xy}(\xi,0)]\!]\, d\xi &= 0, \\ \int_{-l}^{l} [\![\sigma_{yy}(\xi,0)]\!]\, d\xi &= 0, \\ \int_{-l}^{l} [\![\sigma_{yy}(\xi,0)]\!]\, \xi\, d\xi &= 0, \end{aligned} \tag{3.26}$$

where the bracket operator $[\![\cdot]\!]$ denotes the jump in the relevant argument across the inclusion line.

The full-field solution for a stiffener of finite length $2l$ can be obtained using the method of complex potentials for plane problems, where the stress components are expressed in terms of complex potentials $\Phi(z)$ and $\Psi(z)$, function of $z = x + \mathrm{i}\, y$ (where i is the imaginary unit) and defining the stress fields as (Muskhelishvili, 1953)

$$\begin{aligned} \sigma_{xx} &= \mathrm{Re}\left[2\Phi(z) - \overline{z}\Phi'(z) - \Psi(z)\right], \\ \sigma_{yy} &= \mathrm{Re}\left[2\Phi(z) + \overline{z}\Phi'(z) + \Psi(z)\right], \\ \sigma_{xy} &= \mathrm{Im}\left[\overline{z}\Phi'(z) + \Psi(z)\right]. \end{aligned} \tag{3.27}$$

Considering *uniform* Mode I and Mode II loadings[4] described by the remote in-plane stresses σ_{xx}^{∞}, σ_{yy}^{∞} and σ_{xy}^{∞}, the stiffener solution is (Atkin-

[4]The definition of in-plane Mode loadings for the stiffener problem is given in analogy with their equivalent in fracture mechanics, so that Mode I is defined as an in plane symmetric loading, while Mode II is defined as an in plane antisymmetric loading.

son, 1973; see also Ballarini, 1990)

$$\Phi(z) = \frac{\sigma_{xx}^{\infty} + \sigma_{yy}^{\infty}}{4} - \frac{(\kappa+1)\sigma_{xx}^{\infty} + (\kappa-3)\sigma_{yy}^{\infty}}{8\kappa}\left(1 - \frac{z}{\sqrt{z^2 - l^2}}\right),$$

$$\Psi(z) = \frac{\sigma_{yy}^{\infty} - \sigma_{xx}^{\infty}}{2} + \mathrm{i}\,\sigma_{xy}^{\infty} + \frac{(\kappa+1)\sigma_{xx}^{\infty} + (\kappa-3)\sigma_{yy}^{\infty}}{8\kappa} \times \tag{3.28}$$

$$\times \left[1 + \kappa - (2+\kappa)\frac{z}{\sqrt{z^2 - l^2}} + \frac{z^3}{\sqrt{(z^2 - l^2)^3}}\right].$$

Solution (3.28) yields:

- for Mode I loading and due to the symmetry of the problem, a stress state which automatically satisfies conditions (3.26) and leads to

$$\varepsilon_{xx}(\xi, 0) = \varepsilon_{xy}(\xi, 0) = 0, \quad \forall\, |\xi| < l, \tag{3.29}$$

  so that conditions (3.25) are also satisfied with $\omega_S = 0$ and unprescribed $u_x(0,0)$ and $u_y(0,0)$;

- for Mode II loading, a uniform stress state, so that all jumps in Eqs. (3.26) are null and Eqs. (3.25) are satisfied with $\omega_S = \sigma_{xy}^{\infty}/\mu$ and unprescribed $u_x(0,0)$ and $u_y(0,0)$.

Therefore, *differently from the crack problem*, solution (3.28) shows that:

- the mechanical fields depend on the Poisson's ratio through parameter κ, Eq. (3.24);

- the rigid line inclusion perturbs the homogeneous state for stress component parallel to the inclusion, σ_{xx}^{∞}, but it is 'neutral' to stress component σ_{xy}^{∞}, leaving unperturbed[5] the homogeneous shear stress field (see Appendix A for experimental results about stiffener 'neutrality').

[5]The neutrality of a rigid line inclusion occurs only for *uniform* Mode II, indeed a square-root singularity can be found for a generic Mode II loading.

For uniform Mode I loading, the asymptotics of solution (3.28) (taken near the stiffener tip on the right hand side, $z = l + r\exp(\mathrm{i}\theta)$, with small r/l ratio) or, more in general, the asymptotics for an arbitrary Mode I loading leads to an expression for stress and strain fields in the form (Wang *et al.*, 1985)

$$\begin{bmatrix} \sigma_{xx} \\ \sigma_{yy} \\ \sigma_{xy} \end{bmatrix} = \frac{H_I}{\sqrt{2\pi r}} \begin{bmatrix} \cos\frac{\vartheta}{2}\left(\frac{3+\kappa}{2} - \sin\frac{\vartheta}{2}\sin\frac{3\vartheta}{2}\right) \\ \cos\frac{\vartheta}{2}\left(\frac{1-\kappa}{2} + \sin\frac{\vartheta}{2}\sin\frac{3\vartheta}{2}\right) \\ \sin\frac{\vartheta}{2}\left(\frac{1+\kappa}{2} + \cos\frac{\vartheta}{2}\cos\frac{3\vartheta}{2}\right) \end{bmatrix},$$

$$\begin{bmatrix} \varepsilon_{xx} \\ \varepsilon_{yy} \\ \varepsilon_{xy} \end{bmatrix} = \frac{H_I}{2\mu\sqrt{2\pi r}} \begin{bmatrix} \cos\frac{\vartheta}{2}\left(\kappa - \sin\frac{\vartheta}{2}\sin\frac{3\vartheta}{2}\right) \\ -\cos\frac{\vartheta}{2}\left(1 - \sin\frac{\vartheta}{2}\sin\frac{3\vartheta}{2}\right) \\ \sin\frac{\vartheta}{2}\left(\frac{1+\kappa}{2} + \cos\frac{\vartheta}{2}\cos\frac{3\vartheta}{2}\right) \end{bmatrix}, \tag{3.30}$$

where H_I is a Mode I stress intensity factor, which takes different forms according to a normalization criterion. In particular, the usual normalization criterion of fracture mechanics for Mode I loadings gives

$$K_I = \lim_{r\to 0} \sqrt{2\pi r}\,\sigma_{yy}(r, \vartheta = 0) = \frac{1-\kappa}{2}\,H_I, \tag{3.31}$$

which is not well behaved under plane strain condition in the limit of incompressibility, $\kappa = 1$. To emend the problem of incompressibility, in agreement with Wu (1990), we introduce the following normalization

$$K_I^{(\varepsilon)} = \lim_{r\to 0} 2\mu\sqrt{2\pi r}\,\varepsilon_{xx}(r, \vartheta = 0) = \kappa\,H_I. \tag{3.32}$$

From the full-field solution (3.28), we can now obtain the stress intensity factors for a rigid line inclusion under uniform Mode I loading at infinity, following the normalizations (3.31) and (3.32) in the forms

$$K_I = \frac{1-\kappa}{\kappa}\mu\varepsilon_{xx}^{\infty}\sqrt{\pi l}, \qquad K_I^{(\varepsilon)} = 2\mu\varepsilon_{xx}^{\infty}\sqrt{\pi l}. \tag{3.33}$$

Note that the definition (3.32) leads to the stress intensity factor $(3.33)_2$, which is similar to the analogous quantity (where 'remote strain' replaces 'remote stress') obtained for a crack using definition (3.31). The analogy between the two definitions of stress intensity factor is connected to the difference of the fields that are constrained to assume null value within the inclusion, namely, σ_{yy} for the crack and ε_{xx} for the stiffener.

3.4 Experimental

3.4.1 The production of samples containing thin, stiff inclusions

A photoelastic matrix material has been realized employing a commercial two-part epoxy resin (Crystal Resins© by Gedeo, 305 Avenue du pic de Bretagne, 13420 Gemenos, France), commonly used for producing highly transparent non-yellowing casts. Different samples have been made pouring the obtained blend (with resin and hardener in proportion of 1:1) in a PTFE mould (at the bottom of which the stiffener was kept orthogonal with the help of some cyanoacrylate drop used at his centre) and de-moulded after 48 hours during which it has been kept at a constant temperature of 25° C. To realize the stiffener, we have used a 0.1 mm and 0.05 mm thick steel sheets, with a superficial rugosity improved (to enhance adhesion) using a fine (P 500) sandpaper.

With this technique we have realized and tested fifteen samples, which have all given the same qualitative results. For brevity, we report here the results obtained from five samples tested after one week from de-moulding (and labeled S1, S2, S3, S4 and S5 in the following). Samples S1–S4 have dimensions 100 mm × 260 mm × 5 mm (see Fig. 3.7), while sample S5 has a reduced thickness of 3 mm. The samples contain stiffeners centered within the matrix and arranged parallel to the larger side, in particular:

- S1, S2 and S3 contain a single inclusion of thickness 0.1 mm, respectively with length $2l = \{20; 30; 40\}$ mm;
- S4 contains two collinear inclusions of thickness 0.1 mm and length $2l = 20$ mm with their tips at a distance of 10 mm;
- S5 contains a single inclusion of thickness 0.05 mm and length $2l = 30$ mm.

Fig. 3.7: Two-part epoxy resin samples (S1, S2, S3, S4, S5) containing 0.1 mm (samples S1–S4) and 0.05 mm (sample S5) thick steel laminae of different lengths ($\{20; 30; 40\}$ mm for samples S1–S3, 20 mm for sample S4 and 30 mm for sample S5). The thickness of samples S1–S4 is 5 mm, while sample S5 is 3 mm thick.

3.4.2 Photoelastic experiments

Experiments have been performed with a linear and a circular (with quarterwave retarders for 560 nm) polariscope (dark field arrangement and equipped with a white and sodium vapor lightbox at $\lambda = 589.3$ nm, purchased from Tiedemann & Betz), designed by us and manufactured at the University of Trento.[6] Photos have been taken with a Nikon D200 digital camera, equipped with a AF-S micro Nikkor (105 mm, 1:2.8G ED) lens and

[6] A detailed descriptions of our polariscope can be found on http://ssmg.ing.unitn.it while general description of photoelastic experimental techniques can be found in Coker and Filon (1957) and Frocht (1965).

with a AF-S micro Nikkor (70-180 mm, 1:4.5Ű5.6 D) lens for details. Monitoring with a thermocouple connected to a Xplorer GLX Pasco©, temperature near the samples during experiments has been found to lie around 22.5° C, without sensible oscillations. Near-tip fringes have been captured with a Nikon SMZ800 stereozoom microscope equipped with Nikon Plan Apo 0.5x objective and a Nikon DS-Fi1 high-definition color camera head.

The samples have been loaded by prescribing vertical dead loads (parallel to the stiffener) increasing from[7] 0 to 50 N (with steps of 5 N). Data have been acquired after 5 minutes from the load application time in order to damp down the largest amount of viscous deformation, noticed as a settlement of the fringes, which follows displacement stabilization. Releasing the applied load after the maximum amount of 50 N, all the samples at rest showed no perceivably residual stresses in the whole specimen.

In Fig. 3.8 (which is the counterpart of Fig. 3.1, but taken under monochromatic light) photoelastic fringes detected on the samples S1, S2 and S3 loaded at 50 N are compared all together with the linear elastic solution (3.28) in plane strain,[8] with a Poisson's ratio[9] equal to 0.45 and $\sigma_{xx}^{\infty} = 0.116$ MPa, equal to the nominal stress applied to the samples. In order to report results of three samples with different stiffener lengths in the same figure, we have scaled down the photos in a way that all the stiffeners appear to have the same length, so that self-similarity of the elastic solution allows us to conclude that the fringes have to be the same, a circumstance fully verified in the experiments.

We can note from Fig. 3.8 that (i.) the linear elastic solution is in a very good *quantitative* agreement with the photoelastic results and (ii.) being the material almost incompressible, the mid-point of inclusion corresponds to an in-plane pressure stress state, i.e. $\Delta\sigma \approx 0$), so that the zone looks

[7]Note that a further load of 8 N corresponding to the grasp weight has been taken into account.

[8]The state in the vicinity of a stiffener can be considered a plane strain state, since the inclusion imposes null deformation on its surface and therefore even in the out-of-plane direction. The comparison of the fields obtained from the experiments and from the analytical solution under plane strain condition proves the validity of this statement.

[9]For the matrix material employed in our experiments, we have estimated the value of the Poisson's ratio using optical measurements, performed until large deformations occurred. Due to the known difficulties in measuring the Poisson's ratio, these measures have to be taken with care, so that we have estimated $\nu = 0.45$, with an error that can arrive to 20%.

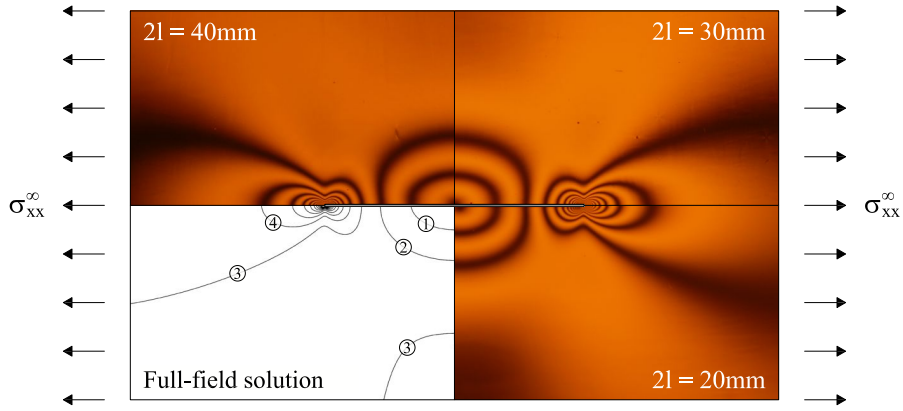

Fig. 3.8: Monochromatic photoelastic fringes revealing the in-plane principal stress difference field near a thin line inclusion (a 0.1 mm thick steel platelet) embedded in an elastic matrix (a two-component 'soft' epoxy resin) compared to the elastic solution (in plane strain, with Poisson's ratio equal to 0.45). The image is the composition of three different photos taken for different stiffener lengths [$2l$ = 20 mm (sample S1), 30 mm (sample S2), and 40 mm (sample S3)], scaled down according to self-similarity to provide the same stress fields.

black and the fringe order is 0.

3.4.3 Hunting the near-tip singular field

Singularities cannot exist in reality, since the stress cannot become infinite in any real material. However, the investigation of the behaviour in vicinity of a singularity is of crucial importance in assessing an elastic solution and its domain of validity.

For all samples, the count of fringes has been possible directly on the photos, producing results shown in Figs. 3.2, 3.9 and 3.11, where the stress along the stiffener line $y = 0$ is reported for the experimental quantifications and compared with the asymptotic and full-field elastic solutions. Differently from samples S1 and S3, the specimen S2 was optically pure until near the tip of the stiffener (in the outside region), so that, with the aid of an optical stereomicroscope (a Nikon SMZ800), we have been able to detail the very near-tip fringes in the direction outward to the stiffener (in the inward direction the optical purity was compromised by the

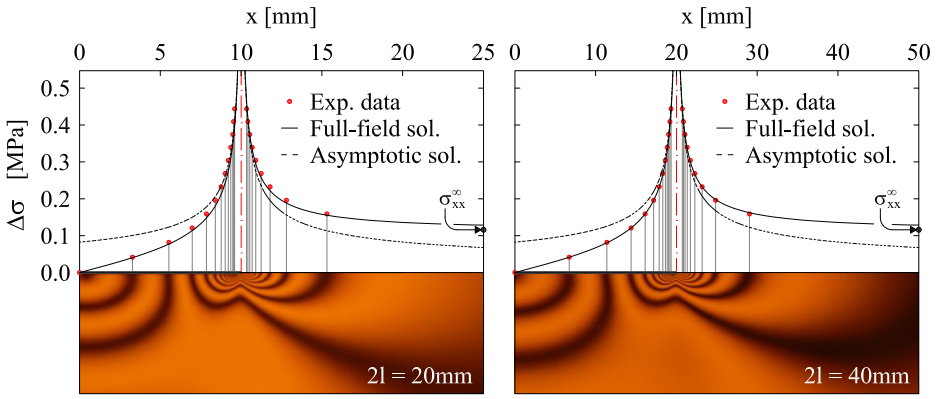

Fig. 3.9: In-plane principal stress difference along the stiffener line (y =0): comparison between photoelastic experiments at monochromatic light on samples S1 (left), S3 (right) and the (full-field and asymptotic) elastic solutions for remote stress σ^{∞}_{xx}= 0.116 MPa.

cyanoacrylate used to fix the stiffener before pouring the resin), until a distance from the tip of the same order of the stiffener thickness (0.1 mm), see Fig. 3.2. It has been possible to count twenty different fringes, corre-

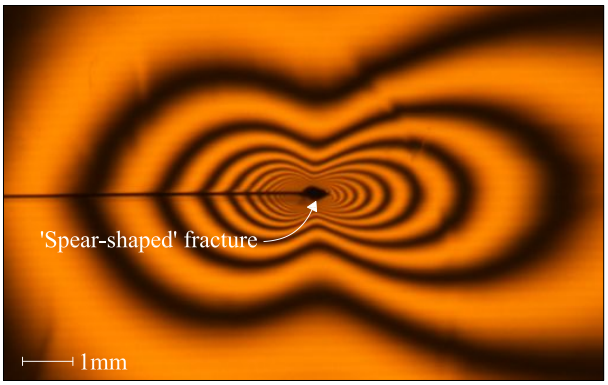

Fig. 3.10: Monochromatic photoelastic fringes near the stiffener tip of sample S5, which has suffered a delayed failure. A 'spear-shaped' microscopic fracture is visible at the tip of the stiffener (having a thickness 0.05 mm).

sponding to a stress concentration equal to seven. A stress concentration equal to eight has been obtained testing sample S5, which however has suffered a delayed near-tip microscopic failure just an instant after we had finished counting twenty-three fringes.

The near-stiffener failure of specimen S5 is shown in Fig. 3.10 (taken with the Nikon SMZ800 stereomicroscope), evidencing a 'spear' shape of the near-tip fracture, which we have found to be the typical failure mode in all our samples (see also Dal Corso *et al.*, 2008, their Fig. 7).

Although our experiments are not conclusive on this aspect, debonding is not observed along the long edges defining the stiffener line, so that the spear-shaped fracture seems to involve debonding only along the short edge ($0.05\,\text{mm} \times 3\,\text{mm}$ in the experiment reported in Fig. 3.10) of the stiffener tip. Considering the Figs. 3.9 and 3.2, we may observe that the stress

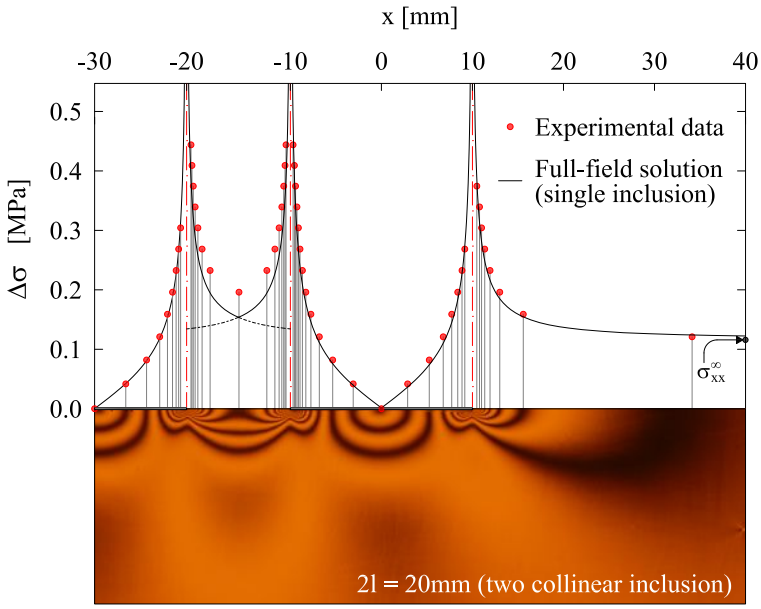

Fig. 3.11: In-plane principal stress difference along the stiffener line (y =0): comparison between photoelastic experiment at monochromatic light on sample S4 (containing two stiffeners) and the full-field elastic solution relative to a single stiffener, for remote stress σ^{∞}_{xx}=0.116 MPa. Note that the distance between the stiffeners (equal to the inclusion half-length) is not close enough that to invalidate the single inclusion solution.

raises near the tip of the stiffener in very good quantitative agreement with the elastic solution, to decrease at a distance $1.5l$ to 110% of the remote stress σ_{xx}^{∞}.

From these figures we may note that the elastic solution remains valid until very near to the stiffener tip (0.1 mm), so that the asymptotic approximation has a range of validity in an annular zone with an external radius equal to $l/3$ (and corresponding to a 20% discrepancy with the full-field solution).

A special comment is related to Fig. 3.11, where we see that the interaction between two collinear stiffeners (when their tips are at a distance l from each other) is not strong enough to completely invalidate the solution for the single stiffener, which is still shown to reproduce very well the stress field in the experiment.

In closure of this Section we mention that, although all our experimental results have been interpreted using the nonlinear law for the fringe material parameter $f_{\sigma}^{(n)}$, Eq. (3.19), the assumption of a constant value for the fringe material parameter does not alter substantially results. A discussion on this point is deferred to Appendix B.

3.4.4 Determination of stress intensity factor $K_I^{(\varepsilon)}$

In the literature, photoelastic experiments on fracture have mainly been conducted with the purpose of providing a quantitative description of the introduced singularity through the determination of the stress intensity factor K_I, a quantity which is usually determined through the so-called 'two– three– and four– parameter methods' (reviewed by Østervig, 1987), based on a procedure proposed by Irwin (1958). However, our purpose here is different, since we want to experimentally validate the analytical value of stress intensity factor $K_I^{(\varepsilon)}$ for a uniform Mode I at infinity, Eq. $(3.33)_2$. To this purpose, we note that applying the two–parameter method (Irwin, 1958) to the asymptotics of the stiffener (3.30), the introduction of a 'uniform stress parameter' yields unrealistic (experimentally not observed) corners of the predicted fringes along the stiffener line. For this reason, instead using the two–parameter method or its variants, we have found more suited the recent approach proposed by Chen (1996) based on the experimental measure of the area enclosed within two

isochromatic fringes.

Following this approach, the area between two isochromatic fringes can be related to the stress intensity factor via the asymptotic solution and the optical properties of the material. Applied to the rigid line inclusion problem, the stress intensity factor takes an expression different from that defined for a crack, which is the following (referred to two different fringes numbered N and M and the associated nominal quantities)

$$K_I^{(\varepsilon)} = 2\kappa \frac{M f_{\sigma,M}^{(n)} N f_{\sigma,N}^{(n)}}{t_0} \times \times \sqrt[4]{\frac{2\pi\,(A_N - A_M)}{(8\kappa^4 + 16\kappa^3 + 20\kappa^2 + 12\kappa + 3)\left[(M f_{\sigma,M}^{(n)})^4 - (N f_{\sigma,N}^{(n)})^4\right]}}, \tag{3.34}$$

where A_i $(i = N, M)$ is the area enclosed within the two isochromatic fringes with order N and M, representing the only quantity that has to be measured in order to estimate the stress intensity factor $K_I^{(\varepsilon)}$.

Reference Area	Fringe orders N - M	$(A_N - A_M)/l^2$			Mean	Variance
		S1	S2	S3		
$2-$ left	$5-6$	0.0171	0.0174	0.0153	0.0166	0.1345×10^{-5}
	$6-7$	0.0094	0.0087	0.0071	0.0084	0.1409×10^{-5}
	$7-8$	0.0058	0.0045	0.0038	0.0047	0.1017×10^{-5}
$2-$ right	$5-6$	0.0511	0.0479	0.0394	0.0461	3.6347×10^{-5}
	$6-7$	0.0183	0.0180	0.0152	0.0172	0.2907×10^{-5}
	$7-8$	0.0087	0.0084	0.0071	0.0080	0.0667×10^{-5}
total	$5-6$	0.0341	0.0326	0.0273	0.0314	1.2706×10^{-5}
	$6-7$	0.0139	0.0133	0.0112	0.0128	0.2068×10^{-5}
	$7-8$	0.0072	0.0064	0.0054	0.0064	0.0786×10^{-5}

Tab. 3.1: Measures of the area between fringes N and M (divided by the square of the stiffener length) $(A_N - A_M)/l^2$ for the fringe patterns shown in Figs. 3.2 and 3.9.

Since formula (3.34) is obtained from the Mode I asymptotic fields (3.30), its application becomes more accurate the closer are the fringes to the stiffener tip. However, the asymptotic solution (referring for the moment to the right stiffener tip) evidences a symmetry (with respect to $x = +l$) of the areas between two fringes, which cannot be perfectly verified in any real experiment. Therefore, we propose the three estimates

of $K_I^{(\varepsilon)}$ which give the same results, would the symmetry be exactly verified. In addition to the direct measure of the area between two fringes, labeled 'total' in Tab. 3.1, we propose the measure labeled '2-left' (labeled '2-right'), corresponding to twice the area enclosed between two fringes observed for $x \leq l$ (for $x \geq l$). Note that 'total' corresponds to the average of '2 left' and '2 right'. The data reported in Tab. 3.1 have been measured with reference to the fringe patterns shown in Figs. 3.2 and 3.9. The measures of the area between fringes has been normalized through division by the square of the stiffener length. From the values reported in

Reference Area	Fringe orders N - M	$K_{I,exp}^{(\varepsilon)}/K_{I,th}^{(\varepsilon)}$			Mean	Variance
		S1	S2	S3		
$2-$ left	$5-6$	0.9216	0.9253	0.8954	0.9141	0.2657×10^{-3}
	$6-7$	0.9716	0.9510	0.9049	0.9425	1.1664×10^{-3}
	$7-8$	1.0190	0.9572	0.9167	0.9643	2.6541×10^{-3}
$2-$ right	$5-6$	1.2111	1.1918	1.1350	1.1793	1.5650×10^{-3}
	$6-7$	1.1468	1.1418	1.0948	1.1278	0.8230×10^{-3}
	$7-8$	1.1287	1.1187	1.0745	1.1073	0.8319×10^{-3}
total	$5-6$	1.0947	1.0829	1.0358	1.0711	0.9711×10^{-3}
	$6-7$	1.0699	1.0592	1.0132	1.0474	0.9076×10^{-3}
	$7-8$	1.0780	1.0475	1.0049	1.0435	1.3481×10^{-3}

Tab. 3.2: Estimate of the ratio between measured and theoretical stress intensity factor, $K_{I,exp}^{(\varepsilon)}/K_{I,th}^{(\varepsilon)}$, for the fringe patterns shown in Figs. 3.2 and 3.9 obtained with the area reported in Tab. 3.1.A value of 1 means perfect adherence between theory and measured values.

Tab. 3.1, the estimations of stress intensity factor $K_I^{(\varepsilon)}$ have been calculated with Eq. (3.34) and reported in Fig. 3.12 and in Tab. 3.2 (where the ratio between experimental $K_{I,exp}^{(\varepsilon)}$ and theoretical[10] $K_{I,th}^{(\varepsilon)}$ values of stress intensity factors is reported, so that value of 1 means perfect adherence between theory and measure).

From Tab. 3.2 we can conclude that:

- the values of $K_{I,exp}^{(\varepsilon)}/K_{I,th}^{(\varepsilon)}$ range between the minimum value of 0.8954 and the maximum of 1.2111, with a mean value 1.0442 and a standard deviation 0.0903;

[10]The theoretical values of the stress intensity factor $K_{I,th}^{(\varepsilon)}$ have been calculated from Eq. $(3.33)_2$ under plane strain condition, using the estimated Poisson's ratio and the remote stress σ_{xx}^{∞}=0.116 MPa.

- fringes closer to the stiffener tip give smaller error in the estimation of stress intensity factor;
- at same fringe order, the smaller error in the estimation of stress intensity factor is obtained for the '2- left' area criterion.

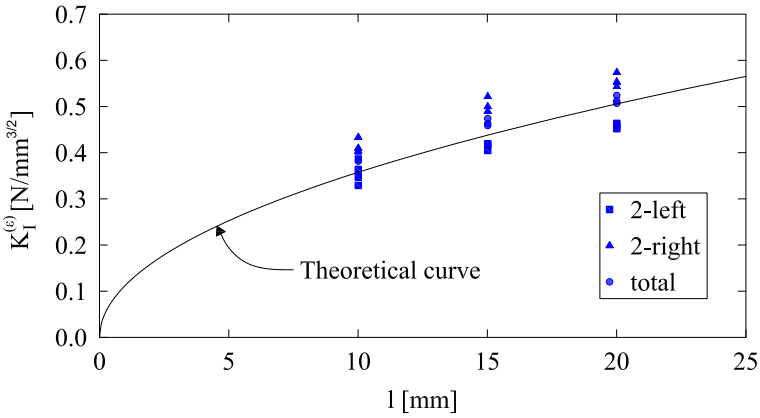

Fig. 3.12: Stress intensity factor $K_I^{(\varepsilon)}$ versus semi-length of stiffener, l. Theoretical curve and measured values, the latter reported in Tab. 3.2.

3.5 Conclusions

The *singular* stress field around a rigid line inclusion in an elastic matrix represents an *excellent approximation* to the photoelastic fringes visible in a two-component epoxy resin material containing thin steel laminae. The experiments provide a superb quantitative validation of the elastic model until a distance from the inclusion tip on the same order of its thickness and corresponding to a stress concentration up to seven. An accurate estimation of the stress intensity factor has been provided by extension of a method used for fracture.

A Stiffener neutrality under uniform Mode II loading conditions (uniform shear parallel to the inclusion line)

The stiffener neutrality to uniform shear stress states has been experimentally verified imposing to the sample S2 a simple shear deformation parallel to the inclusion.

The shear deformation has been estimated from the deformation of a rectangle drawn (with a pen on the sample surface) with the edges parallel and orthogonal to the inclusion line in the undeformed configuration (Fig. 3.13 on the left).

Photoelastic results of the simple shear test are reported in Fig. 3.13, where global shear strain ε_{xy} is (approximately) 2.5% (centre) and 5% (right). Higher deformations were precluded by out-of-plane buckling of the sample.

From the figure we conclude that the stiffener leaves almost unperturbed the imposed shear stress state, so that concentration of stress around the inclusion is not visible. Note that this shear deformation, $\varepsilon^{\infty}_{xy}$, is quantitatively equivalent to the maximum elongation, $\varepsilon^{\infty}_{xx}$, imposed during the experiments described in Section 3.4.2 and disclosing a strong focussing of the stress/strain field around the stiffener tips.

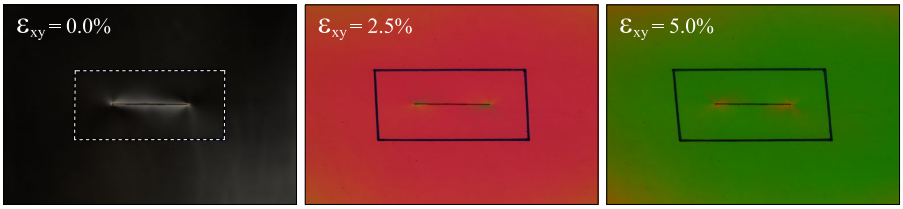

Fig. 3.13: Photoelastic fringes for in-plane principal stress difference around a stiffener subjected to a simple shear ($\varepsilon^{\infty}_{xy}$) parallel to the inclusion line at different stages of deformation ($\varepsilon^{\infty}_{xy} = \{0; 2.5; 5\}\,\%$). The shearing deformation can be estimated from the distortion of the rectangle drawn (with a pen on the surface of the sample) with edges parallel and orthogonal to the stiffener in the unloaded configuration (on the left). The homogeneity of the fields demonstrates the stiffener neutrality for uniform Mode II loading.

B Results obtained with constant material fringe parameter

All our experimental results have been interpreted using the nonlinear law for the fringe material parameter $f_\sigma^{(n)}$, Eq. (3.19), but the the assumption of a constant value for the fringe material parameter does not alter qualitatively results. It may be therefore of interest to quantify how the data result quantitatively affected.

The photoelastic fringes shown in Fig. 3.8 are reported in Fig. 3.14 and compared this time to the theoretical elastic solution assuming a constant value for $f_\sigma^{(n)}$ (equal to 0.196 N/mm, the mean value of the measures), instead of the law (3.19).

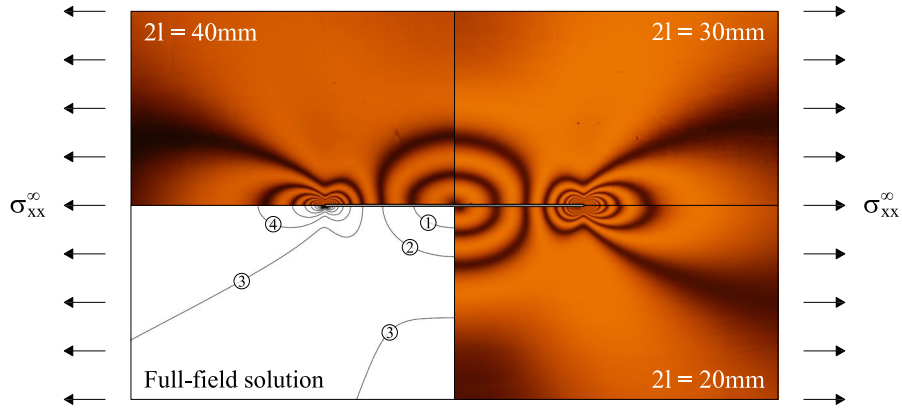

Fig. 3.14: As for Fig. 3.8, but for constant fringe parameter $f_\sigma^{(n)} = 0.196\,\mathrm{N/mm}$ (mean value obtained from the tests).

Globally, we note a good agreement, although a close comparison to Fig. 3.8 reveals some discrepancies, particularly, in the behaviour of the third fringe in the elastic solution.

The most evident differences arise near the stiffener tips, so that in Fig. 3.15 we report a detail of the near-tip fringes of Fig. 3.14 (referred to $2l = 40\,\mathrm{mm}$), compared with the two interpretations based on the law (3.19) (labeled 'Proposed law') and the mean value $f_\sigma^{(n)} = 0.196\,\mathrm{N/mm}$ (labeled 'Mean value').

Finally, the ratio has been calculated between the values of the stress

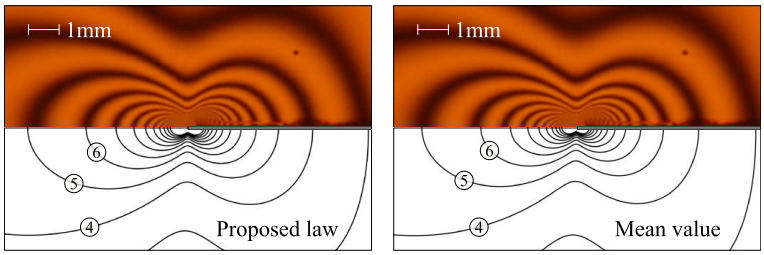

Fig. 3.15: Details of the left stiffener tip of Figs. 3.8 (on the left) and 3.14 (on the right). The elastic fields in the former figure have been obtained with the nonlinear law (3.19), while the latter with the constant value $f_\sigma^{(n)} = 0.196\,\mathrm{N/mm}$.

intensity factors experimentally deduced ($K_{I,exp}^{(\varepsilon)}$) assuming a constant fringe parameter $f_\sigma^{(n)}$, and theoretically determined ($K_{I,th}^{(\varepsilon)}$). These ratios result very similar to the analogous values evaluated for variable fringe parameter $f_\sigma^{(n)}$ and reported in Tab. 3.2. The fact that these values are in close agreement follows from the circumstance that the stress intensity factors have been evaluated working on fringes N=5, 6, 7, 8, where $f_{\sigma,N}^{(n)}$ is very close to the mean value $f_\sigma^{(n)} = 0.196\,\mathrm{N/mm}$.

CHAPTER
FOUR

STRUCTURES BUCKLING UNDER TENSILE DEAD LOAD

After the systematic experiments by Musschenbroek and their rationalization by Euler, for the first time we show that it is possible to design structures (i.e. mechanical systems whose elements are governed by the equations of the elastica) exhibiting bifurcations and instabilities ('buckling') under tensile load of constant direction and point of application ('dead'). We show both theoretically and experimentally that the behaviour is possible in elementary structures with a single degree of freedom and in more complex mechanical systems, as related to the presence of a structural junction, called 'slider', allowing only relative transversal displacement between the connected elements. In continuous systems where the slider connects two elastic thin rods, bifurcations occur both in tension and compression and are governed by the equation of the elastica, employed here for tensile loading, so that the deformed rods take the form of the capillary curve in a liquid, which is in fact governed by the equation of the elastica under tension. Since axial load in structural elements deeply influences dynamics, our results may provide application to innovative actuators for mechanical wave control, moreover, they open a new perspective in the understanding of failure within structural elements.

4.1 Introduction

Buckling of a straight elastic column subject to *compressive* end thrust occurs at a critical load for which the straight configuration of the column

becomes unstable and simultaneously ceases to be the unique solution of the elastic problem (so that instability and bifurcation are concomitant phenomena). Buckling is known from ancient times: it has been experimentally investigated in a systematic way by Pieter van Musschenbrok (1692-1761) and mathematically solved by Leonhard Euler (1707-1783), who derived the differential equation governing the behaviour of a thin elastic rod suffering a large bending, the so-called 'elastica' (see Love, 1927).

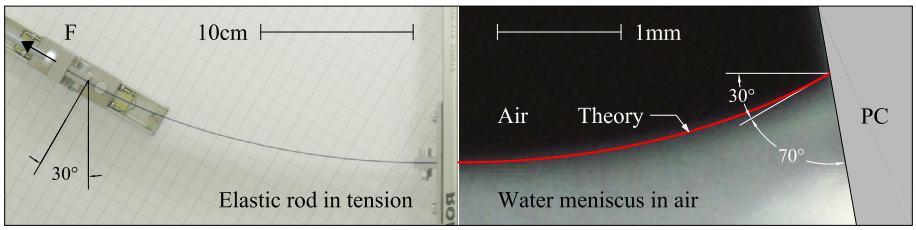

Fig. 4.1: Analogy between an elastic rod buckled under tensile force (left) and a water meniscus in a capillary channel (right, superimposed to the solution of the elastica, marked in red): the deflection of the rod and the surface of the liquid have the same shape, see Section 4.4.

Through centuries, engineers have experimented and calculated complex structures, such as frames, plates and cylinders, manifesting instabilities and bifurcations of various forms (Timoshenko and Gere, 1961), so that certain instabilities have been found involving tensile loads. For instance, there are examples classified by Ziegler (1977) as 'buckling by tension' where a tensile loading is applied to a system in which a compressed member is always present, so that they do not represent true bifurcations under tensile loads. Other examples given by Gajewski and Palej (1974) are all related to the complex *live* (as opposed to 'dead') loading system, for instance, loading through a vessel filled with a liquid, so that Zyczkowski (1991) points out that 'With Eulerian behaviour of loading (materially fixed point of application, direction fixed in space), the bar cannot lose stability at all [...].' Note finally that necking of a circular bar represents a bifurcation of a material element under tension, not of a structure.

It can be concluded that until now *structures made up of line elements*

(each governed by the equation of the elastica) exhibiting bifurcation and instability under tensile load of fixed direction and point of application (in other words 'dead') have never been found, so that the word 'buckling' is commonly associated to compressive loads.

In the present article we show that:

- simple structures can be designed evidencing bifurcation (buckling) and instability under tensile dead loading;
- the deformed shapes of these structures can be calculated using the equation of the elastica, but under tension, so that the deflection of the rod is identical to the shape of a capillary curve in a liquid, which is governed by the same equation, see Fig. 4.1 and Sections 4.3.2 and 4.4;
- experiments show that elastic structures buckling under tension can be realized in practice and that they closely follow theory predictions, Sections 4.2 and 4.4.

The above findings are complemented by a series of minor new results for which our system behaves differently from other systems made up of elastic rods, but with the usual end conditions. First, our system evidences load decrease with increase of axial displacement (the so-called 'softening'), second, the bifurcated paths involving relative displacement at the slider terminate at an unloaded limit configuration, for both tension and compression.

We will see that the above results follow from a novel use of a junction between mechanical parts, namely, a *slider* or, in other words, a connection allowing only relative sliding (transverse displacement) between the connected pieces and therefore constraining the relative rotation and axial displacement to remain null.

Vibrations of structures are deeply influenced by axial load, so that the speed of flexural waves vanishes at bifurcation (Bigoni *et al.* 2008; Gei *et al.* 2009), a feature also evidenced by the dynamical analysis presented in Section 4.3.1, so that, since bifurcation is shown to occur in our structures both in tension and compression, these can be used as two-way actuators for mechanical waves, where the axial force controls the speed of the waves traversing the structure. Therefore, the mechanical systems invented in

the present article can immediately be generalized and employed to design complex mechanical systems exhibiting bifurcations in tension and compression, to be used, for instance, as systems with specially designed vibrational properties (a movie providing a simple illustration of the concepts exposed in this work, together with a view of experimental results is provided, see http://ssmg.ing.unitn.it).

4.2 A simple one d.o.f. structure which buckles for tensile dead loading

The best way to understand how a structure can bifurcate under tensile dead loading is to consider the elementary single-degree-of-freedom structure shown in Fig. 4.2, where two rigid rods are connected through a 'slider' (a device which imposes the same rotation angle and axial displacement to the two connected pieces, but null shear transmission, leaving only the possibility of relative sliding). Bifurcation load and equilibrium

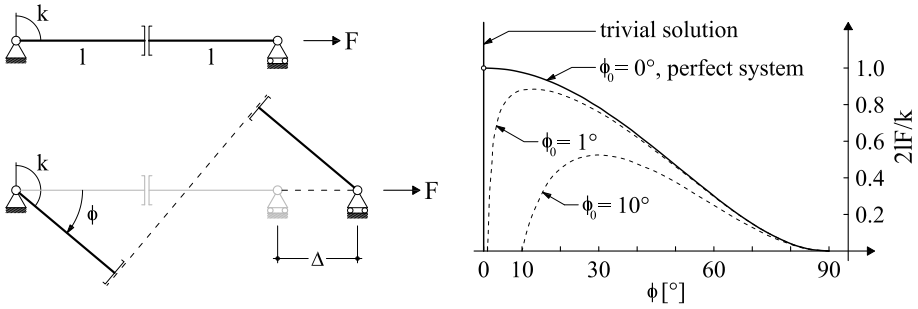

Fig. 4.2: Bifurcation of a single-degree-of-freedom elastic system under *tensile dead loading* (the rods of length l are rigid and jointed through a slider, a device allowing only for relative sliding between the two connected pieces). A rotational elastic spring of stiffness k, attached at the hinge on the left, provides the elastic stiffness. Note that the bifurcation is 'purely geometrical' and is related to the presence of the constraint at the middle of the beam which transmits rotation, but not shear (left). The bifurcation diagram, showing bifurcation and softening in tension is reported on the right. The rotation angle $\phi_0 = \{1°, 10°\}$ denotes an initial imperfection, in terms of an initial inclination of the two rods with respect to the horizontal direction.

paths of this single-degree-of-freedom structure can be calculated by con-

sidering the bifurcation mode illustrated in Fig. 4.2 and defined by the rotation angle ϕ. The elongation of the system and the potential energy are respectively

$$\Delta = 2l\left(\frac{1}{\cos\phi} - 1\right) \tag{4.1}$$

and

$$W(\phi) = \frac{1}{2}k\phi^2 - 2Fl\left(\frac{1}{\cos\phi} - 1\right), \tag{4.2}$$

so that solutions of the equilibrium problem are

$$F = \frac{k\,\phi\,\cos^2\phi}{2l\sin\phi}, \tag{4.3}$$

for $\phi \neq 0$, plus the trivial solution ($\phi = 0,\ \forall F$). Analysis of the second-order derivative of the strain energy reveals that the trivial solution is stable up to the critical load

$$F_{cr} = \frac{k}{2l}, \tag{4.4}$$

while the nontrivial path, *evidencing softening*, is unstable.

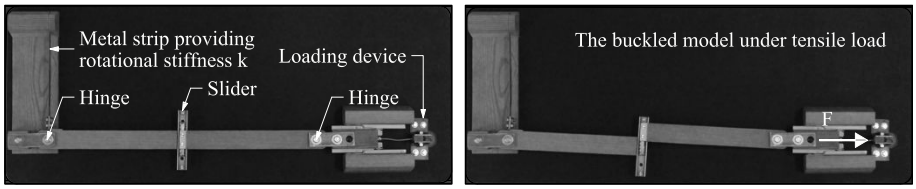

Fig. 4.3: A model of the single-degree-of-freedom elastic structure shown in Fig. 4.2 on the left (in which a metal strip reproduces the rotational spring and the load is given through hanging a load) displaying bifurcation for tensile dead loading (left: undeformed configuration; right: buckled configuration).

For an imperfect system, characterized by an initial inclination of the rods ϕ_0, we obtain

$$W(\phi, \phi_0) = \frac{1}{2}k\left(\phi - \phi_0\right)^2 - 2Fl\left(\frac{1}{\cos\phi} - \frac{1}{\cos\phi_0}\right) \tag{4.5}$$

and

$$F = \frac{k\,(\phi - \phi_0)\,\cos^2\phi}{2l\sin\phi}, \tag{4.6}$$

so that the force–rotation relation is obtained, which is reported dashed in Fig. 4.2 for $\phi_0 = 1^\circ$ and $\phi_0 = 10^\circ$.

The simple structure presented in Fig. 4.2, showing possibility of a bifurcation under dead load in tension and displaying an overall softening behaviour, can be realized in practice, as shown by the wooden model reported in Fig. 4.3.

4.3 Vibrations, buckling and the elastica for a structure subject to tensile (and compressive) dead loading

In order to generalize the single-degree-of-freedom system model into an elastic structure, we consider two *inextensible* elastic rods clamped at one end and joined through a slider, identical to that used to join the two rigid bars employed for the single-degree-of-freedom system (see the inset of Fig. 4.4). The two bars have bending stiffness B, length l^- (on the left) and l^+ (on the right) and are subject to a load F which may be tensile ($F > 0$) or compressive ($F < 0$).

4.3.1 The vibrations and critical loads

The differential equation governing the dynamics of an elastic rod subject to an axial force F (assumed positive if tensile) is

$$\frac{\partial^4 v(z,t)}{\partial z^4} - \frac{F}{B}\frac{\partial^2 v(z,t)}{\partial z^2} + \frac{\rho}{B}\frac{\partial^2 v(z,t)}{\partial t^2} = 0, \tag{4.7}$$

where ρ is the unit-length mass density of the rod and v the transversal displacement, so that time-harmonic motion is based on the separate-variable representation

$$v(z,t) = \tilde{v}(z)\,e^{-i\omega t}, \tag{4.8}$$

in which ω is the circular frequency, t is the time and $i = \sqrt{-1}$ is the imaginary unit.

A substitution of Eq. (4.8) into Eq. (4.7) yields the equation governing time-harmonic oscillations

$$\frac{d^4\tilde{v}(z)}{dz^4} - \alpha^2\,\mathrm{sign}(F)\,\frac{d^2\tilde{v}(z)}{dz^2} - \beta\tilde{v}(z) = 0, \tag{4.9}$$

where the function 'sign' (defined as $\mathrm{sign}(\alpha) = |\alpha|/\alpha\ \forall\alpha \in \mathrm{Re}$ and $\mathrm{sign}(0) = 0$) has been used and

$$\alpha^2 = \frac{|F|}{B}, \quad \beta = \omega^2\frac{\rho}{B}. \tag{4.10}$$

The general solution of Eq. (4.9) is

$$\tilde{v}(z) = C_1\cosh(\lambda_1 z) + C_2\sinh(\lambda_1 z) + C_3\cos(\lambda_2 z) + C_4\sin(\lambda_2 z), \tag{4.11}$$

where

$$\lambda_{1,2} = \sqrt{\frac{\sqrt{\alpha^4 + 4\beta} \pm \alpha^2\,\mathrm{sign}(F)}{2}}. \tag{4.12}$$

Eq. (4.11) holds both for the rod on the left (transversal displacement denoted with '$-$') and on the right (transversal displacement denoted with '$+$') shown in the inset of Fig. 4.4, so that the boundary conditions at the clamps impose

$$\tilde{v}^-(0) = \left.\frac{d\tilde{v}^-}{dz}\right|_{z=0} = 0, \quad \tilde{v}^+(l^+) = \left.\frac{d\tilde{v}^+}{dz}\right|_{z=l^+} = 0, \tag{4.13}$$

while at the slider we have the two conditions

$$\left.\frac{d^3\tilde{v}^-}{dz^3}\right|_{z=l^-} = \left.\frac{d^3\tilde{v}^+}{dz^3}\right|_{z=0} = 0, \tag{4.14}$$

expressing the vanishing of the shear force. The imposition of the six conditions (4.13)–(4.14) provides the constants $C^{\pm}_{2,3,4}$ as functions of the constants $C^{\pm}_1$, so that the continuity of the rotation at the slider

$$\left.\frac{d\tilde{v}^-}{dz}\right|_{z=l^-} = \left.\frac{d\tilde{v}^+}{dz}\right|_{z=0} \tag{4.15}$$

and the equilibrium of the slider

$$\left.\frac{d^2\tilde{v}^-}{dz^2}\right|_{z=l^-} - \alpha^2\,\mathrm{sign}(F)\ \tilde{v}^-(l^-) = \left.\frac{d^2\tilde{v}^+}{dz^2}\right|_{z=0} - \alpha^2\,\mathrm{sign}(F)\ \tilde{v}^+(0), \tag{4.16}$$

yields finally a linear homogeneous system (with unknowns C_1^- and C_1^+), whose determinant has to be set equal to zero, to obtain the frequency equation, function of α^2, ω and sign(F). The circular frequency ω (normalized through multiplication by $\sqrt{\rho l^4/B}$) versus the axial force (normalized through multiplication by $4l^2/(B\pi^2)$) is reported in Fig. 4.4, where the first four branches are shown for a system of two rods of equal length. In this figure the gray zones represent situations that cannot be achieved,

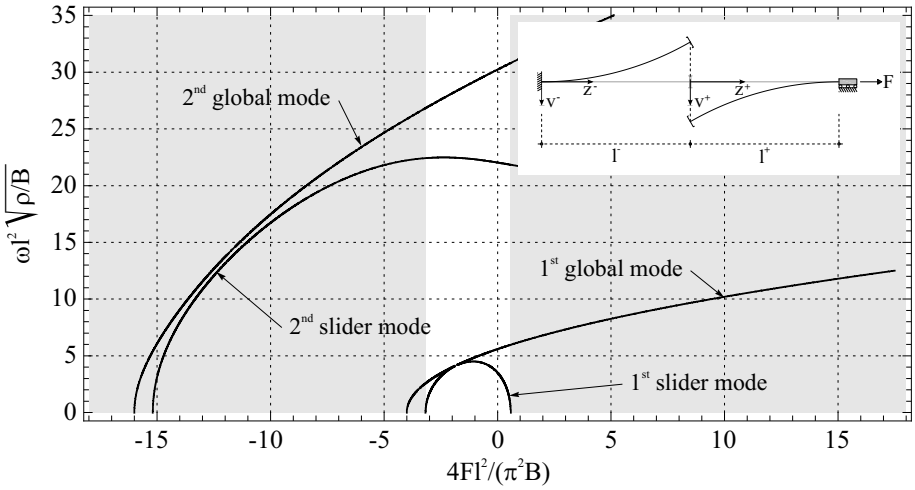

Fig. 4.4: Dimensionless circular frequency ω for the structure shown in the inset (in the particular case of rods of equal length, l) as a function of the dimensionless applied load F. Note that solutions in the gray region cannot be achieved, since the rods cannot remain straight for axial forces external to the bifurcation range of loads (shown as a white zone).

in the sense that the axial force falls outside the interval where the straight configuration of the system is feasible (in other words, for axial loads external to the interval of first bifurcations in tension and compression the straight configuration cannot be maintained).

The branches shown in Fig. 4.4 intersect the horizontal axis in correspondence to the bifurcation loads of the system, namely, $4F_{cr}l^2/(\pi^2 B) = -16, -15.19, -4, -3.17, +0.58$, so that there is one critical load in tension (the corresponding branch is labeled '1$^{\text{st}}$ slider mode' in Fig. 4.4), and infinitely many bifurcation loads in compression, the first three are reported

in Fig. 4.4 (bifurcations corresponding to the label 'global mode' do not involve relative displacement across the slider).

Beside the possibility of bifurcation in tension, an interesting and novel effect related to the presence of the slider is that a tensile (compressive) axial force yields a decrease (increase) of the frequency of the system, while an opposite effect is achieved when 'global modes' are activated.

Quasi-static solutions of the system and related bifurcations can be obtained in the limit $\omega \to 0$ of the *frequency equation*, which yields

$$\begin{cases} \tanh\left(\alpha\, l^-\right)\cosh\left(\alpha\, l^+\right) + \\ +\sinh\left(\alpha\, l^+\right)\left[1-\left(l^+ + l^-\right)\alpha\tanh\left(\alpha\, l^-\right)\right] = 0, & \text{for } F>0, \\ \tan\left(\alpha\, l^-\right)\cos\left(\alpha\, l^+\right) + \\ +\sin\left(\alpha\, l^+\right)\left[1+\left(l^+ + l^-\right)\alpha\tan\left(\alpha\, l^-\right)\right] = 0, & \text{for } F<0. \end{cases} \tag{4.17}$$

In the particular case of rods of equal length l, Eqs. (4.17) simplify to

$$\begin{cases} \sinh\left(\alpha\, l\right)\left[1-\alpha\, l\,\tanh\left(\alpha\, l\right)\right] = 0, & \text{for } F>0, \\ \sin\left(\alpha\, l\right)\left[1+\alpha\, l\,\tan\left(\alpha\, l\right)\right] = 0, & \text{for } F<0. \end{cases} \tag{4.18}$$

Eqs. (4.18) show clearly that *there is only one bifurcation load in tension* (branch labeled '1^{st} slider mode' in Fig. 4.4), but there are ∞^2 bifurcation loads in compression (the first three branches are reported in Fig. 4.4). In compression, the bifurcation condition $\sin\left(\alpha\, l\right) = 0$, providing ∞^1 solutions, yields the critical loads of a doubly clamped beam of length $2l$ and defines what we have labeled 'global modes' in Fig. 4.4. Bifurcation loads, normalized through multiplication by $(l^+ + l^-)^2/(\pi^2 B)$, are reported in Fig. 4.5 as functions of the ratio l^+/l^- between the lengths of the two rods.

Note that the graph is plotted in a semi-logarithmic scale, which enforces symmetry about the vertical axis. In the graph, the first two buckling loads in compression are reported: the first corresponds to a mode involving sliding, while the second does not involve any sliding (and when $l^+ = l^-$ corresponds to the first mode of a doubly clamped rod of length $2l$). Used as an optimization parameter, $l^+ = l^-$ corresponds to the lower bifurcation load in tension ($+0.58$), near five times smaller (in absolute value) that the buckling load in compression (-3.17).

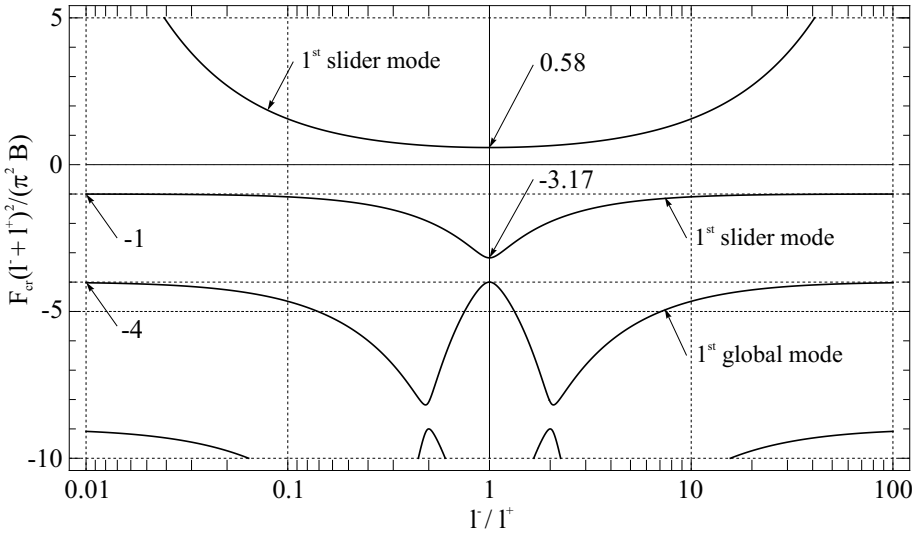

Fig. 4.5: Dimensionless critical loads F_{cr} as a function of the ratio between the lengths of the rods, l^+/l^-. The dimensionless axial forces for bifurcation in tension and those corresponding to the first two modes in compression are reported.

4.3.2 The elastica

The determination of the non-trivial configurations at large deflections of the mechanical system requires a careful use of Euler's elastica. It is instrumental to employ the reference systems shown in Fig. 4.6 and impose one kinematic compatibility condition and three equilibrium conditions. These are as follows.

- The kinematic compatibility condition can be directly obtained from Fig. 4.6 noting that the jump in displacement across the slider (measured orthogonally to the line of the elastica), Δ_s, can be related to the angle of rotation of the slider Φ_s, a condition that assuming the local reference systems shown in Fig. 4.6 becomes

$$\left[x_1^-(l^-) + x_1^+(l^+)\right] \tan \Phi_s + x_2^-(l^-) + x_2^+(l^+) + \Delta_s = 0, \qquad (4.19)$$

  where $x_1(s)$ and $x_2(s)$ are the coordinates of the elastica and the index $-$ $(+)$ denotes that the quantities are referred to the rod on

the left (on the right). Note that Φ_s is assumed positive when anticlockwise and Δ_s is not restricted in sign (negative in the case of Fig. 4.6).

- Since the slider can only transmit a moment and a force R orthogonal to it, equilibrium requires that (see the inset in Fig. 4.6)

$$R = \frac{F}{\cos \Phi_s}, \tag{4.20}$$

where F is the axial force providing the load to the rod, assumed positive (negative) when tensile (compressive), so that since $\Phi_s \in [-\pi/2, \pi/2]$, R is positive (negative) for tensile (compressive) load. Note that with the above definitions we have

$$\theta^+(0) = \theta^-(0) = 0, \quad \theta^+(l^+) = \theta^-(l^-) = -\Phi_s. \tag{4.21}$$

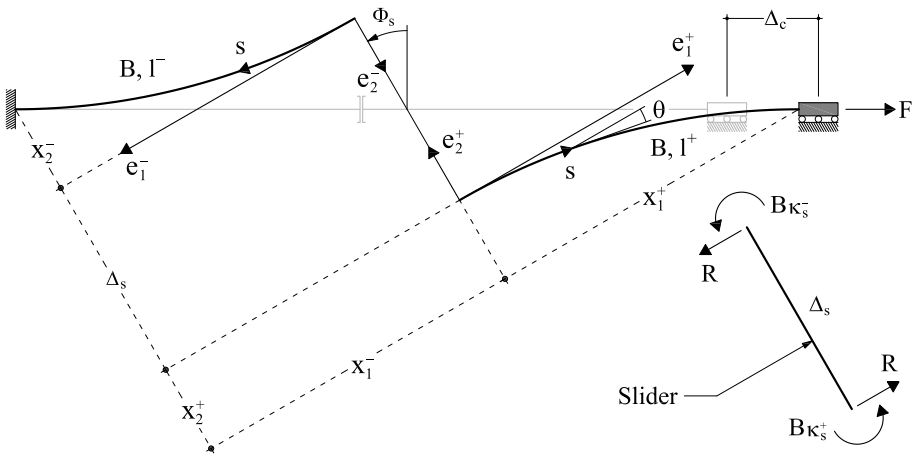

Fig. 4.6: Sketch of the problem of the elastica under tensile axial load F. Note the reference systems employed in the analysis and note that the moments on the slider have been reported positive and the curvature results to be negative.

- Equilibrium of the slider requires that

$$\kappa_s^- + \kappa_s^+ = \frac{R}{B}\,\Delta_s, \tag{4.22}$$

where B is the bending stiffness of the rod and $\kappa_s^{\pm}$ is the curvature on the left $(-)$ or on the right $(+)$ of the slider. Note that B is always positive, but R, $\kappa_s^{\pm}$ and Δ_s can take any sign.

- For both rods (left and right) rotational equilibrium of the element of rod singled out at curvilinear coordinate s requires

$$\frac{d^2\theta}{ds^2} - \frac{R}{B}\sin\theta = 0, \tag{4.23}$$

where θ is the rotation of the normal at each point of the elastica, assumed positive when anticlockwise, with added the superscript $-$ $(+)$ to denote the rod on the left (on the right).

Eq. (4.23) is usually (see for instance Love, 1927, his Eq. (8) at Sect. 262) written with a sign '+' replacing the sign '−' and R is assumed positive when compressive; the same equation describes the motion of a simple pendulum (see for instance Temme, 1996). The '+' sign originates from the fact that the elastica has been analyzed until now only for deformations originating from compressive loads. However, an equation with the '−' sign and with R/B replaced by the ratio between unit weight density and surface tension of a fluid –thus equal to Eq. (4.23)– determines *the shape of the capillary curve of a liquid* (Lamb, 1928), which therefore results to be identical to the deflection of a rod under tensile load.

In the following we derive equations holding along both rods '+' and '−', so that these indices will be dropped for simplicity. Multiplication of Eq. (4.23) by $d\theta/ds$ and integration from 0 to s yields

$$\left(\frac{d\theta}{ds}\right)^2 = -2\,\tilde{\alpha}^2\,\mathrm{sign}(R)\,\cos\theta + 2\,\tilde{\alpha}^2\left(\frac{2}{k^2} - 1\right), \tag{4.24}$$

where, using the Heaviside step function H, we have

$$\tilde{\alpha}^2 = \frac{|R|}{B} \quad \text{and} \quad k^2 = \left(\frac{\kappa_s^2}{4\,\tilde{\alpha}^2} + H(R)\right)^{-1}. \tag{4.25}$$

Eq. (4.24) can be re-written as

$$\left(\frac{d\theta}{ds}\right)^2 = \frac{4\,\tilde{\alpha}^2}{k^2}\left[1 - k^2\sin^2\left(\frac{\theta}{2} + \frac{\pi}{2}\,H(R)\right)\right], \tag{4.26}$$

so that the change of variable $u = s\tilde{\alpha}/k$ yields

$$\frac{d\,\theta}{d\,u} = \pm 2\sqrt{1 - k^2 \sin^2\left(\frac{\theta}{2} + \frac{\pi}{2}\,H(R)\right)}. \tag{4.27}$$

The analysis will be restricted for simplicity to the case '+' in the following. At $u = 0$ it is $\theta = 0$, so that Eq. (4.27) gives the solution

$$\theta = 2\,\mathrm{am}\left[u + KH(R), k\right] - \pi\,H(R) \tag{4.28}$$

and

$$\frac{d\,\theta}{d\,s} = \frac{2}{k}\,\tilde{\alpha}\,\mathrm{dn}\left[u + KH(R), k\right], \tag{4.29}$$

where am and dn are respectively the Jacobi elliptic functions amplitude and delta-amplitude and K is the complete elliptic integral of the first kind (Byrd and Friedman, 1971). Since in the local reference system we have $dx_1/ds = \cos\theta$ and $dx_2/ds = \sin\theta$, an integration gives the coordinates x_1 and x_2 of the elastica expressed in terms of u,

$$\begin{cases} x_1 = \dfrac{\left(2 - k^2\right) u - 2\,\mathrm{E}\left[\mathrm{am}\left[u, k\right], k\right] + 2k^2 \mathrm{sn}\left[u, k\right] \mathrm{cd}\left[u, k\right]}{k\,\tilde{\alpha}} \\ x_2 = \dfrac{2\sqrt{1 - k^2}\left(1 - \mathrm{dn}\left[u, k\right]\right)}{k\,\tilde{\alpha}\,\mathrm{dn}\left[u, k\right]} \end{cases} \tag{4.30}$$

for tensile axial loads ($R > 0$), while for compressive axial loads ($R < 0$)

$$\begin{cases} x_1 = \dfrac{\left(k^2 - 2\right) u + 2\,\mathrm{E}\left[\mathrm{am}\left[u, k\right], k\right]}{k\,\tilde{\alpha}} \\ x_2 = \dfrac{2\left(1 - \mathrm{dn}\left[u, k\right]\right)}{k\,\tilde{\alpha}} \end{cases} \tag{4.31}$$

in which the constants of integration are chosen so that x_1 and x_2 vanish at $s = 0$. In Eqs. (4.30)–(4.31) sn and cd are respectively the Jacobi elliptic functions sine-amplitude and cosine-amplitude/delta-amplitude and E is the incomplete elliptic integral of the second kind (Byrd and Friedman, 1971).

Eqs. (4.31) differ from Eqs. (16) reported by Love (1927, his Section 263) only in a translation of the coordinate x_2, while Eqs. (4.30), holding for tensile axial force, are new.

Finally, with reference to Fig. 4.6, we note that the horizontal displacement Δ_c of the right clamp can be written in the form

$$\Delta_c = \frac{x_1^-(l^-) + x_1^+(l^+)}{\cos\Phi_s} - \left(l^+ + l^-\right). \tag{4.32}$$

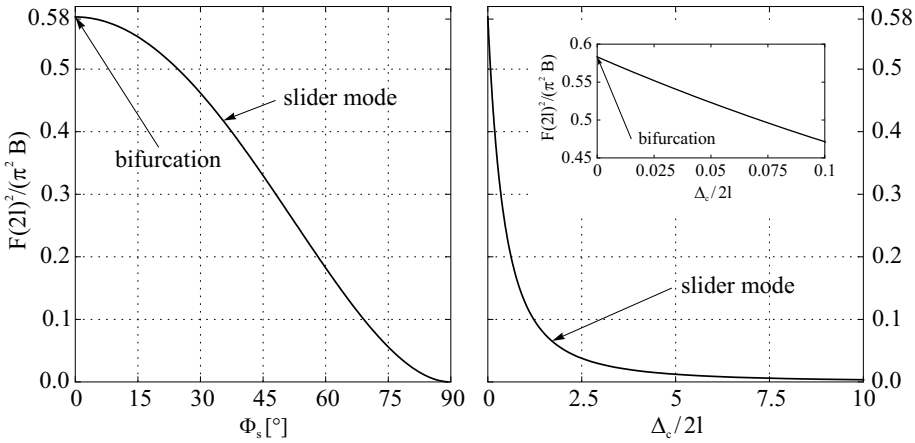

Fig. 4.7: Bifurcation of the structure sketched in Fig. 4.6 under tensile load. Dimensionless axial load F versus slider rotation (versus dimensionless end displacement) is shown on the left (on the right).

To find the axial load F as a function of the slider rotation Φ_s, or as a function of the end displacement Δ_c, we have now to proceed as follows:

- values for κ_s^- and κ_s^+ are fixed (as a function of the selected mode, for instance, $\kappa_s^- = \kappa_s^+$, to analyze the bifurcation mode in tension);
- k can be expressed using Eq. $(4.25)_2$ as a function of $\tilde{\alpha}$;
- the equations for the coordinates of the elastica, Eq. (4.30) for tensile load, or Eq. (4.31) for compressive load, and Eq. (4.28), evaluated at l^- and l^+, become functions of only $\tilde{\alpha}$;
- Eqs. (4.21) and (4.22) provide Φ_s and Δ_s, so that Eq. (4.19) becomes a nonlinear equation in the variable $\tilde{\alpha}$, which can be numerically solved (we have used the function FindRoot of Mathematica® 6.0);

- when $\tilde{\alpha}$ is known, R and F can be obtained from Eqs. $(4.25)_1$ and (4.20);
- finally, Φ_s and Δ_c are calculated using Eqs. $(4.21)_2$ and (4.32).

Results are shown in Fig. 4.7 for tensile loads and in Fig. 4.8 for compressive loads, in terms of dimensionless axial load $4Fl^2/(B\pi^2)$ versus slider rotation Φ_s (on the left) and dimensionless end displacement $\Delta_c/(2l)$ (on the right).

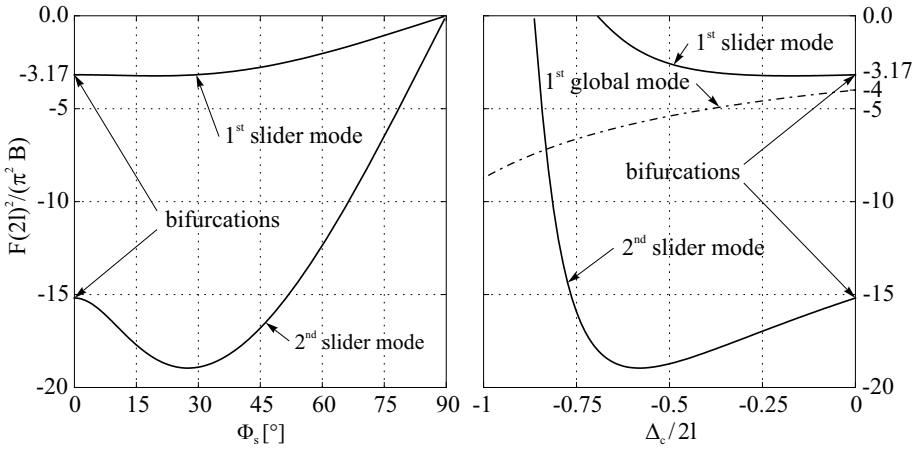

Fig. 4.8: Bifurcation of the structure sketched in Fig. 4.6 under compressive load. Dimensionless axial load F versus slider rotation (versus dimensionless end displacement) is shown on the left (on the right).

Note that, while there is only one bifurcation in tension, there are infinite bifurcations in compression, so that we have limited results to the initial three modes in compression. Two of these modes involve slider rotation (labeled 'slider mode'), while an intermediate mode (labeled 'global mode') does not.

The load/displacement curve shown in Fig. 4.7 on the left is plotted until extremely large displacements, namely, $\Delta_c = 20l$ (a detail at moderate displacement is reported in the inset). It displays a *descending, in other words softening and unstable, postcritical behaviour*, which contrasts with the usual postcritical of the elastica under various end conditions, in

which the load rises with displacement. In compression, the post-critical behaviour evidences another novel behaviour, so that the first and the second slider modes present an initial part where the load/displacement rises, followed by a softening behaviour. Finally, it is important to note that the curves load versus Φ_s in Figs. 4.7 and 4.8, both *for tension and compression intersect each other at null loading* at the extreme rotation $\Phi_s = 90°$, which means that two unloaded configurations (in addition to the initial configuration) exist. These peculiarities, never observed before in simple elastic structures, are all related to the presence of the slider.

Deformed elastic lines are reported in Fig. 4.9, both for tension and compression, the latter corresponding to the first three slider modes (the global mode is not reported since it corresponds to the first mode of a doubly-clamped rod).

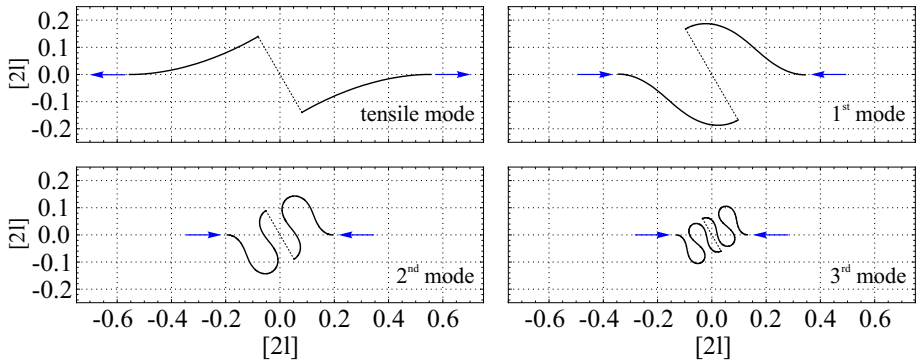

Fig. 4.9: Deflections (the scale of the axes is $2l$) of the structure shown in Fig. 4.6 (with rods of equal length) at a slider rotation of 30° in tension (upper part, on the left) and compression (first 3 slider modes are reported, whereas the global mode has not been reported).

4.4 Experimental

The structure sketched in Fig. 4.6 has been realized with two carbon steel AISI 1095 strips (250 mm × 25 mm × 1 mm; Young modulus 200 GPa) and the slider with two linear bearings (type Easy Rail SN22-80-500-610, purchased from Rollon®), commonly used in machine design applications,

see Fig. 4.10. The slider is certified by the producer to have a low friction

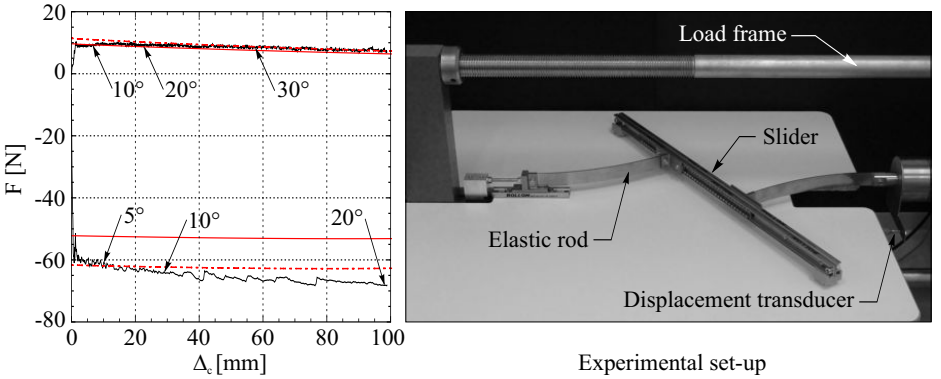

Fig. 4.10: Load versus end displacement for the model representing the structure sketched in Fig. 4.6 recorded during tensile (positive F) and compressive (negative F) tests. The red curves are the theoretical predictions (the dashed line is obtained keeping into account the effective values of the lengths of the rods, 10% smaller than the values measured from the clamps to the middle of the slider). The values '5°', '10°', '20°' and '30°' denote the inclination of the slider in degrees reached during the test. A photo of the experimental setup during the postcritical behaviour in tension is reported on the right.

coefficient, equal to 0.01. Tensile force on the structure has been provided by imposing displacement with a load frame ELE Tritest 50 (ELE International Ltd), the load measured with a load cell Gefran OC-K2D-C3 (Gefran Spa), and the displacement with a potentiometric transducer Gefran PY-2-F-100 (Gefran Spa). Data have been acquired with system NI CompactDAQ, interfaced with Labview 8.5.1 (National Instruments). Photos have been taken with a Nikon D200 digital camera, equipped with a AF-S micro Nikkor lens (105 mm 1:2.8G ED) and movies with a Sony Handycam HDR-XR550. Tensile and compressive tests have been run at a velocity of 2.5 mm/s.

Photos taken at different slider rotations (and thus load levels) are shown in Fig. 4.11 for tension ($\Phi_s = 0°$, 10°, 20°, 30°) and in Fig. 4.12 for compression ($\Phi_s = 0°$, 5°, 10°, 20°). A comparison between theoretical predictions and experiments is reported in the lower parts of the figures where photos are superimposed to the line of the elastica, shown

in red and plotted using Eq. (4.30) for tensile load and Eq. (4.31) for compression. These experiments show clearly the existence of the bi-

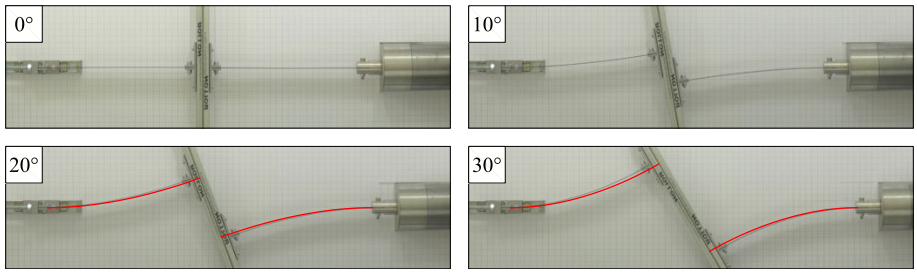

Fig. 4.11: Photos of the model representing the structure sketched in Fig. 4.6 and loaded in tension at different values of slider rotation $\Phi_s = 0°$, 10°, (upper part) 20°, 30° (lower part). The elastica calculated with Eq. (4.30) is superimposed on the photos at 20°, 30° in the lower part. The side of the grid marked on the paper is 10 mm.

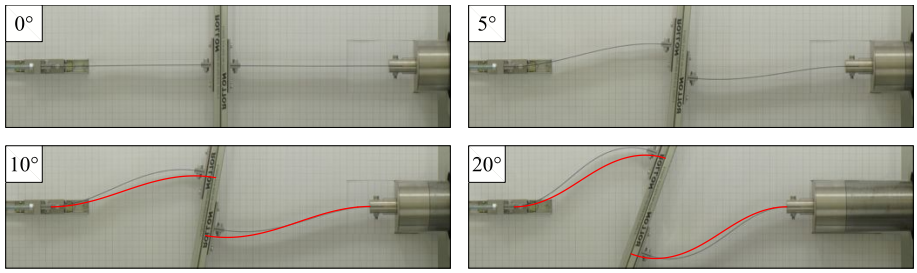

Fig. 4.12: Photos of the model representing the structure sketched in Fig. 4.6 and loaded in compression at different values of slider rotation $\Phi_s = 0°$, 5°, (upper part) 10°, 20° (lower part). The elastica calculated with Eq. (4.30) is superimposed on the photos at 10°, 20° in the lower part. The side of the grid marked on the paper is 10 mm.

furcation in tension and provide an excellent comparison with theoretical results obtained through integration of the elastica both in tension and in compression. A further quantitative comparison between theoretical results and experiments is provided in Fig. 4.10, where the axial load in the structure (positive for tension and negative for compression) is plotted versus the end displacement Δ_c. The experimental result is compared to theoretical results (marked red) expressed by Eq. (4.32), used in the way

detailed at the end of Section 4.3.2.

The theoretical result marked in red with continuous curve has been calculated assuming an initial length of the rods (25 cm) measured from the end of the clamps to the middle of the slider. However, the slider and the junctions to the metal strips are 58 mm thick, so that the system is stiffer in reality. Therefore, we have plotted dashed the theoretical results obtained employing an 'effective' initial length of the rods reduced of 10% (so that the effective length of the system has been taken equal to 45 cm). The experimental curve evidences oscillations of ± 1 N for tensile loads and ± 5 N for compressive loads. These oscillations are due to friction within the slider, so that it is obvious that the oscillations are higher in compression than in tension, since in the former case the load is higher. Except for these oscillations, the friction (which is very low) has been found not to influence the tests.

The fact that experimentally the bifurcations initiate before the theoretical values are attained represents the well-known effect of imperfections, so that we may conclude that the agreement between theory and experiments is excellent.

To provide experimental evidence to the fact that the elastica in tension corresponds to the shape of the free surface of a liquid in a capillary channel, we note that a meniscus in a capillary channel satisfies (by symmetry) a null-rotation condition at the centre of the channel, so that it corresponds to a clamped edge of a rod. If the tangent to the meniscus at the contact with the channel wall is taken to correspond to the rotation of the non-clamped edge of the rod and the width of the channel is calculated employing the elastica, the elastic deflection of the rod scales with the free surface of the liquid. Therefore, we have performed an experiment in which we have taken a photo (with a Nikon SMZ800 stereo-zoom microscope equipped with Nikon Plan Apo 0.5x objective and a Nikon DD-FI1 high definition color camera head) of a water meniscus in a polycarbonate channel. We have proceeded as follows. First, we have observed that the contact angle between a water surface in air and polycarbonate (at a temperature of 20°C) is 70°. Second, we have taken a photo of the meniscus formed in a polycarbonate 'V-shaped' channel with walls inclined at 10° with the vertical, so that the angle between the horizontal direction and the free surface results to be 30° and the distance between the walls results

6 mm. This photo has been compared with a photo taken (with a Nikon D200 digital camera, and shown in Fig. 4.11 on the right) during buckling in tension when the elastic rods form the same angle of 30°. The result is shown in Fig. 4.1, together with the theoretical solution shown red.

4.5 Conclusions

We have theoretically proven and fully experimentally confirmed that elastic structures can be designed and practically realized in which bifurcation can occur with tensile dead loading. In these structures no parts subject to compression are present. The finding is directly linked to the presence of a junction allowing only for relative sliding between two parts of the mechanical system. Our findings open completely new and unexpected perspectives, related for instance to the control of the propagation of mechanical waves and to the understanding of certain failure modes in material elements.

CHAPTER
FIVE

THE EXPERIMENTAL EVIDENCE OF FLUTTER INSTABILITY INDUCED BY DRY FRICTION

Flutter and divergence instabilities have been advocated to be possible in elastic structures with Coulomb friction, but no direct experimental evidence has ever been provided. Moreover, the same types of instability can be induced by tangential follower forces, but these are commonly thought to be of extremely difficult, if not impossible, practical realization. Therefore, a clear experimental basis for flutter and divergence induced by friction or follower-loading is still lacking. This is provided for the first time in the present article, showing how a follower force of tangential type can be realized via Coulomb friction and how this, in full agreement with the theory, can induce a blowing-up vibrational motion of increasing amplitude (flutter) or an exponentially growing motion (divergence). In addition, our results show the limits of a treatment based on the linearized equations, so that nonlinearities yield the initial blowing-up vibration of flutter to reach eventually a steady-state. The presented results give full evidence to potential problems in the design of mechanical systems subject to friction, open a new perspective in the realization of follower loading systems and of innovative structures exhibiting 'unusual' dynamical behaviours.

5.1 Introduction

Coulomb friction at the contact between two elastic bodies is an example of a live load (since it acts in a direction opposite to the relative

velocity during sliding of the bodies) and is known to be connected to different forms of instabilities. Two of these, the so-called 'flutter' and 'divergence' (the former associated to blowing-up oscillations and the latter to an exponentially growing motion), are dynamical instabilities that have been *theoretically* shown to be possible in elastic structural systems with Coulomb friction (Martins *et al.*, 1999; Simões and Martins, 1998; Nguyen, 2003) and even in plastic continua characterized by frictional behaviour (Rice, 1977; Loret, 1992; Bigoni, 1995; Bigoni and Loret, 1999; Loret *et al.*, 2000; Piccolroaz *et al.*, 2006). However, *no clear experimental evidence of flutter and divergence instabilities related to dry friction has ever been presented* [1], so that flutter induced by friction has always been thought to be a puzzling phenomenon, since it is rather 'unexpected' that a merely dissipative factor such as friction, can induce blowing-up dynamical motions in a mechanical system that would be stable in the absence of it. Moreover, for friction-related flutter in structures and continua, the role played by the nonlinearities, usually neglected in the stability analyses, is simply not known from the experimental point of view, so that these could even have a stabilizing effect, see the discussion by Bigoni and Petryk (2002).

The primary purpose of this work is to provide a definitive and indisputable experimental evidence for flutter and divergence instability in elastic systems with dry Coulomb friction. The key for this achievement is the link with a special elastic structure exhibiting flutter and divergence: the so-called 'Ziegler column' (Ziegler, 1953; 1977). This is a two-degree-of-freedom structure made up of two rigid bars, jointed each other and fixed at one end through two elastic rotational springs, while a tangential follower load, in other words a load remaining collinear with the terminal rod, is applied at one end (Fig. 5.1). Since the follower load is nonconser-

[1] Friction-related dynamical instabilities are thought to be responsible of brake squeal and of the 'song' of a fingertip moved upon the rim of a glass of water, but these phenomena involve stick and slip, a phenomenon modelled as a drop of friction coefficient with velocity (Rice and Ruina, 1983). It is therefore not clear if the instabilities would occur in the absence of this drop and it is not possible to definitely conclude about the real nature of these, which appear to be only weakly related to the flutter of the structures subject to follower load, so that there are many different theories to describe brake squeal involving or not follower forces (see the reviews by Flint and Hultén, 2002; Kröger *et al.*, 2008).

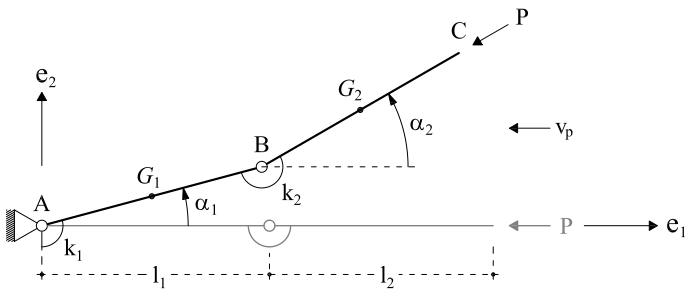

Fig. 5.1: The Ziegler column, a two-degree-of-freedom system subject to follower load (the force **P** remains always applied to C and directed parallel to the rod BC), exhibiting flutter and divergence instability. The two rods, of linear mass density ρ, are rigid and connected through two rotational springs of stiffness k_1 and k_2. Note that there is no bifurcation for this system.

vative, the structure becomes dynamically unstable at a certain load level (although non-trivial equilibrium configurations do not exist), so that it evidences flutter (a blowing-up oscillating motion) and, at higher load, divergence instability (an exponentially growing motion) [2].

As a result of a complex fluid-structure interaction, follower loads and related instabilities may occur in aeroelasticity, but these do not directly involve the tangential follower force postulated in the Ziegler column, which is thought to be of such difficult practical realization[3] that a clear experimental basis for flutter and divergence instability as induced by tangential follower load is still lacking. These difficulties led Professor W.T.

[2]The history of the discovery of this instability involves, among others, Nikolai (1928), Pflüger (1950; 1955), Beck (1952), Ziegler (1953; 1956; 1977), Bolotin (1963), Herrmann and Jong (1965), Como (1966) and is explained in detail by Elishakoff (2005), who also provides an account of the frustrating attempts of giving experimental evidence to the theory.

[3]Follower tangential forces have been realized until now through a fluid flowing from a nozzle, or through a solid motor rocket fixed at the end of the structure (Herrmann *et al.*, 1966; Sugiyama *et al.*, 1995; 2000), two devices introducing complications in the modelling. In fact, the complex fluid/structure interaction of a fluid flowing from a nozzle is only as a first approximation reduced to a follower thrust, while in the other experimental set-up complications arise from the non-negligible mass and dimensions of the solid motor rocket and from the short duration of the thrust provided by it, which prevents long-term analyses of the motion.

Koiter (1996) to propose the 'elimination of the abstraction of follower forces as external loads from the physical and engineering literature on elastic stability' and to conclude with the warning: 'beware of unrealistic follower forces'.

In the present article we show that it is possible to exploit dry friction to generate follower loads of the type postulated by Ziegler (1953; 1977), so that flutter and divergence instabilities in structures and in mechanical systems with dry friction are shown to be strictly connected phenomena. In particular, we will prove the following results.

- First, we definitely disclaim Koiter's statement and the current opinion that follower forces are unrealistic, showing that *a follower load can be easily realized exploiting dry friction and that flutter and divergence instabilities can be observed with a simple experimental setting, so simple that can even be reduced to a toy for kids.*

- Second, *we prove in a direct and indisputable way that flutter and divergence instabilities can be induced by dry friction.*

- Third, *we investigate experimentally and theoretically the role of nonlinearities on the development of the instability, showing that in the case of flutter these induce the attainment of a steady-state motion.*

The above mentioned results have been obtained by inventing, designing and testing a two-degree-of-freedom elastic structure with a frictional (obeying the Coulomb rule) element.

A brief explanation of our idea and results can be given as follows. Our two-degree-of-freedom system is a simple variant to the Ziegler column (Fig. 5.1), where the follower load is induced by a frictional force acting on a wheel mounted at the end of the structure and kept sliding with friction against a plane. Note the crucial role played by the wheel, which transmits the frictional force coaxial to its axis (see the sketch in Fig. 5.3). The behaviour of the structure is shown in Fig. 5.2, where photos taken at different time instants have been superimposed. On the left of the figure we may see an example of flutter instability, while on the right an example of divergence. The numbers provide the order in which the photos have

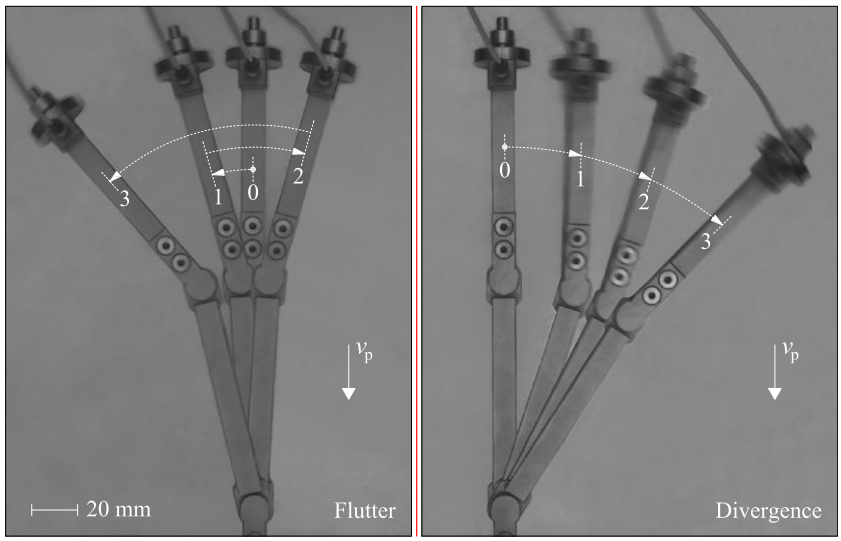

Fig. 5.2: A superposition of photos, adapted from Figs. 5.10 and 5.14 on the left, taken at different instants of time [(0, 0.48, 0.72, 1.08) s for flutter and (0, 0.20, 0.28, 0.36) s for divergence] of the two-degree-of-freedom structure (Fig. 5.8b) exhibiting flutter (left) and divergence (right) instability. v_p is the velocity of a plate sliding against the wheel, taken equal to 75 mm/s for flutter and 50 mm/s for divergence.

been taken, so that we can clearly detect the oscillatory blow-up of flutter, to be contrasted with the progressive growth of divergence[4].

The Chapter is organized as follows. A variant of the Ziegler column is presented in Section 5.2, in which the mass is distributed along the two rigid beams forming the system and the follower load is provided by a frictional device obeying Coulomb friction. The basic ideas for the design of the structure and the complication involved with the friction constraint are detailed. The practical realization of the structure is described in Section 5.3, where experimental results are provided and commented. A final discussion is presented in Section 5.4.

[4]A movie with experiments can be downloaded at http://ssmg.ing.unitn.it/. Note in the movie the acoustic emission during the test, also evidencing the instability.

5.2 The two-degree-of-freedom system

It is well-known that flutter instability may be induced in a structure by non-conservative loads and the typical example is the so-called 'Ziegler column', the two-degree-of-freedom system with heavy rigid rods (mass per unit length ρ) shown in Fig. 5.1, where two rotational springs of stiffness k_1 and k_2 provide the elasticity. The generic configuration of the structure remains determined by the two Lagrangean parameters α_1 and α_2. The applied load $\mathbf{P}$, assumed positive when compressive, maintains the direction parallel to the rod BC. The analysis of a system similar to this (with concentrated masses instead than diffused) can be found in Herrmann (1971), Ziegler (1977) and, in a simplified version, in Nguyen (1995), while the analogous problem of a clamped column subjected to a load tangential to its axis at the free end has been solved by Beck (1952) and Pflüger (1955).

The follower force $\mathbf{P}$ in the structure shown in Fig. 5.1 has been previously realized through a fluid flowing from a nozzle (Herrmann *et al.*, 1966) or through an end rocket (Sugiyama *et al.*, 1995; 2000) fixed at the end of the structure.

Our idea is

> *to provide the follower force through a wheel of negligible mass mounted at the top of the structure and constrained to slide against a frictional plane, see Fig. 5.3.*

In fact, a perfect (massless and fully free of rotating) wheel sliding with pure Coulomb friction (but without rolling friction) on a rigid plane, which is ideally touched at a point, can only transmit an axial force and we will show that these conditions can be successfully approximated in real experiments, since the deviations from the ideal model that necessarily arise in experiments are not sufficient to hide the instabilities.

Following the above-mentioned idea, we analyze the structure shown in Fig. 5.1 under the hypotheses that: (i.) the wheel is massless, free of rotating, and touches the horizontal plane at a point, (ii.) the hinges (unloaded in the straight configuration) are viscoelastic, (iii.) the follower force is transmitted through Coulomb friction of coefficient μ_d by a plane moving at the speed $-v_p\,\mathbf{e}_1$, and that (iv.) there is no rolling friction, so that the

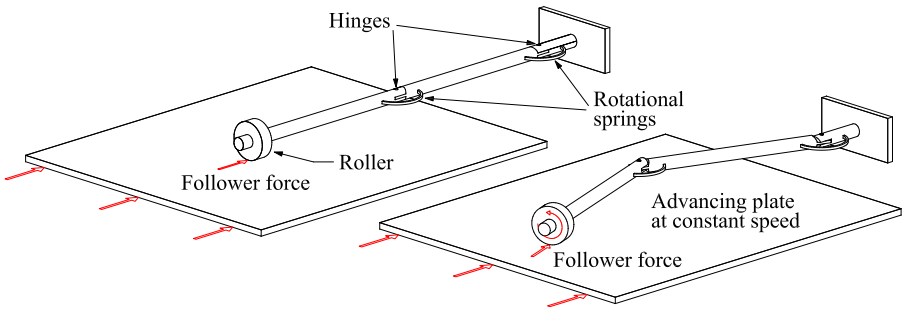

Fig. 5.3: The way to produce a force coaxial to a rod from friction; a freely rotating wheel of negligible mass is mounted at the top of the rod.

analysis merely differs from results in the above-mentioned literature in the inclusion of the friction condition at the end of the structure.

The above-mentioned assumptions (i.)–(iv.) are very close to our experimental setup and have been verified both experimentally (changing the wheel's mass and profile, the friction coefficient, the geometry of the structure and the stiffness and viscosity of the springs, see Section 5.3) and theoretically (we have performed more sophisticated computations by introducing the mass and rotational inertia of the wheel, the rolling friction and a possible deviation of the frictional load from collinearity), so that we may point out that, though more complex models might yield a better quantitative comparison with experiments, they cannot change the overall qualitative picture, which will be shown to be very well captured with simple assumptions.

A simple static analysis of the structure shown in Fig. 5.1 is sufficient to conclude that only the trivial (straight) configuration satisfies equilibrium (in fact equilibrium of the rod BC is only possible if $\alpha_1 = \alpha_2$, while equilibrium of the complex ABC requires $\alpha_1 = 0$), so that quasi-static bifurcations are excluded.

Let us obtain now the equations of motion for the system. To this purpose, we start from the position vectors of the point **C** and of the mass

center of the rods $\mathbf{G}_1$ and $\mathbf{G}_2$

$$\begin{aligned}
\mathbf{C}-\mathbf{A} &= \{l_1\cos\alpha_1 + l_2\cos\alpha_2\}\mathbf{e}_1 + \{l_1\sin\alpha_1 + l_2\sin\alpha_2\}\mathbf{e}_2\\
\mathbf{G}_1-\mathbf{A} &= \{l_1\cos\alpha_1/2\}\mathbf{e}_1 + \{l_1\sin\alpha_1/2\}\mathbf{e}_2\\
\mathbf{G}_2-\mathbf{A} &= \{l_1\cos\alpha_1 + l_2\cos\alpha_2/2\}\mathbf{e}_1 + \{l_1\sin\alpha_1 + l_2\sin\alpha_2/2\}\mathbf{e}_2
\end{aligned} \tag{5.1}$$

where $\mathbf{e}_1$ and $\mathbf{e}_2$ are the two unit vectors singling out the horizontal and vertical direction respectively, so that the follower force $\mathbf{P}$, of modulus P, can be expressed as

$$\mathbf{P} = -\{P\cos\alpha_2\}\mathbf{e}_1 - \{P\sin\alpha_2\}\mathbf{e}_2, \tag{5.2}$$

where, denoting with a superimposed dot the derivative with respect to time, P is given by the Coulomb friction law with stiction

$$P = R\,\mu(\dot{C}_p^r), \quad \mu(\dot{C}_p^r) = \begin{cases} \mu_d\,\mathrm{sign}(\dot{C}_p^r), & \text{if } \dot{C}_p^r = \dot{\mathbf{C}}_p\cdot\mathbf{e}_r \neq 0,\\ [-\mu_s,\ \mu_s], & \text{if } \dot{C}_p^r = \dot{\mathbf{C}}_p\cdot\mathbf{e}_r = 0, \end{cases} \tag{5.3}$$

where R is the vertical reaction applied at the wheel (orthogonal to the moving plane), μ_s and μ_d are the static and dynamic friction coefficients (their difference gives the 'stiction effect', which vanishes taking $\mu_s = \mu_d$) and $\dot{C}_p^r$ is the radial component ($\mathbf{e}_r = \{\cos\alpha_2\}\mathbf{e}_1 + \{\sin\alpha_2\}\mathbf{e}_2$) of the velocity of the wheel relative to the plate, so that we can write

$$\dot{\mathbf{C}}_p = \dot{\mathbf{C}} + v_p\,\mathbf{e}_1, \qquad \dot{\mathbf{C}}_p\cdot\mathbf{e}_r = v_p\,\cos\alpha_2 - l_1\sin(\alpha_1-\alpha_2)\dot{\alpha}_1. \tag{5.4}$$

For the practical realization of the experiment, the vertical reaction R will be provided by using the structure itself as a lever to which a dead load W is applied, as sketched in Fig. 5.4, so that

$$R = \frac{l_s}{l_f + l_1\cos\alpha_1 + l_2\cos\alpha_2}\,W, \tag{5.5}$$

where l_s is the length of one arm of the lever, while the denominator is the variable length of the other, see Fig. 5.4.

It is assumed that the hinges are viscoelastic of the Voigt type with constants β_1, β_2, k_1, and k_2, so that the moments applied to the rods are

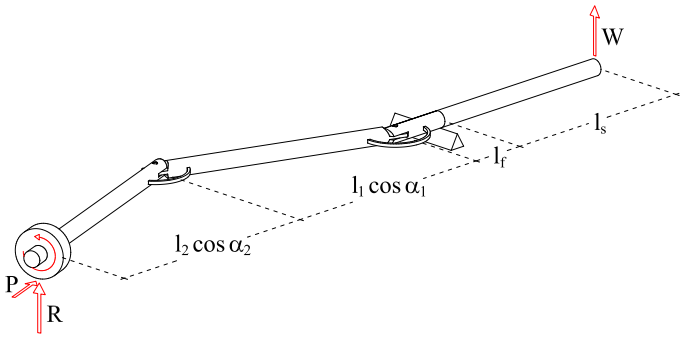

Fig. 5.4: The structure shown in Fig. 5.3 is used as a lever to provide the vertical reaction R from the vertical dead load W, so that the force from friction results $P = \mu_d R$.

$k_1\alpha_1 + \beta_1\dot{\alpha}_1$ and $k_2(\alpha_2 - \alpha_1) + \beta_2(\dot{\alpha}_2 - \dot{\alpha}_1)$ and the principle of virtual works, denoting with '$\cdot$' the scalar product, writes as (see Appendix A for details)

$$\begin{aligned}&\mathbf{P}\cdot\delta\mathbf{C} - (k_1\alpha_1 + \beta_1\dot{\alpha}_1)\delta\alpha_1 - [k_2(\alpha_2 - \alpha_1) + \beta_2(\dot{\alpha}_2 - \dot{\alpha}_1)](\delta\alpha_2 + \\ &-\delta\alpha_1) - \rho[l_1\ddot{\mathbf{G}}_1\cdot\delta\mathbf{G}_1 + l_2\ddot{\mathbf{G}}_2\cdot\delta\mathbf{G}_2 + (l_1^3\ddot{\alpha}_1\delta\alpha_1 + l_2^3\ddot{\alpha}_2\delta\alpha_2)/12] = 0,\end{aligned} \tag{5.6}$$

holding for every virtual rotation $\delta\alpha_1$ and $\delta\alpha_2$. Imposing now the condition (5.6) and invoking the arbitrariness of $\delta\alpha_1$ and $\delta\alpha_2$ we arrive at the two nonlinear differential equations

$$\begin{cases} \rho\,\dfrac{l_1^2}{3}\,(l_1 + 3l_2)\,\ddot{\alpha}_1 + \rho\,\dfrac{l_1 l_2^2}{2}[\cos(\alpha_1 - \alpha_2)\ddot{\alpha}_2 + \sin(\alpha_1 - \alpha_2)\dot{\alpha}_2^2] + \\ + (\beta_1 + \beta_2)\dot{\alpha}_1 - \beta_2\,\dot{\alpha}_2 + (k_1 + k_2)\alpha_1 - k_2\,\alpha_2 + \\ - l_1 P(\dot{C}_p^r)\sin(\alpha_1 - \alpha_2) = 0, \\ \rho\,\dfrac{l_1 l_2^2}{2}[\cos(\alpha_1 - \alpha_2)\ddot{\alpha}_1 - \sin(\alpha_1 - \alpha_2)\dot{\alpha}_1^2] + \rho\,\dfrac{l_2^3}{3}\,\ddot{\alpha}_2 + \\ - \beta_2(\dot{\alpha}_1 - \dot{\alpha}_2) - k_2(\alpha_1 - \alpha_2) = 0, \end{cases} \tag{5.7}$$

governing the dynamics of the system. A numerical solution of the nonlinear differential system (5.7) faces the well-known numerical difficulty that

the friction law (5.3) is a multivalued, discontinuous relation (Threlfall, 1977; Oden and Martins, 1985; Martins *et al.*, 1990). This difficulty can be overcome using a viscous smooth approximation of the law, including or not the difference between static and dynamical friction, which in the continuous approximation becomes the so-called 'Stribeck effect' (Stribeck, 1902). In the following we have numerically solved the system (5.7) using different approximations to the law (5.3), including and neglecting the Stribeck effect, and we have found that results *for our structure* do not differ much, so that the root of the unstable behaviour is *not* linked to a drop in the friction coefficient. Therefore, we will refer to the simple approximation to the relation (5.3) employed by Oden and Martins (1985) and Martins *et al.* (1990)

$$\mu(\dot{C}_p^r) = \mu_d \begin{cases} \operatorname{sign}(\dot{C}_p^r), & \text{if } \dot{C}_p^r \notin [-\varepsilon, \varepsilon], \\ \left(2 - \dfrac{|\dot{C}_p^r|}{\varepsilon}\right) \dfrac{\dot{C}_p^r}{\varepsilon}, & \text{if } \dot{C}_p^r \in [-\varepsilon, \varepsilon], \end{cases} \tag{5.8}$$

where ε is a small parameter.

A purely elastic analysis ($\beta_1 = \beta_2 = 0$) of the structure (a linear viscoelastic analysis is deferred to Appendix A), valid for configurations in a small neighborhood of the trivial one ($\alpha_1 = \alpha_2 = 0$) can be performed with the incrementally nonlinear differential system obtained from Eqs. (5.7) through a Taylor series expansion in the form

$$\begin{cases} \rho \dfrac{l_1^2}{3} (l_1 + 3l_2)\, \ddot{\alpha}_1 + \rho \dfrac{l_1 l_2^2}{2} \ddot{\alpha}_2 + (k_1 + k_2)\alpha_1 - k_2\, \alpha_2 + \\ - l_1 P(\dot{C}_p^r)(\alpha_1 - \alpha_2) = 0, \\ \rho \dfrac{l_1 l_2^2}{2} \ddot{\alpha}_1 + \rho \dfrac{l_2^3}{3} \ddot{\alpha}_2 - k_2(\alpha_1 - \alpha_2) = 0, \end{cases} \tag{5.9}$$

where $P(\dot{C}_p^r)$ remains the incrementally nonlinear function (5.3). Note that the Eqs. (5.9) are similar (keeping aside for the moment the complication related to the difference between μ_s and μ_d) to the piecewise incremental nonlinearity of a rigid perfectly-plastic body. The complication connected to the incremental nonlinearity disappears if the plate/wheel sliding condition $\dot{C}_p^r > 0$ is always verified, a situation which certainly

holds *at the instant* of flutter (when $\alpha_1 = \alpha_2 = 0$) and *even for a finite interval of time* from this instant, , for v_p sufficiently high to satisfy $v_p > l_1 \sin(\alpha_1 - \alpha_2)\dot{\alpha}_1 / \cos\alpha_2$. In this case, we can operate with the fully linearized version of Eqs. (5.7)

$$\begin{cases} \rho \dfrac{l_1^2}{3}(l_1 + 3l_2)\,\ddot{\alpha}_1 + \rho \dfrac{l_1 l_2^2}{2}\ddot{\alpha}_2 + (k_1 + k_2)\alpha_1 - k_2\,\alpha_2 + \\ - l_1 P(\alpha_1 - \alpha_2) = 0, \\ \\ \rho \dfrac{l_1 l_2^2}{2}\ddot{\alpha}_1 + \rho \dfrac{l_2^3}{3}\ddot{\alpha}_2 - k_2(\alpha_1 - \alpha_2) = 0, \end{cases} \tag{5.10}$$

where P is now independent of $\dot{C}_p^{rr}$ and given by

$$P = \mu_d\, R = \mu_d \frac{l_s}{l_f + l_1 + l_2}\, W. \tag{5.11}$$

In the flutter analyses usually performed in nonassociative elastoplasticity (see for instance Bigoni, 1995), 'plastic loading' is always assumed, in other words, a fully linear system such as that described by Eqs. (5.10) and (5.11) is considered. We will soon be in a position to test this assumption on our structure both theoretically and experimentally; for the moment, continuing with the linearization Eq. (5.11), we look for time-harmonic vibrations so that we can conclude that (see Appendix A for details):

- *flutter instability* occurs when $W_f < W < W_d$, with

$$W_{\substack{f \\ d}} = \frac{k_2(l_f + l_1 + l_2)}{\mu_d l_s l_1} \cdot \frac{k + (1+\lambda)^3 \mp \lambda\sqrt{k(3+4\lambda)}}{1 + 3\lambda/2}, \tag{5.12}$$

  where

$$\lambda = \frac{l_1}{l_2}, \quad k = \frac{k_1}{k_2}, \tag{5.13}$$

- and *divergence instability* occurs when $W > W_d$.

The linearized analysis yields the known conclusion (which cannot be reached through a quasi-static analysis) that, *while divergence instability corresponds to a motion growing exponentially in time, flutter instability corresponds to a self-excited oscillation blowing up in time.* This statement

is confirmed in Fig. 5.5, where results are reported as solution of the linear differential system (5.10) with the initial conditions $\alpha_1 = \alpha_2 = 0.5°$ ($\alpha_1 = \alpha_2 = -0.5°$ for divergence) and $\dot{\alpha}_1 = \dot{\alpha}_2 = 0$ and with the geometric and stiffness setting that will be employed for experiments (see Tab. 5.2). A 0.52 (0.2) seconds sequence of configurations at different instants of time is reported in the figure, where each configuration is drawn at fixed intervals of time (0.04 s). The oscillatory blow-up (exponential growth) of the solution is clearly visible in the case of flutter (divergence).

The linearized elastic analysis has the mentioned limitations that: (i.) slip at the wheel/plate contact is assumed, $\dot{C}_p^r > 0$, (ii.) geometrical nonlinearities are neglected, and (iii.) viscous behaviour of the hinges is set to zero. So that the the question arises whether the blowing-up motion connected to flutter (or to divergence) really develops or is strongly altered, maybe even 'damped-down', by nonlinearities. We can provide various answers to these questions, which are now discussed in detail.

- Assumption (i.), namely, $\dot{C}_p^r > 0$. For sufficiently high velocities of the plate, v_p, this condition is verified not only at the instant of flutter, but also for a finite interval of time, say, until $l_1(\alpha_1 - \alpha_2)\dot{\alpha}_1$ remains sufficiently small when compared to v_p. It is therefore expected that *the linearized analysis based on Eqs. (5.10) correctly predicts the onset and the early development of a dynamical instability, without involving any stick-slip phenomena*. This statement is verified in the example reported in Fig. 5.5, where we have observed that the wheel/plate slip condition is satisfied for all reported configurations until the instant of time 0.40 s for flutter (0.16 s for divergence). Therefore, the problem to be addressed is not if flutter and divergences are 'true' instabilities, but how these instabilities develop when displacements become sufficiently large to violate the wheel/plate slip condition (and to involve the other nonlinearities). This problem is solved in the following both with a numerical and an experimental approach.

- Assumptions (ii.). The geometrical nonlinearities play a role only when the displacement of the structure becomes large. These effects need to be included for a correct modelling of the experiments, since we have observed large (and very fast) movements to occur, so large

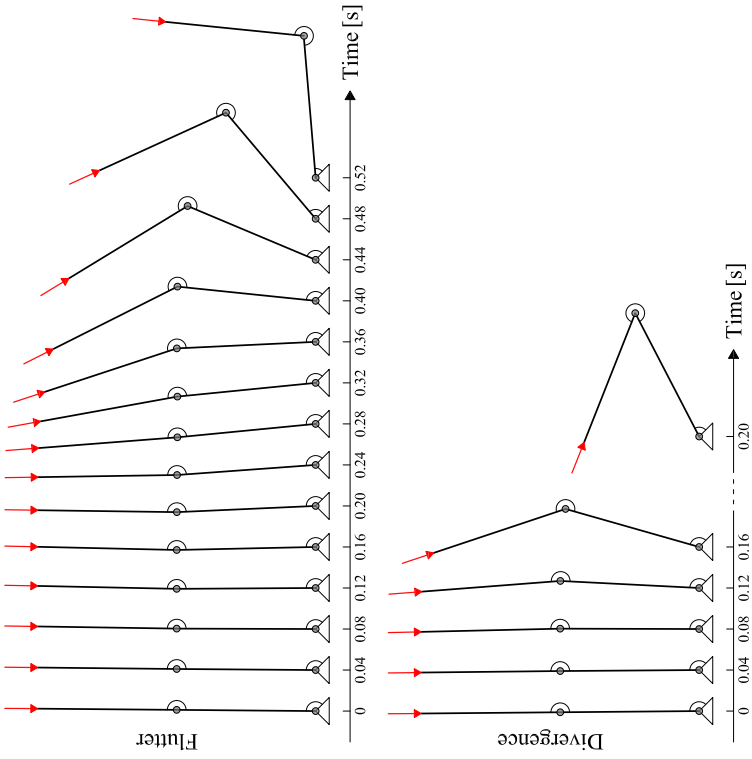

Fig. 5.5: A sequence (0.52 s for flutter and to 0.2 s for divergence) of deformed shapes at consecutive times intervals of 0.04 seconds of the structure sketched in Fig. 5.1 and exhibiting flutter (upper part) and divergence (lower part) instability. Results have been obtained through a linearized analysis [Eqs. (5.10)] with initial conditions $\alpha_1 = \alpha_2 = 0.5^\circ$ ($\alpha_1 = \alpha_2 = -0.5^\circ$ for divergence) and $\dot{\alpha}_1 = \dot{\alpha}_2 = 0$, at the flutter load $(W_f + W_d)/2$ (upper part) and at the divergence load $1.75\,W_d$ (lower part), Eq. (5.12). The values employed for the analysis are reported in Tab. 5.2.

in the case of divergence instability, that we have had to limit the maximum stroke of the structure with a constraint, to avoid failure of the equipment.

- Assumptions (iii.). We have experimentally detected (in a way independent of the instability tests, that will be explained later) a viscous behaviour of the hinges, the consideration of which in the modelling has yield a better comparison to experiments. In any case the instability is not associated to the viscosity, so that we have observed it to occur under various conditions of lubrications at the hinges.

To check the limits of the above assumptions and to be able to model our experiments, we have provided fully nonlinear analyses of the differential system (5.7), employing the regularization (5.8) with $\varepsilon = 10^{-5}$ m/s. One of these analyses (performed numerically using the function 'NDSolve' of Mathematica 6.0) is shown in Fig. 5.6, where configurations at different instants of time have been reported as in Fig. 5.5, but introducing now also the damping coefficients β_1 and β_2, with the values that best fit our experiments (that will be introduced in the next Section, see Tabs. 5.1 and 5.2). We highlight that for all the deformed configurations reported in Fig. 5.6 for flutter, the regularization law (5.8) is not 'activated', so that $\dot{C}_p^r > \varepsilon$, while in the case of the divergence, the regularization is activated starting from the configuration at the instant of time 0.20 s. This means that in the conditions relevant for our experiments, the early development of flutter and divergence fully occurs *without* involving transitions from the dynamic to static friction coefficients, with the possibility of stick-slip instabilities.

We can conclude from Fig. 5.6 that an initial oscillation of increasing amplitude is observed, as would be predicted by a linearized analysis, but that *the oscillation becomes steady at large deformations* (see http://ssmg.ing.unitn.it), so large which could yield the failure of a real structure (in fact we have broken our first two prototypes of the structure during early tests, so that eventually we have designed the third prototype to resist large displacements). A plot of the movement of the tip of the structure recorded on the moving plate, as calculated from solution of the nonlinear Eqs. (5.7) is reported in Fig. 5.7, contrasted with an experimental result, namely, a scratch left on the plate by the wheel during a test.

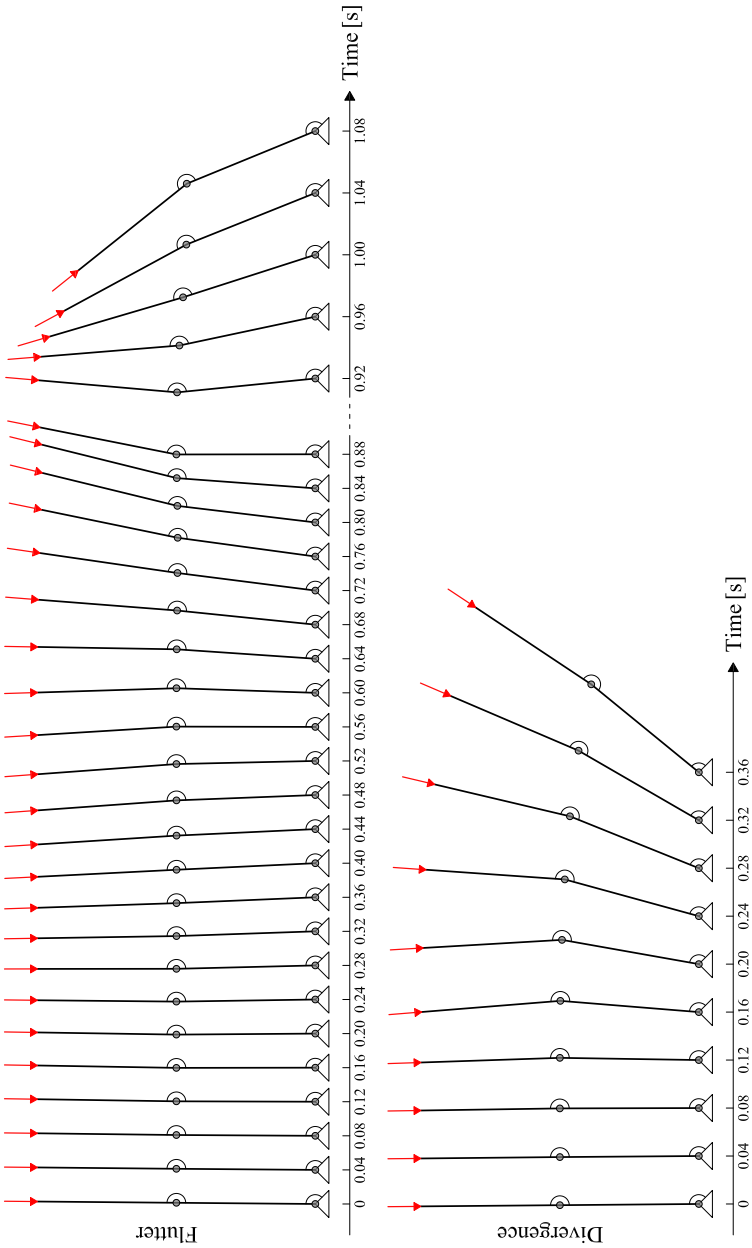

Fig. 5.6: A sequence (1.08 s for flutter and to 0.36 s for divergence) of deformed shapes at consecutive times intervals of 0.04 seconds of the structure sketched in Fig. 5.1 and exhibiting flutter (upper part) and divergence (lower part) instability. Results have been obtained through a numerical analysis of Eqs. (5.7) with initial conditions $\alpha_1 = \alpha_2 = 0.5°$, at the flutter load $(W_f + W_d)/2$ (upper part) and at the divergence load $1.75\,W_d$ (lower part), Eq. (5.12). The values employed for the analysis are reported in Tab. 5.2.

Note that the initial velocity has been taken equal to $\dot{\alpha}_1 = \dot{\alpha}_2 = 0.5\,\mathrm{rad/s}$, since in the experiment we have observed first a slight deviation from rectilinearity and then a movement to reach the straight configuration before the initiation of flutter. We can observe that cusps form in the predicted behaviour when the steady motion is reached, a feature which is present also in the experiment and which is related with the decrease to zero of $\dot{C}_p^r$. We have found that the slip velocity $\dot{C}_p^r$ never became negative in all nonlinear simulations that we have performed.

We have observed some of the scratches left by the wheel on the aluminum plate during the experiments, using an optical microscope (with a Nikon SMZ800 stereo-zoom microscope equipped with Nikon Plan Apo 0.5x objective and a Nikon DD-FI1 high definition color camera head), without finding traces of detachments.

5.3 Experimental results

We have performed experiments with three different prototypes of the two-degree-of-freedom structure sketched in Figs. 5.3 and 5.4, always finding flutter and divergence instabilities for appropriate loads. In the first prototype the elastic hinges were realized with thin steel strips working under flexure, while for the other structures these have been realized as true hinges without (in the case of the second prototype) and with (in the case of the third prototype) ball bearings. In this way the viscous behaviour of the hinges in the three prototypes was markedly different. We have tried a series of different wheel/plate friction conditions, first using an aluminum wheel sliding on paper, then sliding on P2000-sand paper, later, using a steel wheel sliding on a sandblasted-steel plate and, finally, we have used a steel wheel sliding against an aluminum plate.

Since the rotational inertia of the wheel introduces a force transversal to the axis of the structure, we have checked the influence of this effect in the three prototypes by employing five different wheels, one in aluminum (V-shaped cross section, external diameter 15 mm, thickness 5 mm and weight 3 gr) and four in steel (one with V-shaped cross section, external diameter 25 mm, thickness 6 mm and weight 17 gr; three cylindrical with external diameter 25 mm, thicknesses 5, 6 and 10 mm and weights 18, 22 and 36 gr), so that we have proved that, within the dimension range of our

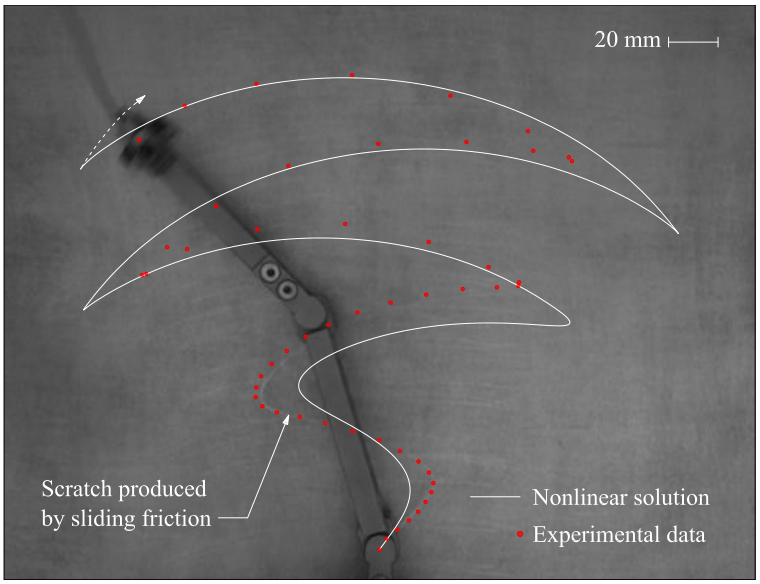

Fig. 5.7: The scratch left by the wheel on the plate compared with the nonlinear solution of Eqs. (5.7) with $W = (W_f + W_d)/2$, v_p =100 mm/s and initial conditions $\alpha_1 = \alpha_2 = 0°$ and $\dot{\alpha}_1 = \dot{\alpha}_2 = 0.5$ rad/s. The red spots along the scratches are positions of the wheel corresponding to photos taken with the high speed camera; the scratch left during the experiment is clearly visible in the initial part of the test, not evidencing detachments. The whole sequence corresponds to 2.04 s.

prototypes, the mass of the wheel and the real dimensions of the contact area (which reduces to a point only in ideal conditions) do not affect much the instability.

The two initial prototypes have both broken during experiments to detect divergence instability, so that we have limited in the third prototype the stroke of the model. Precise measurements have been carried out only using the third prototype, specially designed with this purpose. While we will limit the presentation to the third prototype in the following, we stress now the point that since flutter was always observed at sufficiently high loading, the phenomenon has been found to occur: (i.) with the different viscosity related to the different mechanical realization of the hinges, (ii.) with different friction conditions at the wheel/plate contact

(aluminum/paper, aluminum/P2000-sand paper, steel/sandblasted-steel, steel/aluminium) and (iii.) with different geometries and stiffnesses, always in agreement with the theoretical modelling.

5.3.1 Experimental setting

The two-degree-of-freedom system sketched in Figs. 5.3 and 5.4 has been realized as shown in Fig. 5.8 with two 100 mm long stainless steel AISI 304 rods with a cross section of external dimensions equal to 30 mm × 10 mm. The rods are connected trough hinges realized using ball bearings

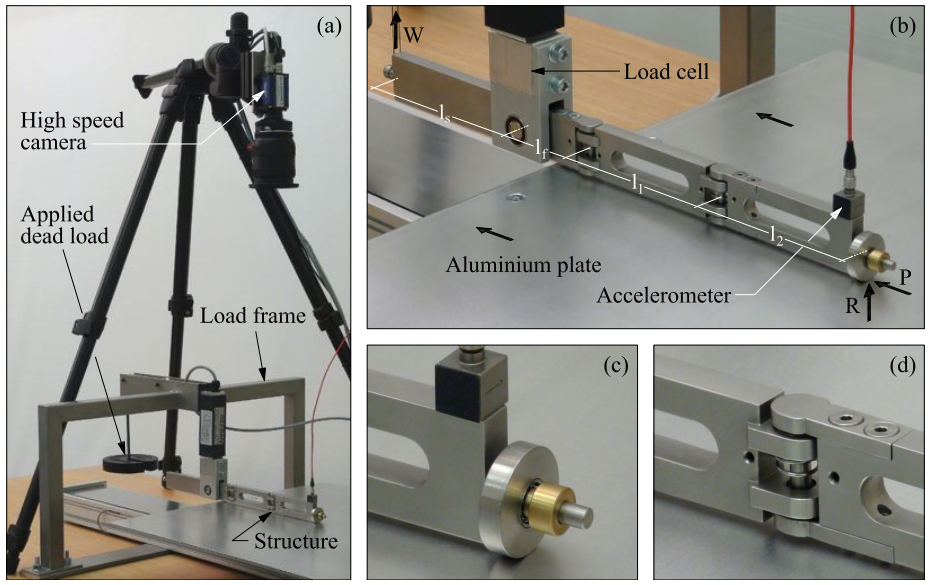

Fig. 5.8: The practical realization of the concept exemplified in Figs. 5.3 and 5.4. (a) A global view of the experimental setting; (b) a detail of the whole structure suffering instability; (c) detail of the structure: the wheel (a 25 mm diameter steel cylinder, 6 mm thick) and the accelerometer; (d) detail of the structure: an elastic hinge.

(SKF, mod. 628/5-2Z), with a torsional spring obtained from a (1 mm diameter) music wire ASTM A228. The wheel, of diameter d=25 mm, mounted (with two ball bearings SKF, mod. 618/5) at the top of the final rod is made of stainless steel AISI 304 and the structure is hinged (with

two ball bearings SKF, mod. 61800) to the loading frame through a load cell (Gefran S.p.A., mod. OC-K5U-C3), to measure the axial force (along $\mathbf{e}_1$).

The plate sliding against the structure is a 500 mm×1000 mm×5 mm aluminium alloy 6082 plate moved through a linear drive unit (Damo S.r.l., mod. AMV120LB), equipped with an ABB AC servo motor (mod. BSM0400CN00) and controlled with and ABB servo drive (mod. BSD0400), both purchased from ABB Sace S.p.A. The plate has been polished with sandpaper P100. An IEPE accelerometer (PCB Piezotronics Inc., mod. 333B50) has been attached at the top of the final piece of the structure. Photos of the system have been taken with a high speed camera (Genie HM1400 from DALSA Corporation), equipped with AF Nikkor (18-35 mm 1:3.5-4.5 D) lens (Nikon Corporation) and a movie has been recorded during the whole test with a Sony handycam (mod. HDR-XR550VE). The axial force, the transversal acceleration (along $\mathbf{e}_\theta$) and the position of the plate have been acquired with a sample rate of 5 kS/s through a NI PXI-6221 data acquisition system, interfaced with Labview 8.5.1 (National Instruments).

The viscosity of the hinges has been measured in the following way. The central hinge of the system has been blocked, so that the structure has been reduced to a one-degree-of-freedom elastic pendulum ($\alpha_1 = \alpha_2$), which has been left free of oscillating starting from an initial configuration at $\alpha_1 = 45°$, for different values of load W, with the plate advancing at a constant speed of 50 mm/s. The deformations of the structure have been recorded with the high-speed camera at 25 frames per second and the parameter β_1 has been estimated through comparison with the solution of the free damped vibrations of a pendulum. The results are reported in Tab. 5.1. Although we have found that the viscosity of the hinges depends

W_i	19.5 N	24.5 N	29.5 N	34.5 N	39.5 N
β_i	0.0036 N m s	0.0041 N m s	0.0052 N m s	0.0074 N m s	0.0095 N m s
Mean and standard deviation of the parameters β_1 and β_2= {0.006; 0.0025}N m s					

Tab. 5.1: Measured values of the viscosity parameters β_1 and β_2 as a function of the applied dead load W characterizing the structure shown in Fig. 5.8.

on W, an effect related to the fact that an increase in the applied weight yields an increase of the dissipation within the bearings, a good approxi-

mation to the viscosity of the hinges (β_1 and β_2, taken to be equal) has been found that reported in Tab. 5.2, where all parameters characterizing the geometry and the mechanical behaviour of the structure shown in Fig. 5.8 have been reported, to be used for numerical simulations [5]. The

Lengths of the rods		Hinges charact.		General data	
l_1	100 mm	k_1	0.189 N m	ρ	1.84 g/mm
l_2	100 mm	k_2	0.189 N m	μ_s	0.61 ± 0.06
l_f	50 mm	β_1	0.006 N m s	μ_d	0.47 ± 0.05
l_s	125 mm	β_2	0.006 N m s	d	25 mm

Tab. 5.2: Measured valued of the parameters characterizing the structure shown in Fig. 5.8 and used in the numerical simulations.

friction coefficients (between steel and aluminum) in the table have been evaluated as mean values of the axial forces measured during all the tests during the stable behaviour and fit the values available in the literature (Minshall, 1992). Using the values listed in the table, we can estimate the critical loads for flutter and divergence from Eqs. (5.12). These, in the absence of viscosity ($\beta_1 = \beta_2 = 0$), result to be $W_f = 20.5$ N and $W_d = 37.5$ N, which become 14.4 N and 55.9 N when the viscosity of the hinges is kept into account.

Note that all the values listed in Tab. 5.2 have been determined *independently* from flutter and divergence experiments and will be found to nicely fit these experiments.

5.3.2 The evidence of flutter and divergence instabilities induced by friction

Since the interval of loads W corresponding to flutter and divergence is know, we can test these instabilities on the structure shown in Fig. 5.8 (b) by increasing the load W from a stable situation. The result is shown in Fig. 5.9, where an experimental investigation of the critical loads for flutter and divergence instability is reported. We have not found any dependence of the critical loads on the plate velocity v_p, which has been

[5] We have performed numerical simulations of our prototype introducing a rolling friction at the wheel, but the results were not in line with the obtained experiments, so that we have concluded that the viscosity of the hinges is a factor dominating rolling friction.

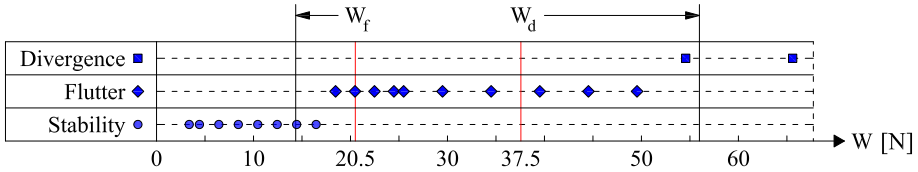

Fig. 5.9: Experimental investigation on flutter and divergence instability at increasing load W at v_p=50 mm/s. The elastic model predicts flutter instability to occur at W_f and divergence at W_d; these values are corrected to $0.70\,W_f$ and $1.49\,W_d$ when viscosity at the hinges is included.

imposed equal to 50 mm/s to measure the values reported in Fig. 5.9. Note that the elastic model predicts flutter at W_f and divergence at W_d and this interval is 'broadened' (note the arrows in the figure) to $0.7\,W_f$ and $1.49\,W_d$, when viscosity of the hinges is kept into account (see Appendix A). This broadening of the flutter range is consistent with our experimental results shown in Fig. 5.9. The discrimination between stability and flutter instability has been performed through visual inspection and documented with the photographic record. This discrimination has been found easy, while some difficulties have been found in distinguishing between flutter and divergence instability in the transition zone between the two phenomena.

A sequence of photos taken with the high-speed camera (with the Sony handycam) at 25 shots per second is shown in Fig. 5.10 (in Fig. 5.11) documenting a case of *flutter instability* at a load $W = (W_f + W_d)/2$ and a speed of 75 mm/s of the aluminum plate. The vibrational motion of increasing amplitude is evident from both Figs. 5.10 and 5.11. Note that the sequence of photos corresponds to the sequence of configurations reported in Fig. 5.6 (upper part), so that the direct comparison results to be excellent.

The measured load (upper part: a, b) and acceleration (lower part: c, d) versus time during a flutter test at a load $W = (W_f + W_d)/2 = 29\,\mathrm{N}$ are reported in Fig. 5.12, for a plate velocity of 75 mm/s (a detail of the curve on the left is shown on the right). Results of the numerical nonlinear (linear viscoelastic) simulation are also reported in red (in blue) for the initial 6 s (1.5 s), with initial conditions $\alpha_1 = \alpha_2 = 0.5^\circ$ and $\dot{\alpha}_1 = \dot{\alpha}_2 = 0$.

Fig. 5.10: A sequence of photos (taken with a high-speed camera at 25 frames per second) of the structure sketched in the lower part of Fig. 5.8 and exhibiting flutter instability. Note the blurred photos, denoting increasing velocity of the motion. The whole sequence of photos has been recorded in 1.08 seconds and the time interval between two photos was 0.04 seconds. The experiment refers to $W = (W_f + W_d)/2$ and $v_p = 75$ mm/s. The plate is advancing vertically from the top to the bottom. This sequence of photos can directly be compared with the sequence of configurations shown in Fig. 5.6, upper part.

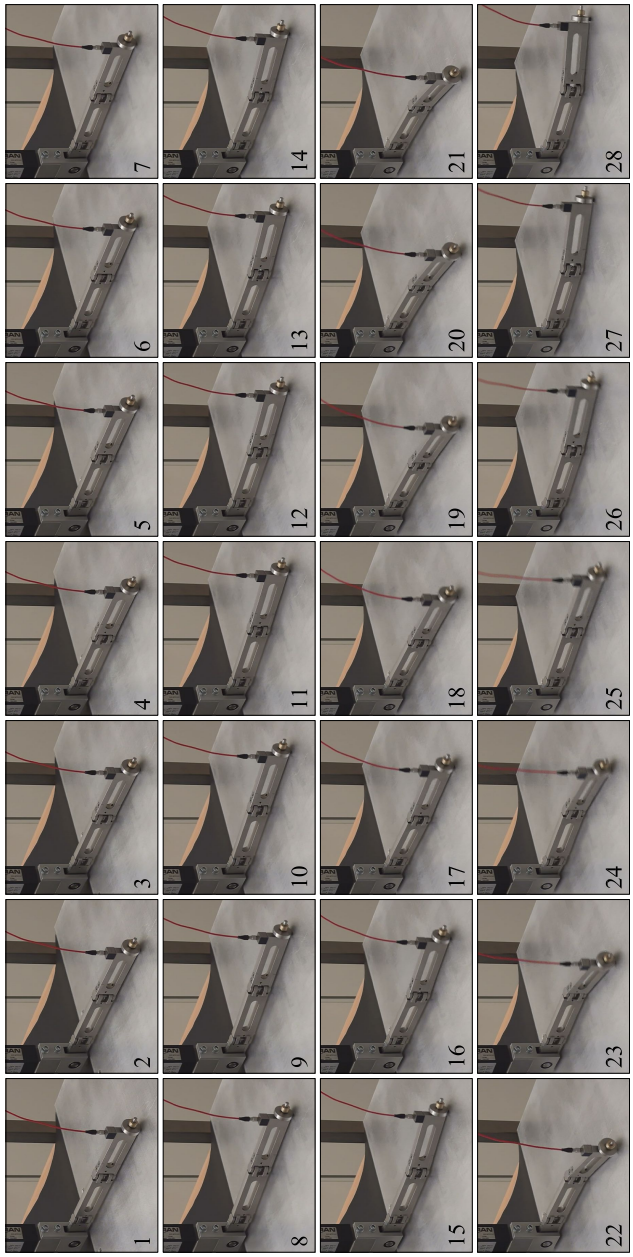

Fig. 5.11: A sequence of photos (taken from a movie recorded with a Sony handycam at 25 frames per second) of the structure sketched in the lower part of Fig. 5.8 and exhibiting flutter instability. The whole sequence of photos has been recorded in 1.08 seconds and the time interval between two photos was 0.04 seconds. The experiment refers to $W = (W_f + W_d)/2$ and $v_p = 75\,\mathrm{mm/s}$.

Note from Fig. 5.12 the initial increase in the amplitude of the acceleration,

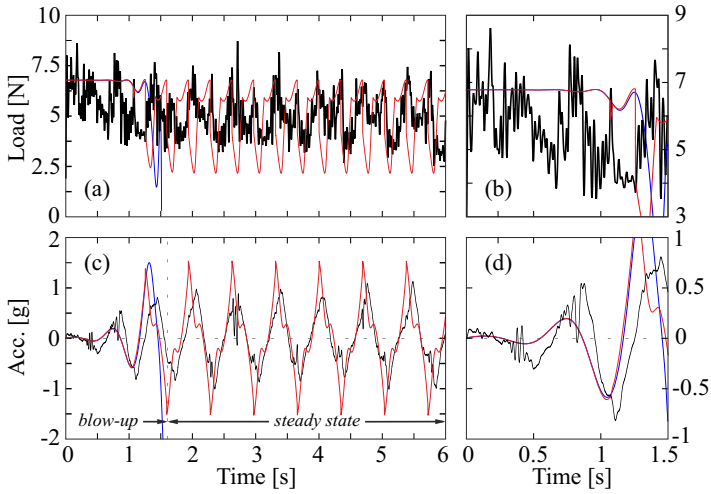

Fig. 5.12: Measured load (a) and acceleration (c) versus time during the flutter test reported in Figs. 5.10 and 5.11, at a load $W = (W_f + W_d)/2$ and for a plate velocity of 75 mm/s. Parts (b) and (d) are details of (a) and (c) respectively, referred to the initial 1.5 s. Results of the numerical nonlinear (linear with viscosity) simulation at the same load and with initial conditions $\alpha_1 = \alpha_2 = 0.5°$ are reported in red (in blue). Note the initial increase in the amplitude of the acceleration denoting flutter (well captured even by the linearized viscoelastic analysis), and the following stabilization (captured by the nonlinear analysis), due to the effect of the nonlinearities.

denoting flutter, and the following stabilization, when a steady situation is reached. *The attainment of a steady dynamics at large displacement is an important conclusion of our study.*

It is important to point out that, although the onset of flutter and the transition between flutter and divergence have been found independent of the plate velocity, we have found a dependence on this velocity of the *maximum amplitude of displacement reached during steady motion in flutter conditions*. This dependence is connected with the attainment of the stick/slip condition $\dot{C}_p^r \leq \varepsilon$, in the sense that the smaller is the velocity, the earlier the stick condition is attained and the oscillation inverted. This behaviour is consistent with the fact that the velocity of the plate is essential to satisfy the sliding condition and ensures the validity of the

linearized analysis to capture the onset of the instability. It is clear that the effects of the instability become more 'intense' when the velocity of the plate is increased. These observations is fully confirmed by the numerical simulations of the nonlinear equations (5.7), so that a comparison between theoretical predictions and measured values is reported in Fig. 5.13.

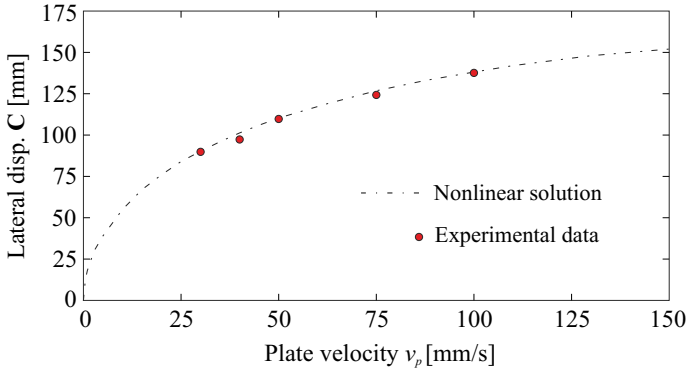

Fig. 5.13: Maximum lateral displacement of the end point **C** of the structure as a function of the plate velocity v_p when the steady state motion is reached. The black dashed curve is obtained through the numerical solution of Eqs. (5.7), for different plate velocities and an applied dead load $W = (W_f + W_d)/2$; the red spots are the experimental data.

Two sequences of photos taken with the high-speed camera and with the Sony handycam, both at 25 shots per second, is shown in Fig. 5.14, documenting a case of *divergence instability* at a load $1.75\,W_d$ and a speed of 50 mm/s of the aluminum plate. In the experimental setting a lateral rubber constraint has been added to prevent possible failure of the equipment. In fact the motion caused by divergence instability has been found to be particularly violent. As in the case of flutter, the blowing-up character of divergence instability is clearly visible in the figure. Note that the sequence of photos can be directly compared with the sequence of configurations shown in Fig. 5.6, lower part, and show excellent agreement.

Finally, a case of stability is documented with a 5 seconds long sequence of photos, taken (with a Sony handycam) at a time intervals of 1 s, and is reported in Fig. 5.15 at a load W=5 N, and at a speed of the aluminum

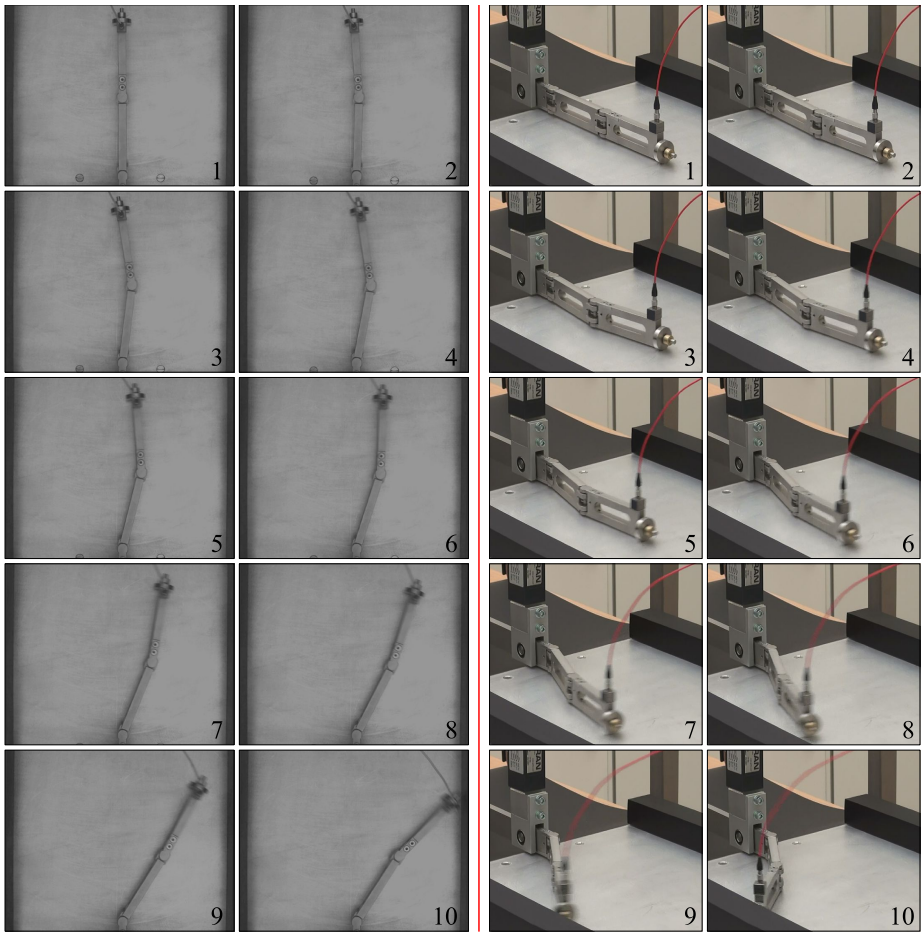

Fig. 5.14: Two sequences of photos (taken with a high-speed camera, on the left, and with a Sony handycam, on the right, at 25 frames per second) of the structure sketched in the lower part of Fig. 5.8 and exhibiting divergence instability. The whole sequence of photos has been recorded in 0.36 seconds and the time interval between two photos was 0.04 seconds. The experiment refers to $W = 1.75\, W_d$ and $v_p = 50\,\mathrm{mm/s}$. The sequence of photos on the left can be directly compared with the sequence of configurations shown in Fig. 5.6, lower part.

plate of 50 mm/s.

During our experiments we have also recorded the noise generated

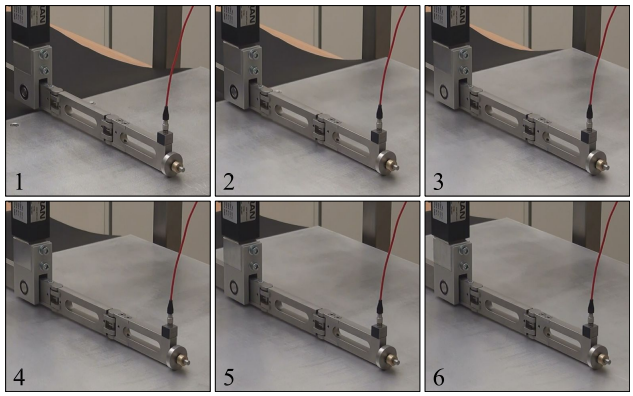

Fig. 5.15: A sequence of photos (taken with a Sony handycam) of the structure sketched in the lower part of Fig. 5.8 within the region of stability. The whole sequence of photos has been recorded in 5 s and the time interval between two photos was 1 s. The experiment refers to W=5 N and $v_p = 50$ mm/s.

during sliding and we have carefully observed the rotational motion of the wheel. The emitted noise highlights the vibrational character of flutter instability and the rotational motion of the wheel shows that there is no inversion of the rotation before the end of an oscillation is reached, in agreement with our model.

In closure, we note that all instabilities are suppressed in our system if the central hinge (Fig. 5.8 d) is blocked, since the follower load induced by friction does not work. Moreover, divergence instability and buckling occur, *but not flutter*, if the wheel is prevented from rotating. These two behaviours have been both studied and checked experimentally, see B.

5.4 A final discussion

Flutter and divergence instabilities have been experimentally demonstrated to occur in a two-degree-of-freedom elastic structure, as related to dry friction, in full agreement with theoretical predictions. In particular, all the following phenomena, documented in various experiments with different settings, are all quantitatively predicted by the theoretical modelling and fully interpretable as friction-induced flutter or divergence

instabilities.

- Experiments performed on three different realizations of the structure sketched in Figs. 5.3 and 5.4 have all shown at increasing load: nearly-null vibrations (interpreted as stable behaviour, Fig. 5.15), blowing-up oscillations becoming large and steady after 1–2 seconds (interpreted as flutter, Figs. 5.10 and 5.11) and, finally, exponentially growing motion (interpreted as divergence instability, Fig. 5.14).

- Since the three structures had different geometries, stiffnesses, types of elastic hinges and wheel/plate friction coefficients, the instabilities are quantitatively *but not qualitatively* affected by all these parameters and, in particular, by the viscosity at articulations and by the value of the friction coefficient at the wheel/plate contact.

- While the amplitude of the vibrations during steady motion has been found to depend on the sliding velocity of the plate, the onset of flutter has been found independent of this.

- The *accelerations* measured at the tip of the structure and the *noise* recorded during the tests show initially an oscillatory blow-up, which finally reaches a steady-state, during flutter instability (Fig. 5.12).

- No evidences of detachment at the wheel/plate contact have been found at a microscope investigation of the scratches on the plate.

- The wheel rotates during instability and does not invert rotation before the end of an oscillation.

- When the wheel is prevented from rotating, three behaviours are found at increasing load: nearly-null vibrations (interpreted as stable behaviour), growing motion with low acceleration and without vibrations (interpreted as divergence instability, Fig. 5.17 upper part) and, finally, stick of the wheel with flexure of the structure (interpreted as buckling, Fig. 5.17 lower part).

- When the central hinge of the structure is blocked, the structure is found to have nearly-null vibrations at every load level (stable behaviour, Fig. 5.18).

Neither any evidence against the model of flutter or divergence instabilities, nor possibilities of describing these phenomena with different models, have been found. Our experiments show that a follower load of tangential type can be easily obtained by exploiting a constraint with Coulomb friction. Moreover, the fully nonlinear dynamics which develops in flutter conditions shows that the system reaches a steady state, in which the maximum amplitude of the motion depends on the initial relative velocity at the friction contact.

A Details of the analysis for the two d.o.f. system shown in Fig. 5.1

We provide details of the stability analysis of the structure shown in Fig. 5.1, which have been omitted in Section 5.2.

Denoting the time derivative by a superimposed dot, the velocities of points $\mathbf{C}$, $\mathbf{G}_1$ and $\mathbf{G}_2$ can be obtained from Eqs. (5.1) as

$$\begin{aligned}
\dot{\mathbf{C}} =& -\{l_1\dot{\alpha}_1 \sin\alpha_1 + l_2\dot{\alpha}_2 \sin\alpha_2\}\mathbf{e}_1 + \\
&+\{l_1\dot{\alpha}_1 \cos\alpha_1 + l_2\dot{\alpha}_2 \cos\alpha_2\}\mathbf{e}_2, \\
\dot{\mathbf{G}}_1 =& -\{l_1\dot{\alpha}_1 \sin\alpha_1/2\}\mathbf{e}_1 + \{l_1\dot{\alpha}_1 \cos\alpha_1/2\}\mathbf{e}_2, \\
\dot{\mathbf{G}}_2 =& -\{l_1\dot{\alpha}_1 \sin\alpha_1 + l_2\dot{\alpha}_2 \sin\alpha_2/2\}\mathbf{e}_1 + \\
&+\{l_1\dot{\alpha}_1 \cos\alpha_1 + l_2\dot{\alpha}_2 \cos\alpha_2/2\}\mathbf{e}_2,
\end{aligned} \tag{5.14}$$

so that the accelerations of the mass center of the two rigid bars are

$$\begin{aligned}
\ddot{\mathbf{G}}_1 =& -\{(l_1/2)(\ddot{\alpha}_1 \sin\alpha_1 + \dot{\alpha}_1^2 \cos\alpha_1)\}\mathbf{e}_1 + \\
&+\{(l_1/2)(\ddot{\alpha}_1 \cos\alpha_1 - \dot{\alpha}_1^2 \sin\alpha_1)\}\mathbf{e}_2, \\
\ddot{\mathbf{G}}_2 =& -\{l_1(\ddot{\alpha}_1 \sin\alpha_1 + \dot{\alpha}_1^2 \cos\alpha_1) + \\
&+(l_2/2)(\ddot{\alpha}_2 \sin\alpha_2 + \dot{\alpha}_2^2 \cos\alpha_2)\}\mathbf{e}_1 + \\
&+\{l_1(\ddot{\alpha}_1 \cos\alpha_1 - \dot{\alpha}_1^2 \sin\alpha_1) + \\
&+(l_2/2)(\ddot{\alpha}_2 \cos\alpha_2 - \dot{\alpha}_2^2 \sin\alpha_2)\}\mathbf{e}_2.
\end{aligned} \tag{5.15}$$

The expressions (5.14) and (5.15) are employed to write down the principle of virtual works (5.6), from which the differential equations governing the dynamics of the structure, Eqs. (5.7), follow.

A.1 Linearized analysis of the elastic structure

For a flutter analysis in the absence of viscosity, solutions of the linearized equations of motion (5.10) are sought in the time-harmonic form

$$\alpha_j = A_j\, e^{-i\Omega t}, \quad j = 1, 2 \tag{5.16}$$

where A_j are (complex) amplitudes, Ω is the circular frequency, and i is the imaginary unit ($i = \sqrt{-1}$), so that a substitution of Eq. (5.16) into Eqs. (5.10) yields

$$\begin{bmatrix} \left(1+\frac{\lambda}{3}\right)\omega^2+\gamma-k-1 & \frac{\omega^2}{2\lambda}-\gamma+1 \\ \frac{\omega^2}{2\lambda}+1 & \frac{\omega^2}{3\lambda^2}-1 \end{bmatrix} \begin{Bmatrix} A_1 \\ A_2 \end{Bmatrix} = \begin{Bmatrix} 0 \\ 0 \end{Bmatrix}, \quad (5.17)$$

where

$$\gamma = \frac{Pl_1}{k_2}, \qquad \omega^2 = \frac{l_1^2 l_2 \rho}{k_2}\Omega^2. \quad (5.18)$$

Non-trivial solution of system (5.17) is possible if the determinant of the matrix vanishes, a condition which immediately provides the solutions

$$\omega^2 = \frac{b(\gamma) \pm \sqrt{\Delta(\gamma)}}{1+(4/3)\lambda}, \quad (5.19)$$

where

$$\Delta(\gamma) = b^2(\gamma) - 4k\lambda^2(3+4\lambda) \quad (5.20)$$

and

$$b(\gamma) = -\gamma(2+3\lambda) + 2(1+\lambda)^3 + 2k, \quad (5.21)$$

so that

$$\Omega = \frac{1}{l_1}\sqrt{\frac{k_2}{l_2\rho}}\,\omega. \quad (5.22)$$

We note that $k > 0$, $\lambda > 0$ and $\Delta(\gamma) < b^2(\gamma)$ and that

$$\begin{aligned} b(\gamma) > 0 \quad &\Leftrightarrow \quad \gamma < \frac{k+(1+\lambda)^3}{1+(3/2)\lambda}, \\ \Delta(\gamma) < 0 \quad &\Leftrightarrow \quad 0 < \gamma_f < \gamma < \gamma_d, \end{aligned} \quad (5.23)$$

where

$$\gamma_{\substack{f \\ d}} = \frac{k+(1+\lambda)^3 \mp \lambda\sqrt{k(3+4\lambda)}}{1+(3/2)\lambda}, \quad (5.24)$$

so that following three possibilities only arise:

- two real and positive values for ω^2, corresponding to $b(\gamma) > 0$ and $\Delta(\gamma) > 0$. There are four Ω, two positive and two negative and vibrations are sinusoidal, a situation which corresponds to *stability*;

- two complex conjugate values for ω^2, corresponding to $\Delta(\gamma) < 0$. There are two complex-conjugate pairs of Ω, so that there are four exponential solutions, two blowing up and the other two decaying with time, a situation corresponding to *flutter instability*;

- two real and negative values for ω^2, corresponding to $b(\gamma) < 0$ and $\Delta(\gamma) > 0$. There are two purely imaginary complex-conjugate pairs of Ω, so that vibrations are exponential with time (one amplifying and the other decaying), a situation corresponding to *divergence instability*.

As a conclusion

- *flutter instability* occurs when $\gamma_f < \gamma < \gamma_d$, a condition identical (though written in a different notation) to Eq. (5.12).

- and *divergence instability* occurs when $\gamma > \gamma_d$.

A.2 Linearized analysis of the viscoelastic structure

A linear viscoelastic analysis can be performed through a linearization of Eqs. (5.7) near the trivial solution ($\alpha_1 = \alpha_2 = 0$), yielding

$$\begin{cases} \rho \dfrac{l_1^2}{3}(l_1 + 3l_2)\,\ddot{\alpha}_1 + \rho \dfrac{l_1 l_2^2}{2}\ddot{\alpha}_2 + (\beta_1 + \beta_2)\dot{\alpha}_1 - \beta_2\dot{\alpha}_2 + \\ + (k_1 + k_2)\alpha_1 - k_2\,\alpha_2 - l_1 P(\alpha_1 - \alpha_2) = 0, \\ \rho \dfrac{l_1 l_2^2}{2}\ddot{\alpha}_1 + \rho \dfrac{l_2^3}{3}\ddot{\alpha}_2 - \beta_2(\dot{\alpha}_1 - \dot{\alpha}_2) - k_2(\alpha_1 - \alpha_2) = 0. \end{cases} \tag{5.25}$$

We look now for time-harmonic vibrations near the equilibrium configuration, so that we seek solutions of Eqs. (5.25) in the form (5.16), so

that a substitution into Eqs. (5.25) yields

$$\begin{bmatrix} \left(1+\frac{\lambda}{3}\right)\omega^2+\eta(\beta+1)\omega-\gamma+k+1 & \frac{\omega^2}{2\lambda}-\omega\eta+\gamma-1 \\ \frac{\omega^2}{2\lambda}-\omega\eta-1 & \frac{\omega^2}{3\lambda^2}+\omega\eta+1 \end{bmatrix} \times \\ \times \begin{Bmatrix} A_1 \\ A_2 \end{Bmatrix} = \begin{Bmatrix} 0 \\ 0 \end{Bmatrix} \tag{5.26}$$

where

$$\beta=\frac{\beta_1}{\beta_2}, \qquad \omega=-i\,l_1\sqrt{\frac{l_2\rho}{k_2}}\,\Omega, \qquad \eta=\sqrt{\frac{\beta_2^2}{l_1^2 l_2 k_2 \rho}}. \tag{5.27}$$

Non-trivial solution of system (5.26) is possible if the determinant of the

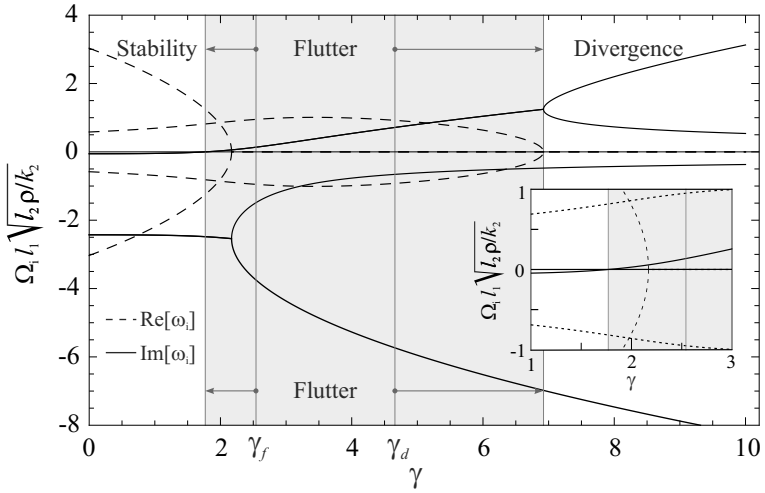

Fig. 5.16: Real and imaginary part of the solutions $\Omega_i\, l_1\sqrt{l_2\rho/k_2}$ as a function of the loading parameter γ and obtained solving the characteristic equation (5.28). Note the broadening of the flutter region due to damping.

matrix vanishes, a condition which immediately provides the characteristic

equation

$$p_0\omega^4 + p_1\omega^3 + p_2\omega^2 + p_3\omega + p_4 = 0, \tag{5.28}$$

where the coefficients are

$$\begin{aligned} p_0 &= 1/4 + \lambda/3 > 0, \\ p_1 &= \eta[\beta + (1+\lambda)^3] > 0, \\ p_2 &= \lambda^3 + 3\lambda^2(1+\beta\eta^2) + 3\lambda + k - \gamma(1 - 3\lambda/2) + 1, \\ p_3 &= 3\lambda^2(k+\beta)\eta > 0, \\ p_4 &= 3\lambda^2 k > 0. \end{aligned} \tag{5.29}$$

In this context we have the following possibilities for a solution Ω_i:

- $\mathrm{Im}[\Omega_i] < 0$ stability,
- $\mathrm{Im}[\Omega_i] > 0$ and $\mathrm{Re}[\Omega_i] \neq 0$ flutter,
- $\mathrm{Im}[\Omega_i] > 0$ and $\mathrm{Re}[\Omega_i] = 0$ divergence.

The numerical determination of the solutions of Eq. (5.28), assuming $\lambda = k = \beta = 1$ and $\eta = 0.32$, the values corresponding to the structure tested in our experiments (Tab. 5.2), reveals that flutter occurs within the interval $0.70W_f < W < 1.49W_d$, while for $W < 0.70W_f$ the system is stable and, finally, divergence occurs for $W > 1.49W_d$. The situation is sketched in Fig. 5.16, where the real and imaginary parts of the solutions $\Omega_i\, l_1\sqrt{l_2\rho/k_2}$ are reported as a function of the loading parameter γ. In the figure, the values γ_f and γ_d correspond to flutter and divergence instabilities in the absence of viscosity, so that we may see that the introduction of the viscosity broadens the interval of flutter.

B Wheel prevented from rotating and one-degree-of-freedom system

To complete our study, we analyze the case in which the wheel in the structure shown in Fig. 5.8(c) is blocked and the case in which the structure is reduced to a one-degree-of-freedom system by blocking the central hinge (but leaving free the wheel). In the former case there is no flutter, but divergence and quasi-static buckling occur, whereas in the latter case the behaviour is always stable. Our experiments confirm these theoretical findings.

B.1 Wheel prevented from rotating

If the wheel is replaced with a fixed contact (we have blocked the wheel with a screw), the system becomes subjected to a frictional force, which assuming sliding can be written as

$$\begin{aligned} \mathbf{P} &= -P\,\frac{\dot{\mathbf{C}}_p}{|\dot{C}_p|}, \\ P &= \mu_d\,\frac{l_s}{l_f + l_1\cos\alpha_1 + l_2\cos\alpha_2}\,W. \end{aligned} \tag{5.30}$$

Eq. (5.30), can be linearized near the configuration $\alpha_1 = \alpha_2 = 0$ assuming $v_p >> l_1\dot{\alpha}_1 + l_2\dot{\alpha}_2$, so that it becomes

$$\begin{aligned} \mathbf{P} &= -\{P\}\mathbf{e}_1 - \{P(l_1\dot{\alpha}_1 + l_2\dot{\alpha}_2)/v_p\}\mathbf{e}_2 \\ P &= \mu_d\,\frac{l_s}{l_f + l_1 + l_2}\,W \end{aligned} \tag{5.31}$$

and Eqs. (5.10) become

$$\begin{cases} \rho\,\dfrac{l_1^2}{3}\,(l_1 + 3l_2)\,\ddot{\alpha}_1 + \rho\,\dfrac{l_1 l_2^2}{2}\ddot{\alpha}_2 + (k_1 + k_2)\alpha_1 - k_2\,\alpha_2 + \\ - l_1 P\alpha_1 + l_1 P\,\dfrac{l_1\dot{\alpha}_1 + l_2\dot{\alpha}_2}{v_p} = 0, \\ \rho\,\dfrac{l_1 l_2^2}{2}\ddot{\alpha}_1 + \rho\,\dfrac{l_2^3}{3}\ddot{\alpha}_2 - k_2\,\alpha_1 + k_2\,\alpha_2 + \\ - l_2 P\alpha_2 + l_2 P\,\dfrac{l_1\dot{\alpha}_1 + l_2\dot{\alpha}_2}{v_p} = 0. \end{cases} \tag{5.32}$$

We look now for time-harmonic vibrations near the equilibrium configuration, so that the Lagrangean parameters are now assumed to be harmonic functions of time (5.16), so that a substitution into Eqs. (5.32)

yields

$$\left[\begin{array}{cc} \left(1+\dfrac{\lambda}{3}\right)\omega^2+\gamma\nu\omega-\gamma+k+1 & \dfrac{\omega^2}{2\lambda}+\dfrac{\omega\gamma\nu}{\lambda}-1 \\ \dfrac{\omega^2}{2\lambda}+\dfrac{\omega\gamma\nu}{\lambda}-1 & \dfrac{\omega^2}{3\lambda^2}+\dfrac{\omega\gamma\nu}{\lambda^2}-\dfrac{\gamma}{\lambda}+1 \end{array}\right]\times \\ \times\left\{\begin{array}{c} A_1 \\ \\ A_2 \end{array}\right\}=\left\{\begin{array}{c} 0 \\ \\ 0 \end{array}\right\} \tag{5.33}$$

where

$$\omega=-i\,l_1\sqrt{\frac{l_2\rho}{k_2}}\,\Omega, \qquad \nu=\frac{1}{v_p}\sqrt{\frac{k_2}{l_2\rho}}. \tag{5.34}$$

Non-trivial solution of system (5.33) is possible if the determinant of the matrix vanishes, a condition which provides the characteristic equation

$$p_0\omega^4+p_1\omega^3+p_2\omega^2+p_3\omega+p_4=0, \tag{5.35}$$

where the coefficients are

$$\begin{aligned} p_0&=1/4+\lambda/3,\\ p_1&=\gamma(1+\lambda)\nu,\\ p_2&=k+(1+\lambda)^3-\gamma[1+\lambda(3+\lambda)],\\ p_3&=3\gamma[k+(1-\gamma+\lambda)(1+\lambda)]\nu,\\ p_4&=3\lambda[\gamma^2+k\lambda-\gamma(1+k+\lambda)]. \end{aligned} \tag{5.36}$$

The stability of the system can be analyzed using the Routh–Hurwitz criterion (Ziegler, 1977), which ensures that all the ω_i have negative real part; the criterion for stability requires that

$$\begin{aligned} p_1&>0,\\ p_1p_2-p_0p_3&>0,\\ (p_1p_2-p_0p_3)p_3-p_1^2p_4&>0,\\ p_4&>0. \end{aligned} \tag{5.37}$$

Conditions (5.37) are equivalent to

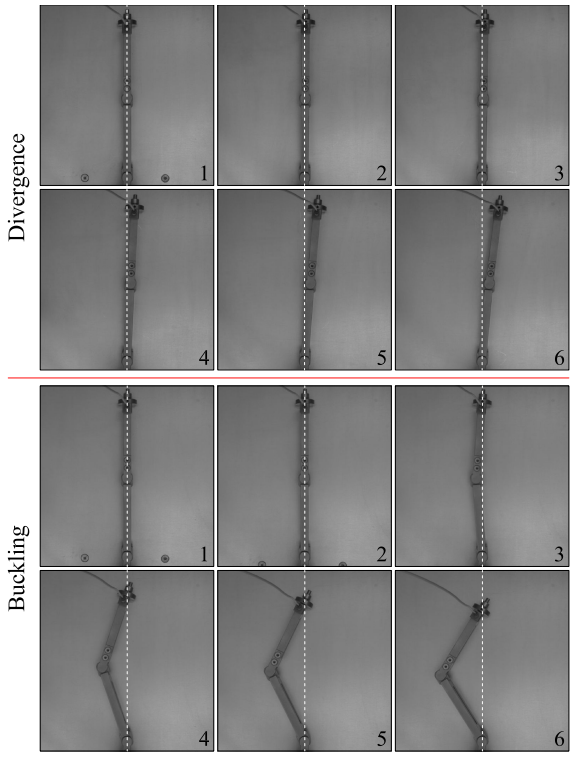

Fig. 5.17: The structure with fixed wheel exhibiting divergence (upper part) and buckling (lower part). The time interval between two consecutive deformed shapes is 1 s for divergence and 0.2 s for buckling, while the whole sequence corresponds to 5 seconds for divergence and to 1 second for buckling. The applied dead loads are, respectively, W=6.5 N and W=16.5 N, while the velocity of the plate is 50 mm/s in both cases.

$$\gamma < \gamma_{cr} = \frac{1 + k + \lambda - \sqrt{(1+k)^2 + \lambda(2 - 2k + \lambda)}}{2}, \tag{5.38}$$

corresponding to the buckling load of the two degree-of-freedom structure, when subjected to a compressive dead load $-\{P\}\mathbf{e}_1$. For $\gamma > \gamma_{cr}$ the structure is unstable and in fact divergence has been experimentally detected, see Fig. 5.17, upper part, referred to a load $W = 6.5\,\mathrm{N}$.

Regarding this instability, we note that its onset is difficult to be detected, since the instability has an extremely mild character and may

manifest itself only after a long plate sliding. Therefore, although the Routh–Hurwitz criterion provides a stability limit of 3.1 N, since the stroke of our plate is only 1 m, we have been able to detect the instability only from a load of 6 N.

Another, more evident, instability has been observed in our experiments (see Fig. 5.17, lower part) at an applied load W higher than that predicted by the Routh–Hurwitz criterion.

In this instability, the wheel already sticks before the plate begins to move, so that a progressive buckling occurs without involving any relative movement at the wheel/plate contact.

In this case, the system is reduced to a single degree-of-freedom structure (lower part of Fig. 5.17) and the critical load can be easily calculated to be (we recall that $\gamma = Pl_1/k_2$)

$$\gamma_{cr}^{b} = \frac{k}{1+\lambda} + \lambda + 1, \tag{5.39}$$

which, assuming a value for static friction, corresponds to a force W that can be easily evaluated.

Note that $\gamma_{cr}^{b} \geq \gamma_{cr}$, so that if the structure would be kept fixed and so 'forced' to reach the slip condition, the divergence dynamical instability would occur instead of the quasi-static buckling, possibly involving stick and slip.

Note that Fig. 5.17, lower part, refers to an applied load equal to 16.5 N, in good agreement with the calculated γ_{cr}^{b}, corresponding to a load W equal to 15.5 N.

B.2 System reduced to one degree-of-freedom by blocking the central hinge

When the central hinge in the structure shown in Fig. 5.8 (d) is fixed and the wheel is left free of rotating, stability is always verified, since the follower force does not work.

We have confirmed this behaviour with a series of experiments in which the hinge between the two rods has been fixed. In these experiments we have raised the vertical load W until 50 N (well inside the region of divergence for the 2 d.o.f. structure), without finding sensible oscillations.

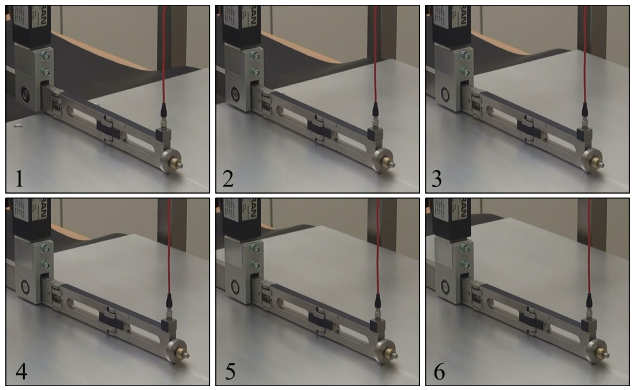

Fig. 5.18: A sequence of photos (taken with a Sony handycam) of the structure with a single d.o.f. (the hinge between the two rods has been fixed), demonstrating stability. The whole sequence of photos has been recorded in 5 seconds, so that the time interval between two photos is 1 seconds. The plate velocity was v_p=50 mm/s and the load W was equal to 29 N.

A sequence of photos taken during one of these experiments with v_p=50 mm/s and W= 29 N is reported in Fig. 5.18, where we observe that the structure remains straight.

BIBLIOGRAPHY

[1] Atkinson, C. (1973) Some ribbon-like inclusion problems. *Int. J. Eng. Sci.*, **11**, 243-266.

[2] Ballarini, R. (1990) A rigid line inclusion at a bimaterial interface. *Eng. Fract. Mech.*, **37**, 1-5.

[3] Beck, M. (1952) Die Knicklast des einseitig eingespannten, tangential gedrückten Stabes. *J. Appl. Math. Phys.*, **3**, 225-228.

[4] Bertoldi, K., Bigoni, D. and Drugan, W.J. (2008) Nacre: an orthotropic and bimodular elastic material. *Compos. Sci. Tech.*, **68**, 1363-1375.

[5] Bigoni, D. (1995) On flutter instability in elastoplastic constitutive models. *Int. J. Solid Struct.*, **32**, 3167-3189.

[6] Bigoni, D. and Loret, B. (1999) Effects of elastic anisotropy on strain localization and flutter instability in plastic solids. *J. Mech. Phys. Solids*, **47**, 1409-1436.

[7] Bigoni, D. and Capuani, D. (2002) Green's function for incremental nonlinear elasticity: shear bands and boundary integral formulation. *J. Mech. Phys. Solids*, **50**, 471-500.

[8] Bigoni, D. and Petryk, H. (2002) A note on divergence and flutter instabilities in elastic-plastic materials. *Int. J. Solid Struct.*, **39**, 911-926.

[9] Bigoni, D. and Capuani, D. (2005) Time-harmonic Green's function and boundary integral formulation for incremental nonlinear elasticity: dynamics of wave patterns and shear bands. *J. Mech. Phys. Solids*, **53**, 1163-1187.

[10] Bigoni, D. and Dal Corso, F. (2008) The unrestrainable growth of a shear band in a prestressed material. *Proc. R. Soc. A*, **464**, 2365-2390.

[11] Bigoni, D., Dal Corso, F. and Gei, M. (2008) The stress concentration near a rigid line inclusion in a prestressed, elastic material. Part II: implications on shear band nucleation, growth and energy release rate. *J. Mech. Phys. Solids*, **56**, 839-857.

[12] Bigoni, D., Gei, M. and Movchan, A.B. (2008) Dynamics of a prestressed stiff layer on an elastic half space: filtering and band gap characteristics of periodic structural models derived from long-wave asymptotics. *J. Mech. Phys. Solids*, **56**, 2494-2520.

[13] Bolotin, V.V. (1963) *Nonconservative problem of the theoty of elastic stability*. Pergamon Press, New York.

[14] Byrd, P.F and Friedman, M.D. (1971) *Handbook of elliptic integrals for engineers and scientists*. Springer-Verlag.

[15] Chen, F. (1996) A high precision photoelasticity procedure for determination of Mode I Stress Intensity Factor K_I. *Int. J. Fract.*, **80**, R55ŰR58.

[16] Clarke, S. and Engelbach, R. (1930) *Ancient Egyptian Masonry: the Building Craft*. Oxford University Press.

[17] Coker, E.G. and Filon, L.N.G. (1957) *A Treatise on Photo-elasticity*. Cambridge University Press.

[18] Como, M. (1966) Lateral buckling of a cantilever subjected to a transverse follower force. *Int. J. Solid Struct.*, **2**, 515-523.

[19] Coppersmith, S.N., Liu, C.-h., Majumdar, S.N., Narayan, O. and Witten, T.A. (1996) Model for force fluctuations in bead packs. *Phys. Rev. E*, **53**, 4673-4685.

[20] Christensen, R.M. (1979) *Mechanics of Composite Materials*. Wiley, New York.

[21] Dal Corso, F., Bigoni, D. and Gei, M. (2008) The stress concentration near a rigid line inclusion in a prestressed, elastic material. Part I: full-field solution and asymptotics. *J. Mech. Phys. Solids*, **56**, 815-838.

[22] Dally, J.W. and Riley W.F. (1965) *Experimental stress analysis*. McGraw-Hill.

[23] Da Silva, M. and Rajchenbach, J. (2000) Stress transmission through a model system of cohesionless elastic grains. *Nature*, **406**, 708-710.

[24] Di Pasquale, S. (1992) New trends in the analysis of masonry structures. *Meccanica*, **27**, 173-184.

[25] Drescher, A., de Josseiling de Jong, G. (1972) Photoelastic verification of a mechanical model for the flow of a granular material. *J. Mech. Phys. Solids*, **20**, 337-351.

[26] Elishakoff, I. (2005) Controversy associated with the so-called "follower force": critical overview. *Appl. Mech. Rev.*, **58**, 117-142.

[27] Everstine, G.C. and Pipkin, A.C. (1971) Stress channelling in transversely isotropic elastic composites. *J. Appl. Math. Phys.*, **22**, 825-834.

[28] Flint, J. and Hultén, J. (2002) Lining-deformation-induced modal coupling as squeal generator in a distributed parameter disk brake model. *J. Sound Vib.*, **254**, 1-21.

[29] Frocht, M.M. (1965) *Photoelasticity*. John Wiley and Sons.

[30] Gajewski, A. and Palej, R. (1974) Stability and shape optimization of an elastically clamped bar under tension (in Polish). *Rozprawy Inzynierskie - Eng. Trans.*, **22**, 265-279.

[31] Gao, H.J., Ji, B.H., Jager, I.L., Arzt, E. and Fratzl, P. (2003) Materials become insensitive to flaws at nanoscale: lessons from nature. *Proc. Natl. Acad. Sci. USA*, **100**, 5597-5600.

[32] Gei, M., Movchan, A.B. and Bigoni, D. (2009) Band-gap shift and defect-induced annihilation in prestressed elastic structures. *J. Appl. Phys*, **105**, 063507.

[33] Geng, J., Howell, D., Longhi, E., Behringer, R.P., Reydellet, G., Vanel, L., Clément, E. and Luding, S. (2001) Footprints in sand: the response of a granular material to local perturbations. *Phys. Rev. Lett.*, **87**, 035506.

[34] Geng, J., Reydellet, G., Clément, E., Behringer, R.P. (2003) GreenŠs function measurements of force transmission in 2D granular materials. *Physica D*, **182**, 274-303.

[35] Goldenberg, C. and Goldhirsh, I. (2005) Friction enhances elasticity in granular solids. *Nature*, **435**, 188-191.

[36] Heyman, J. (1966) The stone skeleton. *Int. J. Solid Struct.*, **2**, 249-279.

[37] Herrmann, G. and Jong, I.C. (1965) On the destabilizing effect of damping in nonconservative elastic system. *J. Appl. Mech.*, **32**, 592-597.

[38] Herrmann, G., Nemat-Nasser, S. and Prasad, S.N. (1966) Models demonstrating instability of nonconservative dynamical systems. Tech. Rept. No. 66-4, Northwestern University, Dept. of Civil Engineering.

[39] Herrmann, G. (1971) Dynamics and stability of mechanical systems with follower forces. Tech. Rept. NASA CR-1782.

[40] Irwin, G.R. (1958) Discussion to a paper by A. Wells and D. Post (1958, *Proc. SESA*, **16**, 69-92). *Proc. SESA*, **16**, 93-96.

[41] Johnson, K.L. (1985) *Contact Mechanics*. Cambridge University Press.

[42] Koiter, W.T. (1996) Unrealistic follower forces. *J. Sound Vib.*, **194**, 636-638.

[43] Kröger, M., Neubauer, M. and Popp, K. (2008) Experimental investigation on the avoidance of self-excited vibrations. *Phil. Trans. R. Soc. A*, **366**, 785-810.

[44] Lamb, H. (1928) *Statics.* Cambridge University Press.

[45] Lekhnitskii, S.G. (1981) *Theory of Elasticity of an Anisotropic Body.* Mir Publisher, Moscow.

[46] Lim, J. and Ravi-Chandar K. (2007) Photomechanics in dynamic fracture and friction studies. *Strain*, **43**, 151Ű165.

[47] Lim, J. and Ravi-Chandar, K. (2009) Dynamic Measurement of Two Dimensional Stress Components in Birefringent Materials. *Exp. Mech.*, **49**, 403-416.

[48] Liu, C.-h., Nagel, R., Schecter, D.A., Coppersmith, S.N., Majumdar, S., Narayan, O. and Witten, T.A. (1995) Force fluctuation in bead packs. *Science*, **269**, 513-515.

[49] Loret, B. (1992) Does deviation from deviatoric associativity lead to the onset of flutter instability? *J. Mech. Phys. Solids*, **40**, 1363-1375.

[50] Loret, B., Simões, F.M.F. and Martins, J.A.C. (2000) Flutter instability and ill-posedness in solids and fluid-saturated porous media. In: Petryk, H. (Ed.), Material Instabilities in Elastic and Plastic Solids, CISM Lecture Notes No. 414. Springer-Verlag, Wien-New York, 109-207.

[51] Love, A.E.H. (1927) *A treatise on the mathematical theory of elasicity.* Cambridge University Press.

[52] Luding, S. (2005) Information propagation. *Nature*, **435**, 159-160.

[53] Mainstone, R.J. (1970) Brunelleschi's dome of S. Maria del Fiore and some related structures. *Trans. Newcomen Soc.*, **42**, 107-126.

[54] Martins, J.A.C., Oden, J.T. and Simões, F.M.F. (1990) Recent advances in engineering science. A study of static and kinetic friction. *Int. J. Eng. Sci.*, **28**, 29-92.

[55] Martins, J.A.C., Barbarin, S., Raous, M. and Pinto da Costa, A. (1999) Dynamic stability of finite dimensional linearly elastic systems with unilateral contact and Coulomb friction. *Comput. Meth. Appl. Mech. Eng.*, **177**, 289-328.

[56] Minshall, H. (1992) Coefficient of Friction Table. In: Lide, D.R. (Ed.), CRC Handbook of Chemistry and Physics, 73rd Edition. CRC Press, Boca Raton.

[57] Muskhelishvili, N.I. (1953) *Some Basic Problems of the Mathematical Theory of Elasticity*. P. Nordhoff Ltd., Groningen.

[58] Nguyen, Q.S. (1995) *Stabilité des structures élastiques*. Springer-Verlag.

[59] Nguyen, Q.S. (2003) Instability and friction. *Comptes Rendus Mécanique*, **331**, 99-112.

[60] Nikolai, E.L. (1928) On the stability of the rectilinear form of equilibrium of a bar in compression and torsion. *Izvest. Leningr. Politekhn.*, in-ta **31**.

[61] Oden, J.T. and Martins, J.A.C. (1985) Models and computational methods for dynamic friction phenomena. *Comput. Meth. Appl. Mech. Eng.*, **52**, 527-634.

[62] Ogden, R.W. (1984) *Non-linear elastic deformations*. Chichester, Ellis Horwood.

[63] Østervig, C.B. (1987) Stress intensity factor determination from isochromatic fringe patterns–A review. *Eng. Fract. Mech.*, **26**, 937-944.

[64] Pflüger, A. (1950) *Stabilitätsprobleme der Elastostatik*. Springer, Berlin.

[65] Pflüger, A. (1955) Zur Stabilität des tangential gedruckten Stabes. *J. Appl. Math. Mech.*, **5**, 191.

[66] Piccolroaz, A., Bigoni, D. and Willis, J.R. (2006) A dynamical interpretation of flutter instability in a continuous medium. *J. Mech. Phys. Solids*, **54**, 2391-2417.

[67] Rice, J.R. (1977) The localization of plastic deformation. In: Koiter, W.T. (Ed.), Theoretical and Applied Mechanics. North-Holland, Amsterdam, 207-220.

[68] Rice, J.R. and Ruina, A.L. (1983) Stability of steady frictional slipping. *J. Appl. Mech.*, **50**, 343-349.

[69] Sammis, C.G., Rosakis, A.J. and Bhat, H.S. (2009) Effects of off-fault damage on earthquake rupture propagation: Experimental Studies. *Pure Appl. Geophys.*, **166**, 1629Ű1648.

[70] Simões, F.M.F. and Martins, J.A.C. (1998) Instability and ill-posedness in some friction problems. *Int. J. Eng. Sci.*, **36**, 1265-1293.

[71] Socolar, J.E.S. (1998) Average stresses and force fluctuations in non-cohesive granular materials. *Phys. Rev. E*, **57**, 3204-3215.

[72] Stribeck, R. (1902) Die wesentlichen Eigenschaften der Gleit- und Rollenlager. *Z. Verein Deut. Ing.*, **46**, 1342-1348.

[73] Sugiyama, Y., Katayama, K. and Kinoi, S. (1995) Flutter of a cantilevered column under rocket thrust. *J. Aerospace Eng.*, **8**, 9-15.

[74] Sugiyama, Y., Katayama, K., Kiriyama, K. and Ryu, B.-J. (2000) Experimental verification of dynamic stability of vertical cantilevered columns subjected to a sub-tangential force. *J. Sound Vib.*, **236**, 193-207.

[75] Temme, N.M. (1996) *Special functions.* John Wiley and Sons, New York.

[76] Threlfall, D.C. (1977) The inclusion of Coulomb friction in mechanisms programs with particular reference to DRAM. *Mech. Mach. Th.*, **13**, 475-483.

[77] Timoshenko, S.P. and Gere, J.M. (1961) *Theory of elastic stability.* McGraw-Hill, New York.

[78] van der Giessen and E., Needleman, A. (1995) Discrete dislocation plasticity: a simple planar model. *Model. Simulat. Mater. Sci. Eng.*, **3**, 689-735.

[79] Wang, C.C. (1970) A new representation theorem for isotropic functions, Parts I and II. *Arch. Rat. Mech. Anal.*, **36**, 166-223.

[80] Wang, Z.Y., Zhang, H.T. and Chou, Y.T. (1985) Characteristics of the elastic field of a rigid line inhomogenity. *J. Appl. Mech.*, **52**, 818-822.

[81] Wu, K.C. (1990) Line inclusion at anisotropic bimaterial interface. *Mech. Mater.*, **10**, 173-182.

[82] Zhu, Y., Shukla, A. and Sadd, M.H. (1996) The effect of microstructural fabric on dynamic load transfer in two dimensional assemblies of elliptical particles. *J. Mech. Phys. Solids*, **44**, 1283-1303.

[83] Zyczkowski, M. (1991) *Strength of structural elements.* Elsevier.

[84] Ziegler, H. (1953) Linear elastic stability. A critical analysis of methods. *J. Appl. Math. Phys.*, **4**, 89-121.

[85] Ziegler, H. (1956) On the concept of elastic stability. *Adv. Appl. Mech.* , **4**, 351-403.

[86] Ziegler, H. (1977) *Principles of structural stability.* Birkäuser Verlag.